

## General introduction

We thank the reviewers for their constructive comments.

As both reviewers raised partly the same issues, we will answer the comments below together.

Major changes to the manuscript are

- a) the restructuring with respect to the long methods section, of which there is now only a summary left in the main manuscript, whereas the major part was moved into the electronic supplement;
- b) a necessary modification of the small-iron-particle discussion, which originated from additional later analyses. The latter revealed a previously unknown artifact of the sample substrates. Details are given in the according sections;
- c) introduction of a section dealing with feldspar particles in manuscript and supplement.

Our answers are written in red color, and changes to the manuscript are also shown in red.

Below the answers, please find the modified manuscript with figures, and below that we have attached the modified electronic supplement, as this was also discussed by the reviewers.

## Reviewer 1

### General comments

The authors have provided a very nice manuscript of measurements and associated modelling of aerosols in the Caribbean boundary layer which is suitable for publishing in ACP. The composition and mixing state of dust, sea salt and sulphate are analysed and they have been detailed in their efforts and provide a good analysis of uncertainty in the results. The general flow of the paper could be improved by condensing the methods and some small additions to the discussions. Of note I feel is the dry deposition discussion – a parameter which hinders aerosol modelling in general and, as shown here, needs further work in constraining.

### Specific comments

Methods:

The methods section is highly detailed, particularly in its use of equations. While it is commendable to be thorough in an analysis I feel the manuscript would greatly benefit from condensing the main methods to the core equations and text. Following each one through in detail to its final derivation is not necessary for the discussion and instead detracts the reader from getting to said results. The SI is the ideal place for much of this text, and some could even be removed totally.

The deposition model section has been condensed to a summary of the most important points and literature references. The original section has been moved to the electronic supplement.

For example, Section 2.3.5: It is good to be thorough and test other statistics, but this is not necessary in the main text and somewhat disturbs the flow. It is sufficient to briefly state you performed the bootstrap analysis with 10,000 replications and move on.

The statistics section also has been condensed to a summary and the original section has been moved to the electronic supplement.

Section 2.4.1: The Petters manuscript and hygroscopicity term is well known within the atmospheric community. Small statements about assumed values and uncertainties would be sufficient I feel.

Also changed as requested.

## Results:

Section 3.2.1: In Figure 5, model d (Aluko) looks like it would perhaps give closer agreement to results in Table 2 than it does. By comparing results of model e (Piskunov) and d (and others if appropriate, e.g. from the tuning exercise) could the Authors also comment on impacts that uncertainty in differences in the deposition velocity for fine (<2.5 µm) or coarse (>2.5 µm) mode aerosol has on the results? - which are significant for fine mode between models d and e, but more similar in coarse mode.

As the fine mode aerosol only contributes about 2% to the total mass deposition (Fig. 14 of the original manuscript), the uncertainty here would not affect considerably the mass flux. Instead, the mass flux uncertainty is mainly depending on the coarse mode. The situation is slightly different for the mass concentration (Fig. 11 of the original manuscript), as the fine mode of course contributes more here. Nevertheless, also the mass concentration is dominated by larger particles, so the effect is small.

However, due to the model uncertainty, it can't currently be recommended to use deposition measurements for conclusions on atmospheric fine mode or total number concentrations.

Section 3.3.2: This is a great section but would benefit from a bit more explanation I feel. How do the air mass proveniences link to the trajectories? Fig 15 looks similar to the trajectories, but Fig 16 (particularly the iron) has a very difference providence – how was this reached? This is important as the air mass trajectories suggest there is a difference in 2016 in that it has a much stronger European component to it than 2013. Which makes sense with the SO<sub>4</sub> sources analysis.

Air mass providence is calculated from the trajectories as outlines in section 2.2, i.e. it reflects frequency of trajectories from a certain area. Also Fig. 16 in the old manuscript was based on the same trajectories. By weighting with different values from the, analysis, other regions can get into focus. That can change the pattern, in particular for rare occurrences. However, ...

However, the southern African source the Authors state for the combustion iron is less obvious I feel from the trajectories themselves, although apparent in Fig 16. Furthermore, the total iron to dust correlation is unfortunately not shown but, as the authors point out, combustion iron has become a topic of much discussion recently and so it would therefore be good to see this result and then put in the context of whether a combustion iron source is visible in 2016 vs 2013. For a south American source can the Authors identify if this likely to be anthropogenic or biomass burning dominated?

... the situation for the iron displayed in Fig. 16 lower part in the old manuscript was different.

As the iron was important to both reviewers, but the pattern was not so easy to explain, we performed additional analyses on the according particles. Also, we tried to make sure that the values were real by using additional blank samples.

At this point it turned out that some of the charges of carbon adhesive suffered from an iron contamination, which we had not observed on these substrates before. The manufacturer and type did not change and not all charges were affected, so it must have been a new source of contamination during the manufacturing or packaging process.

The contamination is on a very low level. If there is a dust event, it becomes completely negligible in comparison to the dust particles (< 1 % of the iron in dust). However, during a few days in 2016 we had very clean conditions with respect to dust, i.e. when the airmasses arrived from Southern America. In these cases, the contamination became visible. As a result, the lower panel of Fig. 16 in the old manuscript showed effectively the source of clean airmasses arriving in Barbados, but not of anthropogenic iron.

Therefore, we have removed the according section from the manuscript and added a comment on artifact removal in the methods section. Also, we have modified the affected plots.

Section 3.3.4: Small additional discussions about 1) Iron solubility: interstitial and cloud-borne changes with sulphate in particular.

We have added a comment on that in the conclusions section

2)Relative concentration of feldspar in the ice nucleation discussion.

We have introduced a 'feldspar index' to determine feldspar content in the methods section and give a plot now of relative feldspar contribution to the silicate fraction, which appears to be relatively constant over time at Barbados.

3)Wet deposition as a loss process when activated to be CDNC. Would be interesting.

We have added a comment on that in the conclusions section, but further work including cloud modeling would be needed to assess these processes.

### Technical corrections

#### Figures

Please add legends to all figures where missing and check the use of colours is appropriate (see below for some examples).

Fig 2: The use of a log scale and a continuous colour bar is not intuitive. Please change to a discrete colour bar (10 or 5 colours).

Changed as requested.

Fig 4: colours do not match numbers using this scale, e.g. green is 2.5-4.5, but blue is 1.2-1.8?

The colors carry additional information, as described in the caption, and do not apply to the x or y scale.

Fig 12: The empty box plot for high volume sampler concentration looks odd. I suggest replacing with a simple horizontal line or a shape (e.g. a star).

We have tried both alternatives, but the plot becomes more difficult to read, as the symbols and lines blend with the existing symbols. Therefore, we would like to keep the plot as it is.

Fig 13: the x-axis is logscale, but the bars are a fixed width. This does not make sense. Either alter to scalar plot (preferred) or alter the width of the bars to match the scale.

The bars perfectly match the scale. They appear as same width because the intervals were chosen equidistantly.

Figs 15, 16: Again, the use of continuous colours would probably be better as discreet.

Changed as requested. Fig. 16 had to be partially removed (see general iron discussion).

Fig 16: 2013 small Fe-rich particles looks like it missing the data?

Values were just extremely low, but Fig. 16 had to be partially removed (see general iron discussion).

Fig S4, S5. Increase legend size to a single bar and add numbers to it.

Changed as requested.

Fig S9 : see Fig 12 note above

See comment above.

Supplementary tables and figures can be grouped together (currently tables are interspersed throughout figures)

Changed as requested.

## Text

Italics are suggested additions to text.

L35: Largest by mass only, not number.

Corrected.

L36-37: Expand this by a sentence, too brief.

Done as requested.

L40: Define the Central American Dust Barrier causes.

Mainly removal, but also meridional transport processes. Added as explanation to the manuscript.

L42: What processes are not fully understood? Use of 'these' is too vague here.

Actually down-mixing as well as deposition processes, but only the latter are topic of this manuscript. Clarified.

L44: Change to: '. . .by physical and chemical processing, . . .'

Changed as requested.

L46-47: This is quite obvious. Best to either expand or remove sentence.

Sentence removed.

L47-48: Link with expanded L36-37 as to why this happens.

We have added explanations and examples.

L49: While could start a new paragraph.

Changed as requested.

L49-51: Brief summary of these studies/anything of importance to note?

These studies describe aerosol mixing at different places around the world for certain situations. We have added two sentences to describe the advances of the present manuscript.

L55 and on: change methodical to methods

Changed to methodological by request of the other reviewer.

L62: 'Offline' can mean many things. Define it here to avoid ambiguity.

Parenthesis inserted, defining as 'analysis of aerosol particles collected on a substrate'

L111: remove space before comma

Corrected.

L198: '. . .mentioned correction methods as a function . . .'

Changed as requested.

L199: 'a higher accuracy in . . . can be achieved'

'in quantification' added

L246: '. . .not the focus ..'

Corrected.

L255: '. . .separately an important. . .'

Corrected.

L260: without seeing the dust:iron ratio it is not possible to say that Fe is safely assumed to be from dust and not combustion.

The term 'dust' in this context of calculating single particle composition serves to differentiate between sea-salt, sulfate compounds and 'dust' inside a single particle. It therefore means an inorganic, thermally stable, non-carbonaceous compound. We do not claim that it is 'natural mineral dust'. In this context, in fact we would also refer to stable anthropogenic iron compounds as 'dust'. We have inserted a parenthesis with the above-mentioned definition.

As additional information: when we look at the single particle scale (after removal of the contamination artifacts), 95 % of the particles have a Fe:Si ratio < 0.33. Only 1.8 % have a Fe:Si ratio > 1, and of these most contain also Si. Therefore we would not assume them to be of anthropogenic origin.

L540: 'conclude'

Corrected.

L722-723. Deposition velocities are described in section 2.4.2.

Links corrected.

L792-793: 2016 listed twice. However, I can see no obvious difference in the air masses coming from South America in Fig.S6 anyhow?

Sentence removed, as indeed not significant.

L801-803: Nitrate as well as sulphate associated with dust sources is likely to be from Europe (e.g., anthropogenic in origin).

Changed as requested

## Reviewer 2

### General comments:

This manuscript presents new methods for accurately determining composition and mixing states of individual coarse aerosol particles by an automated SEM-EDX, and their application on the aged Saharan dust samples collected in the Caribbean boundary layer. Traditionally, individual particle analysis suffered from uncertainties related to poor counting statistics. There has been a significant gap between the ambient mass size distribution and such qualitative information based on individual particle analysis.

The authors however, succeeded to analyze large number of particles by the use of a novel automated SEM-EDX, and to provide a much more comprehensive and quantitative view on the mixing states of dust as a function of particle size. Sampling and data analysis were done very carefully by taking into account many potential sources of errors and uncertainties (e.g. quantification of elements, estimation of dust mass, sampling artifacts, counting statistics) and they are well defined and characterized in the manuscript. I therefore believe the manuscript deserves certain credit and can be a good contribution to ACP. However, such thorough and detailed verification of the methods in turn made the manuscript rather lengthy (especially the method section) and not easy for the readers to digest its major findings. It requires an extensive restructuring, and there are also some concerns on the assumptions made and interpretation of the results. The paper may be recommended for publication after these concerns are properly addressed.

We have moved considerable parts into the electronic supplement and provide a summary in the main manuscript.

Specific comments:

Lines 17-19: Please rephrase “Techniques were developed to conclude from collected aerosol on atmospheric concentrations and aerosol mixing state, and different models were compared.”

Rephrased to “Techniques are presented and evaluated, which allow for statements on atmospheric aerosol concentrations and aerosol mixing-state based on collected samples.”

Line 51: “Data basis is still limited” can be elaborated to make this study stand out more from previous studies.

We have added two sentences on the major differences (methodological advancements, much higher particles numbers (statistical significance) and longer observed time periods).

Line 56: methodological?

Changes as requested (in multiple places)

Lines 68-623: While introduction section is made up of only 3 paragraphs, method section accounts for the majority of the manuscript and the overall structure appears rather unbalanced. Many details, equations and figures in the method section can be moved to supplementary information (SI). The explanation in the text can be significantly shortened by simply referring to corresponding sections in the SI.

We have moved considerable parts into the electronic supplement and provide a summary in the main manuscript.

Line 69: Sampling time and duration for three different samplers are not well explained. How do they coincide? I imagine deposition sampler requires longer time.

We have added remarks on sampling duration to each sub-section, and in addition we provide a table of all sampling times and durations in the electronic supplement (S 1). The sampling time for the DPDS is around 1 day, whereas the active techniques are in the range of 1 hour. In case of more rapidly changing aerosol conditions, this may hamper strict comparability. We have added a remark on this topic.

Also, we have added a comment in section 3.2.1. However, as the same qualitative differences between the techniques – similar in quantitative disagreement – are observed for all samples, it appears to us as a minor source of error.

Line 147: As a result,

Changed as requested

Lines 175-178: Validity of estimating volume equivalent diameter (in section 2.3) based only on 2-dimensional projected area and perimeter is questionable. It may work rather well for dry and solid particles such as pure silicates, but if particles were internally mixed with soluble materials and sampled at high relative humidity conditions (which might often be the case at Ragged Point), flattening of deliquesced particles on the substrate may become a source of significant sizing bias. Some people employ tilting of sample stages or apply shadowing to measure the height of the particles under SEM analysis.

It is correct that sea-salt particles collected at Ragged Point are nearly always in deliquesced state. However, we have observed frequently crystallized particles instead of the flattened ones mentioned by the reviewer. The flattened ones we did observe for example in the Mediterranean for smaller particles. This might be linked to the size range (large droplets) and to the substrate (hydrophobic), which might favor a compact recrystallization, but also possibly to the composition (potentially low in organics).

In addition, we have checked the average backscatter electron image brightness for different particle classes. We find here that the sea-salt particles show a higher average brightness than the silicate

ones, as predicted by their higher average atomic number (e.g., Goldstein 2003, "Scanning Electron Microscopy and X-ray analysis", chapter 4.4.2). If the particles would be flat, it would be expected that the BSE brightness would be very low, as then the low-Z background would average with a thin film of NaCl to a low brightness.

We have added a note to the according section.

Line 185: achieved instead of reached?

Changed as requested

Lines 196-197: How exactly does a smaller accelerating voltage (12.5 kV) ease the particle morphology problem? Please explain.

Fig. 1 was extended to show the increased deviations at higher acceleration voltages.

Lines 212-213: "...which not only includes particle but also the substrate."

Sentence was modified

Lines 213-214: Please rephrase "they do only indirectly represent an amount of matter with respect to the particle."

Sentence was modified

Lines 217-218: "...while the remaining uncertainty originates mainly from the particle to particle variation."

Changed as requested

Lines 222-223: why is the case for 20 kV is shown instead of 12.5 kV?

Two reasons: many other studies use 20 kV as standard, and because problems are more pronounced and better visible at 20 kV than at 12.5 kV (shown above). Fig 1 and according caption and text were modified to demonstrate the dependence on acceleration voltage.

Line 255: "...separately is an important task."

Changed as requested

Line 328: here may suffer?

Changed as requested

Lines 349-350: "chemically aggressive environments" is too vague. Please elaborate.

We have added an example for acidic low pH, but think that the details are well-described in the referenced works and not topic of the present manuscript.

Representing bio-available iron by spherical surface area and metal oxide mass fraction alone may be misleading and needs further explanation about its limitations, since Fe dissolution is also highly dependent e.g. on pH and presence of inorganic and organic ligands (which cannot be addressed by the current analytical approach).

We have added a note to emphasize this point.

Line 659: As a result,

Changed as requested

Line 757: e.g.

Changed as requested

Line 778: "...while a strict disambiguation can't be done for elements also found in sea salt."

Changed as requested

Line 779: “most likely derived only from dust”

Changed as requested

Line 790: Western Africa

Changed as requested

Line 894: considerably higher

Changed as requested

Line 896-908: With regard to the change in dust behavior due to internal mixing, I generally have no objection about the main conclusion that the mixing of dust with sea-salt and sulfate would significantly affect its deposition velocity as stated in the preceding paragraph. I also admit that the conclusion is well supported by the solid results shown in this study. **In contrast, the whole idea** about enhanced ice-nucleation efficiency of dust through internal mixing needs more careful discussion and is not supported by sufficient results. For example, some studies report deactivation of ice nuclei due to atmospherically relevant coating (e.g. Cziczo et al., Environmental Research Letters, 2009), and this deactivation by coating may be more pronounced especially for deposition mode ice nucleation. This impact of coating on different freezing modes might need to be explained clearly in the text not to confuse the readers. Also, the heterogeneous ice freezing temperatures of dust can decrease with increasing concentration of different solutes (e.g. Zobrist et al., J. Phys. Chem. A, 2008) in immersion freezing. There may be a regime where cloud droplets are not dilute enough such that freezing temperatures of droplets activated upon sea-salt / dust mixture can be significantly decreased (Iwata and Matsuki, ACP, 2018). There could be several competing effects of coating on dust ice nucleation efficiency and this may not act identically for different freezing modes. Besides, as authors pointed out themselves (in line 890), mixed particles with a smaller contribution of hygroscopic material, which remain undetected by the current analytical approach, may be present. Droplet growth and activation kinetics may behave differently at sub- and super-saturated conditions and such seemingly uncoated dust may as well be activated as cloud droplets under higher supersaturation. This subject may need a whole new paper to be discussed. Since there are not much results to support the proposed hypothesis, this whole section about the proposed enhancement of dust ice nucleation efficiency may even be omitted from the current manuscript.

We agree with the reviewer that the topic of mixed particle ice activation will need considerable additional investigations, as we wrote in the conclusions. With the hypothesis, our goal was to point out another process which might be of atmospheric relevance, and not to describe the process in detail (which would be far beyond the scope of the current paper).

However, as we can't provide evidence for a particular process, we have removed the according paragraph from the result section. Instead, we have added a short comment on potential implications at the end, calling for further investigations.

Fig. 18: In this context, isn't the annotation for the third figure from the top supposed to be “sea-salt/silicate mixtures” and “sulfate / dust mixtures”?

Corrected, this was a mistake.

Line 1468: “size class is shown in conjunction with. . .”

Changed as requested

# Composition and mixing state of atmospheric aerosols determined by electron microscopy: method development and application to aged Saharan dust deposition in the Caribbean boundary layer

Konrad Kandler<sup>1\*</sup>, Kilian Schneiders<sup>1</sup>, Martin Ebert<sup>1</sup>, Markus Hartmann<sup>1,†</sup>, Stephan Weinbruch<sup>1</sup>, Maria Prass<sup>2</sup>, Christopher Pöhlker<sup>2</sup>

<sup>1</sup>Institute for Applied Geosciences, Technical University Darmstadt, 64287 Darmstadt, Germany

<sup>2</sup>Max Planck Institute for Chemistry, Multiphase Chemistry Department, 55128 Mainz, Germany

<sup>†</sup>now at: Experimental Aerosol and Cloud Microphysics Department, Tropos Leibniz-Institute für Tropospheric Research (TROPOS), 04318 Leipzig, Germany

\*Correspondence to: K. Kandler ([kandler@geo.tu-darmstadt.de](mailto:kandler@geo.tu-darmstadt.de))

**Abstract.** The microphysical properties, composition and mixing state of mineral dust, sea-salt and secondary compounds were measured by active and passive aerosol sampling followed by electron microscopy and X-ray fluorescence in the Caribbean marine boundary layer. Measurements were carried out at Ragged Point, Barbados during June/July 2013 and August 2016. **Techniques are presented and evaluated, which allow for statements on atmospheric aerosol concentrations and aerosol mixing-state based on collected samples.** It became obvious that in the diameter range with the highest dust deposition the **deposition velocity** models disagree by more than two orders of magnitude. Aerosol at Ragged Point was dominated by dust, sea-salt and soluble sulfates in varying proportions. Contribution of sea-salt was dependent on local wind speed. Sulfate concentrations were linked to long-range transport from Africa / Europe and South America / Southern Atlantic Ocean. Dust sources were **located** in Western Africa. **The dust silicate composition was not significantly varying. 3 % of the silicate particles were pure feldspar grains, of which about a third were K-feldspar.** The total dust deposition observed was  $10 \text{ mg m}^{-2} \text{ d}^{-1}$  (range  $0.5\text{--}47 \text{ mg m}^{-2} \text{ d}^{-1}$ ), of which  $0.67 \text{ mg m}^{-2} \text{ d}^{-1}$  was iron and  $0.001 \text{ mg m}^{-2} \text{ d}^{-1}$  phosphorus. **Iron deposition was mainly driven by** silicate particles from Africa. Dust particles were mixed internally to a minor fraction (10 %), mostly with sea-salt and less frequently with sulfate. It was estimated that average dust deposition velocity under ambient conditions is increased by the internal mixture by 30–140 % for particles between 1 and  $10 \mu\text{m}$  dust aerodynamic diameter, with approximately 35 % at the mass median diameter of deposition ( $7.0 \mu\text{m}$ ). For this size, an effective deposition velocity of  $6.4 \text{ mm/s}$  (geometric standard deviation of 3.1 over all individual particles) was observed.

## 1 Introduction

Mineral dust and sea-salt are globally the most abundant aerosol types **by mass** in the atmosphere (Andreae 1995; Grini et al. 2005). They are considerably affecting the earth's radiation budget (Liao et al. 1998; Choobari et al. 2014) **by scattering and absorbing solar and terrestrial radiation. Moreover, they modify** cloud processes **by supplying condensation nuclei and changing the atmospheric stability conditions** (Koehler et al. 2009; Tang et al. 2016; Karydis et al. 2017). Over the North Atlantic Ocean, large amounts of dust are transported westwards in the Saharan Air Layer, until they reach the Caribbean (Karyampudi et al. 1999; Prospero et al. 2014). Here, dust usually does not cross the **'Central American Dust Barrier' to the west. Instead, is mainly removed from the atmosphere, but to a lesser extent also transported in meridional directions** (Nowottnick et al. 2011).

With respect to the removal, dust becomes mixed down into the marine boundary layer by turbulent and convective processes. Here, it is then subject to wet and dry deposition processes, which remove it from the atmosphere. These deposition processes, however, are not yet fully understood (Prospero et al. 2009; Nowottnick et al. 2011).

During its transport, mineral dust may undergo modifications by physical and chemical processing, cloud processing or microphysical effects (Andreae et al. 1986; Falkovich et al. 2001; Matsuki et al. 2005; Sullivan et al. 2007a; Sullivan et al. 2007b). These processes will change the composition and particle size of dust, and thus modify its radiative properties and cloud impacts. For example, an addition of a soluble compound to an insoluble dust particle may obviously on one hand alter its cloud droplet activation properties (Wurzler et al. 2000; Garimella et al. 2014). On the other hand, it might de-activate the original dust particle for deposition ice nucleation (Cziczo et al. 2009). In addition, the coating may on one side enhance the scattering of the particle in dry state by adding non-absorbing material and increasing its size (Bauer et al. 2007; Li et al. 2009), but on the other side in deliquesced state the water shell may increase absorption (Bond et al. 2006), enhancing the absorption of according dust components (Lack et al. 2009).

To assess the mixing state of mineral dust, techniques considering single particles are required. While there have been investigations in the past (Zhang et al. 1999; Zhang et al. 2004; Dall'Osto et al. 2010; Deboudt et al. 2010; Kandler et al. 2011a; Fitzgerald et al. 2015), the data basis is still limited. In particular previous studies based on electron microscopy did not take into account methodological problems. Also, they observed smaller particle numbers, affecting statistical significance, and used shorter observation periods. Studies based on single-particle mass spectrometry, in contrast, were not able to quantify elemental contributions to single particles and therefore could not conclude on material fluxes. In the present work, we present results from two field campaigns in summers 2013 and 2016, where the aerosol in the marine boundary layer at Ragged Point in Barbados was collected by active and passive sampling techniques.

A particular challenge for these campaigns was the high wind speed and the high humidity at the sampling site. Therefore, the present publication consists of an extended methodological section in the electronic supplement with three major topics and a methodological as well as atmosphere-related results section. One methodological section deals with the determination of composition and mixing state of individual particles, taking into account quantification artifacts and modeling the dust- and non-dust components as well as their hygroscopic behavior. A second section is on particle collection representativeness and models relating atmospheric concentration and deposition, taking into account the single particle properties at ambient conditions. Finally, when aerosol mixing state is assessed based on offline aerosol analysis (i.e. analysis of aerosol particles collected on a substrate), considerations on coincidental mixing have to be made to ensure the representativeness of the results for the atmosphere. Therefore, in a third section these fundamental considerations based on model as well as experimental data are presented. In the result section, we report first on these theoretical and experimental methodological aspects, before we then discuss the atmospheric implications of the measurements.

## 2 Methods

### 2.1 Particle sampling and location

Aerosol was sampled at Ragged Point, Barbados (13° 9' 54" N, 59° 25' 56" W) from June 14 until July 15, 2013, and from August 6 until August 28, 2016. Sampling was performed on top of the measurement tower, approximately 17 m above the bluff (Zamora et al. 2011), which descends 30 m to the sea surface. Particles were collected on pure carbon adhesive (Spectro Tabs, Plano GmbH, Wetzlar, Germany) mounted on standard SEM aluminum stubs (Free-wing impactor, Dry particulate deposition sampler) or pure nickel plates (cascade impactor). **Due to the requirements of single particle analysis – i.e. particles separated on the substrate and sufficient particle numbers – different sampling times had to be chosen for the separate instruments due to their varying effective deposition velocities (see Table S 1 in electronic supplement).**

#### 2.1.1 Free-wing impactor (FWI)

A FWI was constructed for inlet-free collection of particles larger than 5  $\mu\text{m}$  in diameter. A FWI consists in general of a rotating arm with a sampling substrate attached, which acts as body impactor (see Fig. S 3 in electronic supplement). Rotation speed, wind speed and sample substrate geometry determine the particle size cut-off for collection. FWI applied in previous investigations were constructed with a rigid setup, so adaptation to actual meteorological conditions (i.e. perpendicular adjustment of the impaction vector) needed to be performed by hand or was neglected (Jaenicke et al. 1967; Noll 1970; Noll et al. 1985; Kandler et al. 2009). The present setup achieves perpendicularity by self-adjustment of the flexibly mounted sampling substrate to the sum vector of wind and rotary movement. This is performed by addition of a small wind vane at the rotating arm adjusting the angle of the substrate. The rotating arm is driven by a stepper motor, which is mounted on a larger wind vane, aligning the construction with the horizontal wind vector. To ensure that the wind vanes respond only to the dynamic pressure, any imbalance in the setup must be avoided. The arm length of the FWI is 0.25 m. With a constant rotation frequency of 10 Hz and the wind speeds at the sampling location, particle impaction speeds between 16.4 and 20.2 m/s were achieved. **In conjunction with collection times between 23 and 112 minutes, this** corresponded to sampling volumes of air between 2.7 and 14.7  $\text{m}^3$ . While in principle the FWI could disturb its own flow field in low wind situations – the sample collector may be influenced by its own wake from the previous rotation – this was not an issue for the present work, as the distance of the sampling volume shifted by the wind between the same angular positions of two consecutive rotations was always larger than 0.45 m. This is a large and therefore safe distance in comparison to the small diameter of the sampling substrate and the counterweight (12.5 mm and 25 mm, respectively). In total, 30 samples were collected during the campaign in 2013.

#### 2.1.2 Dry particulate deposition sampler (DPDS)

The DPDS used in the present work is derived from the flat plate sampler of Ott et al. (2008b), which performed best with respect to wind speed dependence in their tests. It consists of two round brass plates (top plate diameter 203 mm, bottom plate 127 mm, thickness 1 mm each) mounted in a distance of 16 mm. In contrast to the referred design, the one used here has a cylindrical dip in the lower plate, which removes the sampling substrate – a SEM stub with a height of 3.2 mm – from the airflow, reducing the flow disturbance. The dip is larger than the SEM stub and has small holes in the bottom to catch and dispose droplets creeping across the lower plate due to the wind dynamical pressure. The top surface of the SEM stub is located 5 mm below the lower plate's top surface. Larger droplets (> 1 mm) are prevented by this setup from reaching the SEM stub surface at the local

wind speeds (Ott et al. 2008b). A total of 29 samples were collected in 2013 and 22 in 2016 with an exposure time of mostly 1 day.

### 2.1.3 Cascade impactor (CI)

While the principle design of the used CI is described by Kandler et al. (2007), a new version with a larger housing, but with the same collection characteristics, was deployed in the present work. An omnidirectional inlet with a central flow deflector cone was used, whose transmission is discussed in section 2.4.3. The impactor was operated at a flow rate of 0.48 l/min, which is set by a critical nozzle. Nozzle diameters of 2.04, 1.31, 0.71, 0.49, 0.38, and 0.25 mm were used, corresponding to nominal cut-off aerodynamic diameters of 5.2, 2.7, 1.0, 0.54, 0.33, and 0.1  $\mu\text{m}$ , respectively. Sampling times were adjusted to the estimated aerosol concentration and ranged between 10 and 60 min for the supermicron and between 12 and 45 s for the submicron fraction. A total of 30 CI samples were collected in 2013.

## 2.2 Meteorological data, backward trajectory analyses and high-volume sampling / mass concentrations

In 2013, meteorological data was obtained at Ragged Point directly next to the particle sampling devices. In 2016 wind, temperature and relative humidity were measured in parallel at The Barbados Cloud Observatory at Deebles Point, which is located 400 m across a small cove to the southeast (Stevens et al. 2016).

The measurements in 2013 are grouped into two time periods divided by the passage of the tropical storm Chantal, which changed the atmospheric structure and air mass origin (Weinzierl et al. 2017). The period from June 14 to July 8 will be referred to as pre-storm, the one from July 10 to 15 as post-storm.

Backward trajectories were calculated with Hysplit 4 rev. 761 (Stein et al. 2015) based on Global Data Assimilation System (GDAS) with 0.5  $^{\circ}$  grid resolution (NOAA-ARL 2017). A backward-trajectory ensemble consisting of a grid of 3x3 trajectories ending at 13.16483 ( $\pm 0.5$ )  $^{\circ}$  N and 59.43203 ( $\pm 0.5$ )  $^{\circ}$  W at each altitude above sea level (300, 500, 700, 1000, 1500, and 2500 m) was calculated. Backward trajectory length was 10 days in 1-hour steps, and an ensemble calculation was started for every hour during the sample collection periods. Taking into account particle concentrations and deposition rates as well as chemical properties, potential source contribution functions (PSCF) were calculated (Ashbaugh et al. 1985) with a boundary layer approach. For each trajectory point it was checked, whether the trajectory altitude was below the lowest boundary layer height provided by the GDAS data set. If this condition was met, this particular point was regarded as a potential aerosol injection spot and counted into the according source grid cell of 1 $^{\circ}$  x 1 $^{\circ}$  size. For determining possible sources, all trajectories originating during collection of a particular sample were attributed with sample properties of interest. Finally, the average for each source grid cell was calculated and then weighted with a function based on the number of points in the cell to avoid an overrepresentation of cells with high statistical uncertainty. The weighting function is generalized from the step function of Xu et al. (2010) as

$$wt_{PSCF} = \exp \left[ -2.93 \left( \frac{W_j}{\bar{W}} + 0.89 \right)^{-2.94} \right] \quad (1)$$

with  $W_j$  the number of trajectory points counted in cell number  $j$ ,  
 $\bar{W}$  the average number of trajectory points per cell.

As a result, a map based on PSCF shows regions with typically high or low values for air masses passing through the boundary layer in according grid cells. Note that by this approach, sources contributing to advected aerosol can be identified, but local sources of course will not provide a usable signal. Also, aerosol from remote sources might be transported inside the boundary layer and, thus, would be attributed to also to the transport path in addition to its source.

### 2.3 Scanning electron microscopy: individual particle composition, analytical and statistical uncertainties

About 22,000 individual particles (FWI), 65,700 (DPDS) and 26,500 (CI) were analyzed with a scanning electron microscope (SEM; FEI ESEM Quanta 200 FEG and 400 FEG, FEI, Eindhoven, The Netherlands) combined with an energy-dispersive X-ray analysis (EDX; EDAX Phoenix, EDAX, Tilburg, The Netherlands and Oxford X-Max 120, Oxford Instruments, Abingdon, United Kingdom). The samples were analyzed under vacuum conditions (approximately  $10^{-2}$  Pa) without any pretreatment. Before automated analysis, samples were screened for surface defects, distinctive unusual particles shapes or deposition patterns indicating possible artifacts or contamination, and traces of liquids. Areas with surface defects (holes and bubbles in the substrate) were excluded from further data processing.

From blank sample analysis, certain particle populations were identified as contaminants and therefore removed from the analysis. In these particles, there was detected only Fe, Cr+Fe (stainless steel), F+Si, Cl+Fe, or Al+Cl+Fe. In comparison to the abundance of the atmospheric particles on the substrate, the contaminants were mostly rare ( $\ll 1\%$ ). Sample analysis was performed automatically by the software-controlled electron microscope (software EDAX/AMETEK GENESIS 5.231 and Oxford Aztec 3.3). Automated particle segmentation from the background was performed based on the backscatter electron signal. An acceleration voltage of 12.5 kV, a 'spot size 5' (beam diameter about 3 nm) and a working distance of approximately 10 mm were used. Scanning resolution was adjusted to the particles size. For the FWI and DPDS samples 140 to 300 nm/pixel were used, for the CI samples 180 or 360 nm/pixel for the stage containing the largest particles (mainly particles larger than 2.5  $\mu\text{m}$  diameter) and 73 nm/pixel for the stages containing smaller particles. An X-ray signal collection time between 15 s and 20 s (EDAX) and 2 s (Oxford) for each particle was used (yielding 40,000–100,000 total counts), during which the beam was scanned over the particle cross section area.

The image analysis integrated into the SEM-EDX software determines the particles size as projected area diameter:

$$d_g = \sqrt{4B/\pi} \quad (2)$$

with  $B$  the area covered by the particle on the sample substrate.

Following Ott et al. (2008a), the volume-equivalent diameter is estimated from the projected area diameter via the volumetric shape factor expressed by particle projected area and perimeter as

$$d_v = \frac{4\pi B}{P^2} d_g = \frac{1}{P^2} \sqrt{64\pi B^3} \quad (3)$$

with  $P$  the perimeter of the particle.

Note that estimating the volume-equivalent diameter by this technique can be source of a bias, if the particles are largely non-isometric, e.g., droplets based on soluble material drying into a flat film. As it was observed here that sea-salt and sulfate mostly form crystals and clumps, this effect is regarded of minor importance for this work.

In addition, for the assessment of particle coverage homogeneity and size distribution determination series of 1,000 to 2,700 images were acquired for each sample. They were analyzed by the Software Fiji/ImageJ 1.51d (Rasband 2015), using also Eq. (2) for particle size determination after application of a “triangle” type auto threshold for particles segmentation (refer to Fiji/ImageJ documentation for further details).

### 2.3.1 Quantification of elemental composition

Fully quantitative results in EDX analysis can only be **achieved** under specific sample conditions. When the composition of an analyzed spot is derived from an X-ray spectrum, the sample geometry has to be considered. Besides assuming perfect smoothness and homogeneity, commonly either infinite sample depth (i.e. significantly larger than the interaction volume of a few  $\mu\text{m}$ ) or presence of an infinitely thin film is assumed. In the former case, a ‘ZAF’ correction can be applied (Trincavelli et al. 2014), in the latter for example the Cliff-Lorimer method (Cliff et al. 1975). However, for particles these assumptions and the resulting quantifications are not valid, as shown by Laskin et al. (2006) in their Fig. 3. To overcome this problem, several standard-less techniques can be applied (Trincavelli et al. 2014), for example a Monte Carlo simulation of the interaction volume can be used (Ro et al. 2003). Alternatively, particle ZAF algorithms can be applied at least for larger particles with diameters above 1  $\mu\text{m}$  (Armstrong 1991; Weinbruch et al. 1997). In the present work, however, an approach with less computational cost is applied. First, on the measurement side, a lower acceleration voltage – 12.5 kV instead of 20 kV in comparative studies – eases the particle morphology problem. **The left two graphs of Fig. 1 show for an albite standard the Na/Si and Al/Si ratios, demonstrating the impact of different acceleration voltages on the quantification. Also, it is obvious that the problem is more pronounced for a higher difference in the energies of the characteristic peaks used for quantification.** Second, on the data analysis side by combining the mentioned correction methods as function of particle size, a higher accuracy **in quantification** can be achieved. In principle, particle smaller than a limit size are considered as thin films and particles large than a second limit are considered to be of infinite depth. Between the limiting sizes, values are interpolated. To determine the best interpolation method, samples with well-known composition (sodium chloride, albite) were milled to obtain particle standards with sizes between 1 and 30  $\mu\text{m}$ . Particles were dispersed in clean air, re-deposited on the same sampling substrate and analyzed like described above. Several non-linear interpolation schemes were tested; the best results were obtained with:

$$\langle X \rangle = \begin{cases} X_{CL} & d_g \leq d_l \\ X_{CL} + (X_{ZAF} - X_{CL}) \frac{\log(d_g/d_l)}{\log(d_u/d_l)} & d_l < d_g \leq d_u \\ X_{ZAF} & d_g > d_u \end{cases} \quad (4)$$

with  $\langle X \rangle$  the corrected concentration of a particular element in the beam interaction volume,  
 $X_{CL}$  the element concentration determined by the Cliff-Lorimer method,  
 $X_{ZAF}$  the element concentration determined by the ZAF method,  
 $d_l = 1.5 \mu\text{m}$  the lower interpolation range size limit,  
 $d_u = 30 \mu\text{m}$  the upper interpolation range size limit.

Note that the concentrations are always normalized to 100 % of the beam interaction volume. This can include **not only** the particle, **but** also the substrate. **For this reason the substrate was chosen to be composed as differently as possible to all expected particle compositions.** The correction is

identical for atomic and mass concentrations; in the present manuscript, atomic concentrations are used unless otherwise specified.

The result of the correction as function of particle size is shown on the right in Fig. 1 for 20 kV as demonstration (at 12.5 kV as used for the sample analyses, the problems are less pronounced). It becomes clearly visible that the accuracy of the quantification is strongly improved, while the remaining uncertainty originates mainly from the particle to particle variation. This uncertainty depends on the noise in the analysis system, but is also related to particle surface morphology and its variability. The latter affects the X-ray signal mainly by unknown absorption path lengths, particularly for the lighter elements, as illustrated by Fletcher et al. (2011).

Application to a sample of atmospheric particles is shown in Fig. 2. Particles dominated by Na and Cl were selected from all DPDS samples, and the positive and negative ion contributions were calculated for each particle from the determined concentration. It becomes obvious, that for a wide size range the applied correction works well and produces therefore unbiased relative concentrations for the considered elements. The outliers may occur due to noise, the negligence of C, N and O compounds or an internal mixture of sea-salt with dust (e.g., NaAlSi<sub>3</sub>O<sub>8</sub>, FeS).

### 2.3.2 Analytical measurement errors

A typical deposition sample (collected between June 21, 2013, 13:46 and June 22, 15:02, local time) was analyzed 29 times with a signal collection time per particle of 16 s. The same 300 particles were analyzed each time. For illustration of the typical precision, the particles consisting mainly of Na and Cl were selected from. Fig. 3 illustrates the average composition and standard deviation (1  $\sigma$ ) for each particle. The average values show a typical behavior for atmospheric sea-salt with a slightly depleted Cl and enriched S concentration (e.g., McInnes et al. 1994). The precision – shown as relative standard deviation – increases with particle size. This is caused by the increasing amount of material contributing to the particle's signal up to a point at about 3  $\mu\text{m}$  particles, from which the beam excitation volume is completely inside the particle. For the major compounds, the precision is in the range of 2 % relative standard deviation. For minor compounds, it is between 10 and 20 % for particles 3  $\mu\text{m}$  and larger, but can exceed 100 % for the smallest ones. The latter high uncertainties could be decreased with suitable working conditions (magnification, measurement time), but are not the focus of the present paper.

The uncertainty in particle diameter also depends on its size. For particles with 2  $\mu\text{m}$  diameter, the relative standard deviation is about 1.5 % decreasing to less than 1 % for particles larger than 3  $\mu\text{m}$ . This is in the same range as the systematic accuracy of SEM (1–2 %).

### 2.3.3 Particle classification, relative ion balance and feldspar abundance

For assessing the abundances and counting statistics of certain particle types, the particles were classified into different groups and classes. Based on the element index and additional elemental ratios, a set of rules used in former mineral dust investigations in a marine environment was applied therefore. For details refer to Kandler et al. (2011a).

In addition, a relative ion balance is defined for single particles as:

$$IB_{rel} = \frac{\langle Na \rangle + 2\langle Mg \rangle + \langle K \rangle + 2\langle Ca \rangle - \langle Cl \rangle - 2\langle S \rangle}{\langle Na \rangle + 2\langle Mg \rangle + \langle K \rangle + 2\langle Ca \rangle + \langle Cl \rangle + 2\langle S \rangle} \quad (5)$$

A positive relative ion balance – i.e. an excess of positive ions – would indicate an undetected presence of negative ions like NO<sub>3</sub><sup>-</sup> or CO<sub>3</sub><sup>2-</sup>, a negative one such of H<sup>+</sup> or NH<sub>3</sub><sup>+</sup>, which all can't be

(reliably) quantified by EDX. The relative ion balance is calculated only for particles classified into the soluble sulfate or sea-salt classes (see below for classification scheme).

For the description of feldspar abundance, we define two index values showing the vicinity for a single particle to pure feldspar or pure K-feldspar composition. These feldspar indices regard the overall contribution of feldspar-specific elements to the particle and the specific Al/Si as well as alkali/Si or K/Si ratios. Measurements based on mineral dust generated from pure granite – i.e. dust practically free of clay minerals – have shown that a threshold value of 0.80 is suitable to distinguish between pure feldspar grains and other silicates. Details of the index calculation are given in the electronic supplement in section S.1. Note that aggregated particles consisting for example of feldspar and clay minerals, quartz or soluble species would not be classified as feldspar.

### **2.3.4 Estimation of the dust contribution to each single particle in a dust / sea-salt / sulfate mixture and the size of the according dust inclusion**

Sampling was performed in a region where locally emitted sea-salt aerosol and other soluble species are mixed with long-range transported mineral dust. As in particular the mineral dust contribution is of special interest, dis-entangling the particle populations and considering them separately is an important task.

To calculate the size of a dust inclusion and the according volume fraction for an internally mixed particle from the chemical composition, the different elemental contributions have to be attributed to the dust or non-dust component. This analysis is restricted in the present work to the major compounds only. For Al, Si, P, Ti and Fe it can be safely assumed that they belong to a dust component (i.e. an inorganic, thermally stable, oxidized, non-carbonaceous compound), and S and Cl can be attributed to the non-dust component. Na, Mg, K and Ca, however, are ambiguous and can be present in fractions. Therefore, a model is needed to estimate the contribution of the ambiguous elements from the dust and non-dust component based on the single particle chemical composition.

A problem arises here from the error in chemical quantification due to matrix composition and particle geometry. While the correction outlined in section 2.3.1 adjusts the quantification accuracy of the average particle composition, for single particles because of their unknown geometry and surface orientation angles, still a considerable error in element quantification can occur. In particular, a bias between light and heavier elements can be introduced by unaccounted X-ray absorption, which can lead to under- as well as overestimation of the relative contribution of light elements (Fletcher et al. 2011). As for the present aerosol the major cations ( $\text{Na}^+$ ,  $\text{Mg}^{2+}$ ) are light in comparison to the major anions ( $\text{Cl}^-$ , S of  $\text{SO}_4^{2-}$ ), a quantification bias will lead to an error in component attribution. Particularly, an overestimation of the light elements will yield – by attribution of the ion balance excess to the dust component – to an overestimation of the dust contribution. Therefore, two model pathways are applied: an upper limit estimate, where a possibly overestimated fraction of the ambiguous elements is attributed to the dust component, and a lower limit estimate, where all ambiguous elements are attributed to the non-dust component. Details on the procedure are given in section S.2 of the electronic supplement.

The model outlined here may suffer from systematic errors:

1. In the presence of larger amount of nitrate and ammonium or organics, the dust contribution will be overestimated, as the regarded composition is fitted to the apparent particle volume. However, in Barbados the concentration of these compounds is usually small in comparison to the dust (Lepple et al. 1976; Savoie et al. 1992; Eglinton et al. 2002; Prospero et al. 2009; Zamora et al. 2011).

2. The density values are averages for the assumed components, and the real density of a particle may be smaller or larger. However, the density range for the components in question is small (dust: 2300 to 3000 kg/m<sup>3</sup>, non-dust 1800 to 2600 kg/m<sup>3</sup> at maximum), so the error is considered to be less than 10 %.

3. The mass contribution is estimated by ion charge balances. If for the ambiguous elements an inhomogeneous distribution of univalent and bivalent elements exists (e.g., univalent like Na favoring the non-dust component and bivalent like Ca favoring the dust component), an error of less than 5 % in diameter can occur. With an assumption of 5 % iron content in dust, the maximum error due to the Fe<sup>3+</sup> assumption is less than 0.2 % in diameter.

The upper and lower estimates yield diameters, which differ for the dust core diameter in average by 25 %; for 75 % of the particles the difference is less than a factor of two. From the analytical errors in ratios for major compounds (less than 10 % systematically and 6 % repetition uncertainty), a dust core size uncertainty of about 6 % is estimated, as long as the core is larger than 10 % of the particle. An overall analytical uncertainty of 15 % relative core size is estimated. In conjunction with the upper/lower limit estimates, an overall core size error of 25 % is considered appropriate.

### ***Estimation of a geometrical iron-availability index***

Iron bioavailability in general is depending on different chemical and microphysical parameters as well as residence time in chemically aggressive environments (Shi et al. 2011a; Shi et al. 2012), e.g., at low pH values under influence of sulfuric or nitric acid. If considering a homogeneous iron distribution in larger and smaller particles, it seems plausible that the distance to the surface – therefore the surface to volume ratio – should have an impact on the short-term iron accessibility (e.g., Baker et al. 2006; Shi et al. 2011b). Therefore, as first order estimate we define a geometrical surface iron availability index SIAI (after virtual dissolution of the soluble compounds) as

$$SIAI = \frac{Fe_{oxide}}{m_{dust}} 4\pi d_{v,dust}^2 \quad (6)$$

with  $Fe_{oxide}$  iron oxide mass estimated as Fe<sub>2</sub>O<sub>3</sub>,  
 $m_{dust}$  the dust elements oxide mass (refer to S.2 in the electronic supplement)  
 $d_{v,dust}$  the volume-equivalent diameter of the particle dust fraction.

It should be noted that this approach is of geometrical nature only and does not take into account environmental factors like pH and presence of ligands.

### **2.3.5 Statistical uncertainty of total volumes / masses and relative number abundances from single particle measurements**

When assessing the uncertainty of values based on counted occurrences, frequently the counting statistics are assumed to follow a Poisson distribution. However, when calculating total aerosol masses or volumes, besides the measurement errors in particular the – usually few – large particles can introduce a considerable statistical uncertainty, which is not necessarily accounted for by the distribution assumption. Therefore, estimates of the statistical uncertainty based on single particle counts for an a priori unknown frequency distribution (i. e. the counting frequency distribution modified by the also unknown particle size distribution) either require reasonable assumptions or distribution-independent estimators. In the present work, the uncertainty is estimated by a bootstrap approach with Monte Carlo approximation (Efron 1979). For the bootstrap approach, a considerable number of data replications are necessary (Carpenter et al. 2000; Pattengale et al. 2010). On the actual number, different recommendations exist with more than 1000 being among

the most common (Carpenter et al. 2000). As higher numbers lead to smaller errors in the uncertainty estimate, 10,000 replications for each sample were performed in the present work. A comparison of the results of the generally robust bootstrap approach (Efron 2003) to a more simple approach, where the counting statistics is assumed to follow a Poisson distribution, is given in section S.3 of the electronic supplement.

For the assessment of the confidence interval of relative counting abundances, a confidence interval based on a binomial distribution is used as estimate (Agresti et al. 1998), i.e. for a relative number abundance of a certain particle type class  $r$  the two-sided 95 % confidence interval is approximated (Hartung et al. 2005).

## **2.4 Collection efficiency and deposition velocity relating atmospheric concentrations to deposition rates**

### **2.4.1 Determining the size distributions from the free-wing impactor measurements**

Obtaining the atmospheric size distribution and representative contributions of particle populations with different hygroscopicity from the FWI requires two corrections. These corrections are applied to each single particle as a function of its size and composition and the thermodynamic and humidity conditions during sampling. First, a window correction is applied, accounting for the exclusion of particles at the analysis image border (Kandler et al. 2009). Second, the FWI collection efficiency is corrected. For the detailed formalism, refer to section S.4 in the electronic supplement.

Potential systematic error sources for this calculation are mainly the uncertainty in collection efficiency, given the considerable spread in data points in the according literature (Golovin et al. 1962; May et al. 1967), and any bias in particle size.

### **2.4.2 Determining the airborne size distributions from the sedimentation sampler measurements**

Sampling efficiency considerations are also necessary for the sedimentation sampler. For the supermicron particle size range sedimentation and turbulent impaction dominate the particle deposition velocity (as for example illustrated by Piskunov 2009).

A variety of models estimating the particles deposition speed were published (Sehmel 1973; Slinn et al. 1980; Noll et al. 2001; Wagner et al. 2001; Aluko et al. 2006; Piskunov 2009; Petroff et al. 2010). They yield considerable different results, possibly due to negligence of unaccounted forces (e.g., Lai et al. 2005), the way of determining the relevant friction velocity, or other model assumptions. For the present work, the formalism of Piskunov (2009) was selected, as it derives the deposition velocity rather from physical principles instead of parameterizing a specific measurement setup. **Details of the calculation procedure are given in section S.5 of the electronic supplement.** The deposition velocity calculated by different formalisms for a series of deposition samples is shown in Fig. 4.

The spread in deposition velocity for each model is caused mainly by the different wind speeds during exposure, but also by the variation in relative humidity and, to a lesser extent, by other thermodynamic conditions. However, it becomes strikingly obvious that in the size range where most of the atmospheric dust deposition occurs – i.e. between 2 and 50  $\mu\text{m}$  in diameter at Barbados (Mahowald et al. 2014; van der Does et al. 2016) –, the models disagree by more than two orders of magnitude. Besides the uncertainty derived from selection of a particular model, the sphericity assumption and the related drag effects may lead to a bias in deposition flux, most probably mainly

influencing the turbulent deposition regime around 10  $\mu\text{m}$  particle diameter. An additional measurement bias might be introduced by the parallelism assumption underlying all the stable boundary layer calculations, i. e. that the air flow must be parallel to the plate. While the vertical component of the wind speed under atmospheric conditions is usually small in comparison to the horizontal ones, still ‘inlet’ losses might occur even due to small non-parallel components. These inlet losses are expected to affect mainly the largest particles sizes.

### 2.4.3 Impactor inlets

The impactor sampler was used with two types of inlets. For particles larger than approximately 2.5  $\mu\text{m}$  aerodynamic diameter, a pseudo-isoaxial inlet orientation with sub-isokinetic sampling was used. Smaller particles were collected with an omnidirectional inlet. As particles were analyzed separately for each size class, the inlet efficiency does not play a primary role for the results, still it must be considered. Literature on an accurate estimation of inlet transmission for a ratio between ambient wind speed and impactor inlet flow velocity in the range of 100:1 **doesn't exist**. However, from Paik et al. (2002) and Hangal et al. (1990) in conjunction with the observation of Li et al. (2002) regarding the applicability of thin walled nozzle formulas to blunt samplers, it may be **concluded** that:

a) particles larger than 2.5  $\mu\text{m}$  aerodynamic diameter would be increasingly enriched with increasing particle sizes. Enrichment factors for thin-walled nozzles would be in the range of 2–4 for 10  $\mu\text{m}$  particles and 20–50 for 100  $\mu\text{m}$  particles. As the sampler had a blunt inlet, the actual enrichment factors are probably considerably lower.

b) particles smaller than 2.5  $\mu\text{m}$  would be comparatively unbiased at low Stokes numbers; see also Wen et al. (2000).

For a dry aerosol, these size-selective inlet losses would not considerably bias the relative chemical composition. In the present humid environment with partly soluble species, though, it can lead to an overestimation of non-hygroscopic species for particle sizes in the vicinity of the inlet cut-off, if the hygroscopic growth is not explicitly considered. The problem is somewhat diminished by the fact that by water-absorption the density of the particles decreases and, consequently, the Stokes number increases only sub-proportionally to the square of the particle diameter. Nevertheless, the hygroscopic growth should be explicitly accounted for. Therefore, **the hygroscopicity model** is applied based on the measured geometric diameter and chemical composition, and ambient chemical compositions are computed.

## 2.5 Modelling deposition statistics and artifacts of mixing state

When particles are deposited to a substrate, they might touch each other and form an internal mixture, which is not representative for the atmosphere. While the lower limit of coincidental internal particle mixture on a substrate is easily defined – it equals the ratio of the area covered by particles to the total analyses area for an infinitesimally small depositing particle – the assessment is much more complex for larger particles following a wide size distribution function.

Therefore, in the first step the deposition process was simulated by a series of Monte Carlo models. For input, the average size distribution measured at Cape Verde (Kandler et al. 2011b) – hereafter CV-ground – and the median one measured airborne for aged dust (Weinzierl et al. 2011) – hereafter CV-air – were used. These size distributions mainly differ in the concentration of supermicron particles. The deposition velocity formulation after Piskunov (2009) was used. The modeled deposition area is 5 mm x 5 mm, meteorological conditions were assumed as totally dry, 20 °C, sea

level pressure and a friction velocity of 0.2 m/s. Particles were virtually dropped onto the deposition surface until either a certain fractional area coverage by particles or a simulated deposition time limit was reached. Eighteen different area coverages were simulated for a two-component external mixture (particle density 2200 kg/m<sup>3</sup>) with components number ratios of 50 % / 50 %, 75 % / 25 %, 90 % / 10 %, 95 % / 5 %, 97 % / 3 %, and 99 % / 1 % for CV-ground, and nine area coverages with number ratios of 50 % / 50%, 90 % / 10 %, and 99 % / 1 % for CV-air. Each model was run 1000 times (200 times in case of 0.1 and larger fraction area coverages) to assess the statistical uncertainty. In a second series, for CV-ground a tri-component external mixture of sodium sulfate (particle density 1770 kg/m<sup>3</sup>), dust (2700 kg/m<sup>3</sup>) and sea-salt (2170 kg/m<sup>3</sup>) was used as input. The size-dependent component number contributions were taken from measurements at Cape Verde (Schladitz et al. 2011). After the simulated deposition, particle agglomerates on the substrate with touching contours were merged into a new particle with the sum of the volumes and proportionate chemical composition.

To investigate the relevance of mixing artifacts caused by particle sampling, the sensitivity of SEM/EDX analysis has to be considered. Internal mixtures can be only detected by SEM/EDX, if the minor component exceeds the limit of detection. At an acceleration voltage of 12.5 kV the primary X-ray excitation volume is in the range of 0.5 µm to 1.5 µm diameter, depending on the matrix elements (Goldstein et al. 2003). As we consider mainly supermicron particles, the excitation volume is expected to be mainly inside the particles. According to our experience an X-ray peak becomes detectable at about 0.3 % concentration. Therefore, a 1 % contribution of an element to the particle volume will be definitely detectable. Thus, a particle containing more than 1 % material from another particle type is considered as detectable mixture in the model. A particle containing more than 20 % is denominated as strong internal mixture. Note that for smaller particles, when the excitation volume would extend into the substrate, larger contributions to the particle volume would be required.

Besides these fundamental considerations, in the second step a mixing model was applied to each sample, based on its measured composition. Random particles were virtually selected from the pure components of the measured set of particles and placed at random positions inside a virtual area with the same size as the one analyzed in SEM/EDX, until the same area coverage as of the real sample was reached. Internal mixtures artificially produced on the substrate were counted, if their mixing would have been detected by SEM/EDX applying the rules for mixed particle classification. This process was repeated 10,000 times. The upper 95 % confidence interval limit of mixtures modeled by the Monte Carlo simulation was considered as limit of detection for internal mixtures, and the median of the produced mixtures was regarded as systematic error and was subtracted from the mixtures detected in the real samples.

In the third step, the single mixing probability (SMP) for each binary pure compound combination was calculated by selecting 100,000 random pure-composition particles from the measured data set for each sample, mixing them virtually and determining, whether they would be detected as mixed. This was carried out one time without any size restrictions and a second time with only selecting particles not more than a factor of 3 different in size. The latter was done to account for the fact that in a turbulent environment and in the regarded size range, the collision efficiency is highest for particles of similar size (Pinsky et al. 1999; Wang et al. 2005).

### **2.5.1 Simulating particle mixtures due to longer exposure times**

While in the modeling section particles are assumed to be spherical, this is typically not the case for natural aerosol like mineral dust particles. Therefore, a second approach based on particles images was used to estimate the effect of internal particle mixture on the substrate, i.e. taking into account the real particle shapes. Due to the large number of images required, this approach could only be used for assessing the size statistics, but not for the chemical composition. All segmented images of each deposition sample were subject to particle size analysis. In following steps, a number of 2, 3, 5, 10, 15, or 20 segmented images of the same sample were combined into a single image, simulating an extension of exposure time by the according factor. This approach inherently assumes a constant size distribution during exposure and a random particle deposition. The resulting images were then subject to the same particle analysis, yielding apparent size distributions after a coincidental mixing. In contrast to the pure modeling approach, here the true size distribution is not known because even the lowest coverage samples might contain internal mixtures. Certainly though, the lowest coverage sample is closest to the true size distribution and therefore will be used as reference.

## **3 Results and Discussion**

### **3.1 Uncertainty of measurements for the new collection techniques and determination of mixing state**

#### **3.1.1 Area homogeneity of collected particles**

##### ***Free-wing impactor (FWI)***

To assess the homogeneity of particle distribution, for each sample the center 80 mm<sup>2</sup> (about 65 % of the total sample area) were scanned with approximately one thousand SEM images (approximately one third coverage), and the average particle density was determined for each mm<sup>2</sup> as function of  $d_g$ . For particles between 4 μm and 8 μm in diameter (see Fig. S 5 in electronic supplement) no systematic bias in particle density is visible, except for a slight enhancement toward the borders in a few cases. The remaining variability remains probably linked to statistical uncertainty and surface defects interpreted as particles by the automatic segmentation algorithm. However, the density variations between each mm<sup>2</sup> remain below a factor of 2. As commonly 20 to 100 mm<sup>2</sup> are analyzed, the inhomogeneity can be regarded as minor error. For larger particles, the uncertainty due to counting statistics becomes dominant.

##### ***Dry particle deposition sampler (DPDS)***

Similar to above, for the DPDS deposition density homogeneity was assessed, but in this case nearly all of the central 80 mm<sup>2</sup> were scanned. In about half of the samples, a crescent-shaped density gradient can be observed (see Fig. S 6 in electronic supplement). This gradient most probably originates from a stationary wave introduced by the recession of the sample substrate slightly below the primary plane of the DPDS. Depending on the analysis location, a bias in the range of factor 2 to 3 in deposited particle number can occur. Therefore, the fields of analysis for the chemical composition and size distribution discussion below were homogeneously distributed over the sample surface at a regular distance. Also with the DPDS, for larger particles the uncertainty due to counting statistics becomes dominant.

### 3.1.2 Impact of area coverage and counting statistics on size distribution and total volume

Fig. 5 shows the apparent number and volume size distributions of particles deposited from aerosols with CV-ground (a, b) or CV-air (c, d) size distribution for different area coverages, equaling different exposure times. As it is to be expected, for short exposure times there is a considerable counting error, which decreases to less than 10 % for the smaller particles at area coverages of 0.01 and higher. In median, no particle larger than 50  $\mu\text{m}$  would be detected in deposition area for area coverages smaller than 0.0025, and more than 0.005 are necessary to collect more than 5 particles (not shown in graphs). As opposing trend there is a bias in size distribution towards lower concentrations and larger particles, which starts getting relevant at coverages of 0.1. This bias is introduced by the coincidental clumping, a second particle depositing on an already deposited one. As a result, for the given aerosol size distributions, an area coverage of 0.03 to 0.05 is most appropriate to get a size distribution influenced least by counting errors and sampling/mixing bias.

Generally similar, but more pronounced effects can be observed, if the second approach – simulating longer exposure times by combining real microscope images – is used. Fig. 6 shows for three samples – low (a, b), medium (c, d) and high (e, f) area coverages – the evolution of the size distribution due to simulated longer exposure times. In case of high dust deposition rates and long exposure times, particles smaller than 10  $\mu\text{m}$  in diameter would be underestimated by a factor of more than 2, while larger particles would be considerable overrepresented. A shift in the modal diameter of 50 % towards larger size could be the result. However, at the large end of the volume size distribution, counting statistics might considerably influence the total particle mass uncertainty, even at these long simulated exposition times.

If total mass deposition is estimated from the microscope images, one can set up a relation of total volume and apparent area coverage, which might serve as a quick estimate of total deposited particle mass (Fig. 7). If the result of the fit function is multiplied with an approximate particle density, the result gives the deposition as  $\text{mg}/\text{m}^2$  with an uncertainty of factor 2. As expected, the fit function starts to underestimate the volume / mass for high area coverage.

When calculating total mass / volume from small amounts of material, special attention has to be paid to the errors introduced by counting statistics. To assess the uncertainty, two size distributions were considered with different abundance of large particles. Using the CV-ground size distribution, we observe an uncertainty of a factor of 2 for the total mass (95 % two-sided confidence interval), when 3,000 particles are counted, which are equivalent to 8  $\mu\text{g}$  of mass. If only particles between 1 and 32  $\mu\text{m}$  in diameter are regarded, a relative uncertainty of 20 % is achieved with 1500 particles. When analyzing about 100  $\mu\text{g}$  of particle mass, the statistical error is in the range of 30 % mass in case of CV-ground size distribution and 15 % for CV-air. Table S 3 in the electronic supplement gives more details for deposition simulation results based on a typical area, which would be used for automated single particle analysis. It can be concluded here that a minimum number of 5,000 to 10,000 single particle measurements would be desirable to stabilize the total mass concentration in the range of 10 % uncertainty. As this number is usually not reached in SEM studies (e.g., Reid et al. 2003; Coz et al. 2009; Kandler et al. 2011a), additional attention should be paid to larger particles, e.g. by analyzing larger sample areas, to decrease the uncertainty in mass. Note that the same considerations in principle apply to bulk investigations, when only small amounts of mass are analyzed, but are not commonly stated.

### 3.1.3 Amount of coincidental internal particle mixtures

When assessing the mixing state of particles from an offline single particle technique, coincidental internal particle mixture has to be taken into account. Higher area coverage, as to be expected, yields higher mixture probability. In particular, if components are present in equal abundances, mixing probabilities become high already for covered area fraction of a few percent. As an example, Fig. S 7 in the electronic supplement shows the upper 95 % confidence limit – i.e. the detection limit for mixtures – of apparent fractions of internally mixed particles for a two-component system as function of source component ratio and area coverage for detectable strong internal mixtures (refer to section 2.5; data are given also in the electronic supplement, Table S 4 and Table S 5). No significant mixture for submicron particles occurs in these cases. Note also the different size maximum for strong versus detectable mixture.

Applying the same model type based on the CV-ground size distribution to a ternary modal composition distribution of sulfate, sea-salt and dust as described in section 2.5, mixing probabilities for a specific atmospheric composition can be estimated (Fig. 8). It becomes instantly obvious that the mixing probabilities for this atmospherically more relevant aerosol model are much lower than in the homogeneous case. Mixtures between sulfate and sea-salt as well as ternary mixture are absent. The relative fraction of internally mixed particles is lower by an order of magnitude. This can be explained by the fact that the defined relative detection limits of 20 % and 1 % restrict the detection of mixing to mixing partners not differing in size by more than a factor of 1.59 (strong mixing) and 4.6 (detectable mixing). But because different aerosol type are mainly present in different size regimes here (Schladitz et al. 2011), the mixture can only be efficient for size ranges, where these component have an overlap. In general, however, also here mixture increases with particle size.

It can be concluded here that mixing studies for large particles are generally very difficult. Many particles need to be collected in total to ensure reliable counting statistics, which leads in consequence to high mixing probabilities. This issue is of less concern for particles smaller than 10  $\mu\text{m}$  for the given size distributions and in cases, where the aerosol has a strong dependence of composition on particle size. It also emphasizes that mixing studies should be accompanied by mixture modeling as performed below.

## 3.2 Field Measurements – methodological aspect

### 3.2.1 Comparison of atmospheric size and volume concentrations

Using the FWI sampling efficiencies outlined in section 2.4.1 and the DPDS deposition velocities from 2.4.2, one can calculate the atmospheric size distribution derived by the two techniques. Fig. 9 shows the average size distributions for the post- and pre-storm periods based on different deposition velocity models for total and upper estimate dust mass concentrations. The lower dust estimate (not shown) exhibits qualitatively the same behavior. It is evident that there is a large discrepancy between the different models as well as between the DPDS and FWI measurements. The discrepancy is clearly larger than the statistical uncertainties. While the total mass median diameter derived from DPDS (Piskunov model) is around 5  $\mu\text{m}$  particle diameter, for the FWI it is approximately 25  $\mu\text{m}$ . A dust size distribution measured in the Saharan Air Layer in 2.3 km altitude (computed from data shown by Weinzierl et al. 2017) contains the same mode around 4  $\mu\text{m}$  diameter, but shows a secondary maximum at 10  $\mu\text{m}$ , which is not found by the ground-based measurements. It is interesting to note that these values get closer, when only the dust fraction is considered, indicating a connection of the discrepancy with the hygroscopic growth (e.g., growth or density misestimate).

Three other reasons for the discrepancy might be for the FWI an uncertain collection efficiency, particle losses due to non-parallel flow for the DPDS, and non-parallel sampling times. The FWI has 50 % collection efficiency around 11  $\mu\text{m}$  particle aerodynamic diameter, so for smaller particles – the majority by far – the efficiency correction function may yield unrealistic values. The DPDS model assumptions require a well oriented flow. At the high wind speeds, a non-zero angle-of-attack flow (from below) might lead to considerable particle losses for the larger particles. This might for example be caused by an increased boundary layer thickness over the lower plate. Such an angular flow was observed at the measurement site due to the cape orography. Finally a discrepancy in sampling times (DPDS: approximately 1 day, FWI: approximately 1 hour) may yield a bias. However, as similar differences are observed for all samples, the latter is most probably a minor aspect.

When total mass is calculated from deposition, it can be compared to dust concentration measurements with a high volume filter sampler. Fig. 10 shows time series of mass concentrations measured by the high-volume sampler, estimated from dry deposition measurements as well as the raw dry deposition flux densities. For dry deposition uncertainties derived from the low / upper estimates as well as from counting statistics are shown. A few things can be learned from this data. With respect to the deposition model, the Piskunov model performs rather well. The average of the high-volume sampler mass concentration time series (see Table 1) is close to the lower estimate of the Piskunov model, while the higher estimate overestimates the mass concentration. The other models deviate considerably more, as to be expected from the deposition velocity differences (Fig. 4). The ratio of the mass concentration estimate to the mass flux density varies over slightly more than one order of magnitude, depending mainly on size distribution and wind conditions. High volume and deposition-estimated mass concentrations as well as the mass flux densities follow qualitatively the same pattern in showing low concentration and high concentration periods. The absolute numbers, however, deviate significantly. For sub-periods, the correlation quality seems to be different. For example, starting from June 21, the correlation of mass flux with high volume mass concentrations seems to be better than the one with deposition estimated concentrations; for the period before June 21 situation is converse. No direct link of the correlations with any meteorological variable was found, indicating that the deviations depend in part on erroneous assumptions in the model. For example, tuning other deposition velocity models by arbitrary factors can lead to a better agreement of actively and passively determined mass concentrations for this particular data set (Fig. S 10 in electronic supplement), but the data basis is too small for a robust tuning without physical backing. Moreover, disagreement might also be caused by physical measurement biases like unknown size-dependent inlet efficiency for the high-volume sampler or angular inflow for the DPDS.

### 3.3 Field Measurements – atmospheric and aerosol aspects

#### 3.3.1 Aerosol composition

Overall aerosol composition (i.e. the relative number abundance of the different particle groups) was measured by electron microscopy single particle analysis (Fig. 11). The relative abundance of soluble sulfate is highest for the smallest particle sizes, which is in good accordance with previous measurements in the eastern Atlantic Ocean (Kandler et al. 2011a). After the storm passage, higher sulfate abundances – soluble as well as stable – are observed in 2013, which are similar to those observed in 2016. The sea-salt abundance is higher for the pre-storm period in 2013, which is in agreement with the wind speeds observed (see below). In 2016, a much higher abundance of small Fe-rich particles (contained in the oxides/hydroxides class) is observed compared to the pre-storm period in 2013. For the post-storm period in 2013, minor amounts of these particles are visible.

Overall, an average dust deposition of  $10 \text{ mg m}^{-2} \text{ d}^{-1}$  (range  $0.5\text{--}47 \text{ mg m}^{-2} \text{ d}^{-1}$ ) is observed (Fig. 12). While a strict disambiguation can't be done for elements also found in sea-salt, Al, Si, P, Ti, and Fe are most likely derived from dust only and are therefore also shown in the graph. At Barbados, Fe contributes  $0.67 (0.01\text{--}3.3) \text{ mg m}^{-2} \text{ d}^{-1}$  to deposition, while phosphorous adds only  $0.001 \text{ mg m}^{-2} \text{ d}^{-1}$ ; however, P is below the detection limit on two thirds of the days. The cumulative size distribution shows that in particular P and Ti are located preferentially within smaller particles. Al, Si and Fe show generally a similar size distribution.

Recently, the impact of mineral dust composition on clouds via the ice phase has attracted attention. Feldspar particles and in particular K-feldspars are discussed as most efficient ice nuclei (Atkinson et al. 2013; Augustin-Bauditz et al. 2014; Harrison et al. 2016). Therefore, Fig. 13 shows the total feldspar and K-feldspar number fractions with respect to all silicates as determined by the feldspar indices. In general, approximately 3 % of the silicates are pure feldspar particles and slightly less than 1 % K-feldspars. No significant variation is visible for the different periods and years at Barbados, whereas particles collected in Morocco (Kandler et al. 2009) showed slightly higher values. In this respect, the dust composition at Barbados is constant over time. Note that the bulk feldspar contents of the samples might be higher, as the applied technique only detects pure feldspar grains.

### 3.3.2 Airmass history and potential aerosol sources

The airmass provenance of the sampling periods in 2013 and 2016 is generally similar. The trajectories mostly followed the trade-wind path from North-West Africa and East Atlantic Ocean to Barbados (Fig. S 8 in electronic supplement). In 2013, the air was coming more frequently from Western Africa than in 2016. After the tropical storm Chantal in 2013, the airmass origin shifted slightly to more southern regions. In a few cases in 2013, air from the North-West Atlantic Ocean was recirculated into the trade-wind path.

The sea-salt deposition rates are not linked to air mass provenance (not shown). The dust provenance for both years (Fig. 14 a, b) is – as expected – pointing to West Africa. This source region is also identified by isotope measurements in July/August 2013 (Bozlaker et al. 2018). The soluble sulfate deposition (Fig. 14 e, f) is generally linked to three regions, the Atlantic Ocean, West Africa and south west Europe. In particular in 2016, the sulfate sources appear to be located more in Europe and less in Africa. The relative ion balance (Fig. 14 g, h) shows mostly slightly negative values indicating presence of  $\text{NH}_4^+$  or  $\text{H}^+$ . Interestingly, a positive ion excess is observed for European sulfate in 2016, indicating possible presence of  $\text{NO}_3^-$ . These observations support the hypothesis that nitrate as well as sulfate associated with dust sources is likely to be from Europe (e.g., anthropogenic origin; Li-Jones et al. 1998).

Iron contribution from dust is of particular interest for marine ecosystems. Therefore, Fig. 14 c and d show the silicate SIAI as proxy for quick iron availability. It is obvious, that the iron-containing silicate particle source is located in West Africa. Northern and southern West Africa as source regions can't be distinguished after trans-Atlantic transport, in contrast to investigations close to the source (Kandler et al. 2007). This is consistent with observations based on isotope analysis, where also a homogeneous composition has been observed at Barbados (Bozlaker et al. 2018). A slightly higher SIAI can be observed in 2016 than in 2013, while the dust deposition rates in contrast are lower. While the total iron deposition correlates well with dust deposition (not shown), similar to observations by Trapp et al. (2010), for the SIAI an inverse relationship is found at Barbados with higher dust deposition rates leading to lower ratios of SIAI to total dust. This correlates to previous

findings, where iron solubility decreased with increasing dust concentration (Shi et al. 2011b; Sholkovitz et al. 2012), though no direct causal relationship can be derived (Shi et al. 2011a).

### 3.3.3 Sea-salt composition

When considering sea-salt composition, it is assumed generally that except from the sulfate content, aerosol produced from sea-water has a major composition resembling the bulk sea-water (Lewis et al. 2004). However, it was recently shown in the Arctic that a fractionation can occur also with respect to the major composition (Salter et al. 2016). At Barbados, an increasing positive deviation from the nominal value of 0.022 with decreasing particle size is observed for the Ca/Na atomic ratio of sea-salt particles (Fig. 15). This indicates that the same effects found by Salter et al. (2016) are present in Caribbean sea-salt production. According to the authors, these might be linked to an enrichment of Ca in sea surface micro-layers, but details are not yet known.

### 3.3.4 Abundance of mixed particles

If we consider the abundance of mixed particles at Barbados, a complex picture emerges as function of particle size, time period and available mixing partners (Fig. 16). It can be observed that the total deposition rate for all particle types is linked to the wind speed, what is to be expected from the physical process (see for example Fig. S 9 in electronic supplement). The higher sea-salt deposition rates and also higher concentrations in 2013 in comparison to 2016 are also linked to the wind speed, showing the local sea-salt production. In contrast, the dust concentration is slightly lower for higher wind speeds (Fig. S 9) for both years. With increasing particle size, the relative abundance of internal dust/sea-salt mixtures increases (Fig. 16), but these mixtures only occur when considerable amounts of sea-salt are present. This is different for the internal mixture with sulfate. While there are similar ratios of dust and sulfate particles observed in the second half of the 2013 data as in 2016, in 2013, dust/sulfate mixtures are practically absent. Assuming that higher wind speeds in 2013 should lead to more internal mixing due to increased turbulence, this is clearly indicating that in contrast to the sea-salt/dust mixture, the sulfate/dust mixture has a non-local origin (e.g., Usher et al. 2002).

This is corroborated by the dependence of internal mixtures relative abundance on the single mixing probability (Fig. S 11 in the electronic supplement). If one considers here the binary number fraction of mixed particles – i.e. ratio of binary mixed particles to pure compounds – as function of the size-restricted single mixing probability, there is a weak positive correlation for dust/sea-salt mixtures for particles larger than 2  $\mu\text{m}$  diameter, but no correlation for dust/sulfate mixtures. Moreover, for similar single mixing probabilities, the binary number fraction of mixed particles appears slightly higher for higher deposition rates. As the collision efficiency depends on the square of the number concentration (Sundaram et al. 1997), this supports the hypothesis of a locally produced internal mixture of sea-salt and dust and a non-local production of sulfate and dust, the latter having most probably cloud processing involved (Andreae et al. 1986; Niimura et al. 1998).

The overall ratio of dust/sea-salt internal mixture abundance to all dust- and sea-salt-particles increases from 0.01–0.03 for 1  $\mu\text{m}$  particles to 0.1–0.7 for particles of 8–16  $\mu\text{m}$  in diameter, whereas for dust/sulfate mixtures the ratio of 0.01–0.02 is not dependent on particle size. Denjean et al. (2015) report mixed particle abundances of 0.16–0.3, but do not state a size range, so the data can't be compared directly.

If the findings on Barbados are compared to measurements in the eastern Atlantic Ocean (Kandler et al. 2011a), a generally lower abundance of internally mixed particles with respect to dust/sulfate is

observed, while comparable abundances of sea-salt/dust mixtures are found. While the latter can be explained by similar wind conditions and comparable single mixing probabilities, the former seems to be caused by different aging conditions. Dust arriving over Barbados is transported mostly in the dry Saharan Air Layer (e.g., Schütz 1980), while dust arriving during winter-time at Cape Verde is transported inside the humid marine boundary layer (Chiapello et al. 1995; Kandler et al. 2011b). Therefore, considerably higher chemical processing rates at Cape Verde due to the higher humidity can be expected (Dlugi et al. 1981; Ullerstam et al. 2002), even though the transport time is most likely shorter. In addition, the boundary layer most probably provides higher concentrations of sulfur compounds for reaction (Davison et al. 1996; Andreae et al. 2000).

### ***Change in dust behavior due to internal particle mixing***

If dust particles become internally mixed, their mass, size and hygroscopic behavior change. Therefore, they will have modified deposition velocities as well as hygroscopic properties. Fig. 17 shows the increases in deposition velocities for mixed particles observed at Ragged Point in 2013 and 2016. For the both mixtures (dust/sea-salt and dust/sulfate), an increase at ambient conditions of a factor of 2–3 is observed for submicron dust particles, which rises to a factor of 5–10 for particles of 3  $\mu\text{m}$  dust core diameter. As a result, the dust average deposition velocity for particles between 1 and 10  $\mu\text{m}$  aerodynamic diameter is increased by 30–140 % at ambient conditions (Fig. 18). Considering a mass mean aerodynamic diameter in deposition of 7.0  $\mu\text{m}$ , at ambient conditions dust deposition velocity is 6.4 mm/s, which is an enhancement by approximately 35 % over the unmixed state. This overall value is in the range estimated by Prospero et al. (2009). The enhancement will become more pronounced at higher humidities. It has to be emphasized that this estimate is a lower limit, as there most likely exist mixed particles with a smaller contribution of hygroscopic material, which remaining undetected by our analytical approach. At higher humidities, this smaller contribution nevertheless will increase the deposition velocity of the mixtures. While we observe similar relative abundances of mixed particles to previous work in Asian dust outflow Zhang (2008), our estimate of impact on deposition is **considerably** higher. **This** is mainly related to the use of the Piskunov model, **which takes** into account turbulent deposition over a Stokes settling approach.

## **4 Summary and Conclusions**

Aerosol deposition measurements by means of passive samplers were carried out on a daily basis at Ragged Point, Barbados in June/July 2013 and August 2016. In addition, active aerosol collection was performed with a cascade and a novel free-wing impactor. Size, shape and composition of about 110,000 particles were determined by electron microscopy. Focus was placed in this work on measurement accuracy of chemical composition and mixing state determination for individual particles.

Ragged Point, in particular in 2013, is a high-wind and high-humidity environment, which considerably influences representativeness and accuracy of the different sampling techniques. A deposition model including chemistry-dependent hygroscopic growth was adapted to the sampling situation to assess atmospheric concentration of large particles. Fair agreement was reached between passive and active techniques regarding mass concentration, but clear discrepancies were observed for particle size distribution.

Special attention was paid to the mixing state of dust particles. A model was developed to assess the mixing state of airborne particles by correcting for sampling artifacts due to particle overload leading

to coincidental internal mixing of particles on the substrate (i.e., not representative for the airborne state). Different approaches were tested based on model size distributions and observed particle deposition images. It was found that the size distribution is only weakly affected for substrate area coverages with particles below 10 %. The chemical composition of mixtures, however, is already affected at much lower area coverages of < 1 %.

During our measurement campaigns, the aerosol was dominated by dust, sea-salt and sulfate in changing proportions. The sea-salt concentration at Ragged Point is mainly depending on wind speed. Back trajectory analysis showed that dust is originating from the usual sources in West Africa, and the dust composition with respect to different silicate phases was not varying. Sulfate showed three major potential source areas, Africa, Europe and Atlantic Ocean. Particularly in 2013, sulfate was more linked to the African source, while in 2016 southwest Europe occurred as potential source, with a possible contribution of nitrate.

It was further found that internal mixing of dust and sea-salt is depending on local wind speed, and we, thus, hypothesize that it is produced locally, most likely by turbulent processes. In contrast, mixtures of dust and soluble sulfates are presumably not produced locally, but may have formed during the inter-continental transport. Even though the overall amount of internally mixed particles is comparatively low, a considerable impact on total dust deposition velocity is estimated. In addition, a pathway is hypothesized by which the ice-nucleation efficiency of dust can be increased by mixing with soluble compounds during or after the long-range transport.

For future work, some conclusions can be drawn from our observations:

- If different techniques for deposition and/or atmospheric concentration measurements are compared, it is crucial to measure particles size distributions. We observed in some cases that total mass concentration can compare rather well, even though size distributions – and therefore collection efficiencies – are considerably different.
- A better understanding – in theory as well as in experimental use – of particle deposition and collection efficiencies is required in particular under high wind-situations, where turbulent transport has a considerable impact. This most probably applies to a wide range of deposition samplers, not only these used in this work.
- When mixing state investigations are done based on collected aerosol particles, the impact of coincidental mixtures on the substrate must be assessed, unless the area coverage with particles is very low (<< 1%). This is particularly the case for larger particles (> 5 µm diameter) and for aerosols in the same size range, where similar abundances of different mixing partners exist.
- Internal particle mixing most likely has a considerable influence on dust deposition speed. Future models regarding dust dry deposition should take a deposition speed enhancement by internal mixing into account. The internal mixing likely also increases its efficiency to be activated into cloud droplets (Kelly et al. 2007; Kumar et al. 2011). As a result internally mixed dust particles may be subject to preferential removal by wet deposition. However, more systematic investigations are needed to better understand the mixing processes.
- Also the intensity of chemical processing might be affected by the internal mixing, when the particles are activated more efficiently into cloud droplets. For example, the iron solubility for these particles might increase (Shi et al. 2009).

- With respect to a potential cloud impact, the observed fraction of dust mixed with soluble species can be used as input parameters for cloud condensation nuclei parameterizations. Regarding the impact of mixing on dust ice nucleation activity, on one side studies show a deactivation of dust for high solute concentrations (Zobrist et al. 2008; Iwata et al. 2018). On the other side, the more efficient activation into cloud droplets might increase the overall availability of dust for immersion freezing. Further studies are needed to assess and constrain the effects.

## 5 Data availability

The data sets of all particles used for this investigation including particle size, shape, and composition are given as text tables in the electronic supplement along with a data overview.

## 6 Author contribution

KK designed the experiment. KK and MH carried out field work in 2013. MP and CP carried out the field work in 2016. KK and KS analyzed the samples. KK programmed the models and data processing code. KK, SW and ME analyzed data and prepared the manuscript. All authors contributed in data discussion and manuscript finalization.

## 7 Competing interests

The authors declare that they have no conflict of interest.

## 8 Acknowledgements

We acknowledge financial support from the German Research foundation (DFG grant KA 2280/2-1 and KA 2280/3-1). We thank Joseph Prospero for his valuable comments on the manuscript and discussion; his wind and mass concentration data were obtained under National Science Foundation (NSF) grant AGS-0962256. The authors gratefully acknowledge the NOAA Air Resources Laboratory (ARL) for the provision of the HYSPLIT transport and dispersion model and/or READY website (<http://www.ready.noaa.gov>) used in this publication. **We thank the two anonymous reviewers for their useful comments.**

## 9 Literature

- Agresti, A., B. A. Coull (1998): Approximate Is Better than "Exact" for Interval Estimation of Binomial Proportions. *Am. Stat.* 52(2), 119-126. doi: 10.2307/2685469
- Aluko, O., K. E. Noll (2006): Deposition and Suspension of Large, Airborne Particles. *Aerosol Sci. Technol.* 40(7), 503-513.
- Andreae, M. O. (1995). Climatic effects of changing atmospheric aerosol levels. Future climates of the world: a modelling perspective. A. Henderson-Sellers. Amsterdam, The Netherlands, Elsevier. **16**: 347-398.
- Andreae, M. O., R. J. Charlson, F. Bruynseels, H. Storms, R. V. Grieken, W. Maenhaut (1986): Internal Mixture of Sea Salt, Silicates, and Excess Sulfate in Marine Aerosols. *Science* 232, 1620-1623.
- Andreae, M. O., W. Elbert, R. Gabriel, D. W. Johnson, S. Osborne, R. Wood (2000): Soluble ion chemistry of the atmospheric aerosol and SO<sub>2</sub> concentrations over the eastern North Atlantic during ACE-2. *Tellus B* 52(4), 1066-1087. doi: 10.3402/tellusb.v52i4.17087

- Armstrong, J. T. (1991). Quantitative elemental analysis of individual microparticles with electron beam instruments. *Electron probe quantitation*. K. F. J. Heinrich and D. E. Newbury. New York, Plenum Press: 261-315.
- Ashbaugh, L. L., W. C. Malm, W. Z. Sadeh (1985): A residence time probability analysis of sulfur concentrations at grand Canyon National Park. *Atmos. Environ.* 19(8), 1263-1270. doi: 10.1016/0004-6981(85)90256-2
- Atkinson, J. D., B. J. Murray, M. T. Woodhouse, T. F. Whale, K. J. Baustian, K. S. Carslaw, S. Dobbie, D. O'Sullivan, T. L. Malkin (2013): The importance of feldspar for ice nucleation by mineral dust in mixed-phase clouds. *Nature* 498, 355-358. doi: 10.1038/nature12278
- Augustin-Bauditz, S., H. Wex, S. Kanter, M. Ebert, D. Niedermeier, F. Stolz, A. Prager, F. Stratmann (2014): The immersion mode ice nucleation behavior of mineral dusts: A comparison of different pure and surface modified dusts. *Geophys. Res. Lett.* 41(20), 7375-7382. doi: 10.1002/2014gl061317
- Baker, A. R., T. D. Jickells (2006): Mineral particle size as a control on aerosol iron solubility. *Geophysical Research Letters* 33(17), L17608. doi: 10.1029/2006gl026557
- Bauer, S. E., M. I. Mishchenko, A. A. Lacis, S. Zhang, J. Perlwitz, S. M. Metzger (2007): Do sulfate and nitrate coatings on mineral dust have important effects on radiative properties and climate modeling? *J. Geophys. Res.* 112, D06307. doi: 10.1029/2005JD006977
- Bond, T. C., G. Habib, R. W. Bergstrom (2006): Limitations in the enhancement of visible light absorption due to mixing state. *J. Geophys. Res.* 111, D20211. doi: 10.1029/2006JD007315
- Bozlaker, A., J. M. Prospero, J. Price, S. Chellam (2018): Linking Barbados Mineral Dust Aerosols to North African Sources Using Elemental Composition and Radiogenic Sr, Nd, and Pb Isotope Signatures. *J. Geophys. Res.* 123(2), 1384-1400. doi: 10.1002/2017JD027505
- Carpenter, J., J. Bithell (2000): Bootstrap confidence intervals: when, which, what? A practical guide for medical statisticians. *Stat. Med.* 19(9), 1141-1164. doi: 10.1002/(sici)1097-0258(20000515)19:9<1141::aid-sim479>3.0.co;2-f
- Chiapello, I., G. Bergametti, L. Gomes, B. Chatenet, F. Dulac, J. Pimenta, E. Santos Soares (1995): An additional low layer transport of Sahelian and Saharan dust over the North-Eastern Tropical Atlantic. *Geophys. Res. Lett.* 22(23), 3191-3194. doi: 10.1029/95GL03313
- Choobari, O. A., P. Zawar-Reza, A. Sturman (2014): The global distribution of mineral dust and its impacts on the climate system: A review. *Atmos. Res.* 138(0), 152-165. doi: 10.1016/j.atmosres.2013.11.007
- Cliff, G., G. W. Lorimer (1975): The quantitative analysis of thin specimens. *J. Microsc.* 103(2), 203-207. doi: 10.1111/j.1365-2818.1975.tb03895.x
- Coz, E., F. J. Gómez-Moreno, M. Pujadas, G. S. Casuccio, T. L. Lersch, B. Artíñano (2009): Individual particle characteristics of North African dust under different long-range transport scenarios. *Atmos. Environ.* 43, 1850-1863.
- Cziczo, D. J., K. D. Froyd, S. J. Gallavardin, O. Möhler, S. Benz, H. Saathoff, D. M. Murphy (2009): Deactivation of ice nuclei due to atmospherically relevant surface coatings. *Environ. Res. Lett.* 4, 044013. doi: 10.1088/1748-9326/4/4/044013
- Dall'Osto, M., R. M. Harrison, E. J. Highwood, C. O'Dowd, D. Ceburnis, X. Querol, E. P. Achterberg (2010): Variation of the mixing state of Saharan dust particles with atmospheric transport. *Atmos. Environ.* 44(26), 3135-3146. doi: 10.1016/j.atmosenv.2010.05.030
- Davison, B., C. O'Dowd, C. N. Hewitt, M. H. Smith, R. M. Harrison, D. A. Peel, E. Wolf, R. Mulvaney, M. Schwikowski, U. Baltensperger (1996): Dimethyl sulfide and its oxidation products in the atmosphere of the Atlantic and Southern Oceans. *Atmos. Environ.* 30(10), 1895-1906. doi: 10.1016/1352-2310(95)00428-9
- Deboudt, K., P. Flament, M. Choël, A. Gloter, S. Sobanska, C. Colliex (2010): Mixing state of aerosols and direct observation of carbonaceous and marine coatings on African dust by individual particle analysis. *J. Geophys. Res.* 115, D24207. doi: 10.1029/2010JD013921
- Deer, W. A., R. A. Howie, J. Zussman (1992): *An Introduction to the Rock-Forming Minerals*. Second Edition. Harlow, UK, Pearson Education Ltd.

- Denjean, C., S. Caquineau, K. Desboeufs, B. Laurent, M. Maille, M. Quiñones Rosado, P. Vallejo, O. L. Mayol-Bracero, P. Formenti (2015): Long-range transport across the Atlantic in summertime does not enhance the hygroscopicity of African mineral dust. *Geophys. Res. Lett.* 42(18), 7835-7843. doi: 10.1002/2015gl065693
- Dlugi, R., S. Jordan, E. Lindemann (1981): The heterogeneous formation of sulfate aerosols in the atmosphere. *J. Aerosol Sci.* 12(3), 185-197. doi: 10.1016/0021-8502(81)90089-6
- Efron, B. (1979): Bootstrap Methods: Another Look at the Jackknife. *Ann. Statist.*(1), 1-26. doi: 10.1214/aos/1176344552
- Efron, B. (2003): Second Thoughts on the Bootstrap. *Statist. Sci.* 18(2), 135-140. doi: 10.1214/ss/1063994968
- Eglinton, T. I., G. Eglinton, L. Dupont, E. R. Sholkovitz, D. Montluçon, C. M. Reddy (2002): Composition, age, and provenance of organic matter in NW African dust over the Atlantic Ocean. *Geochem. Geophys. Geosy.* 3(8), 1-27. doi: 10.1029/2001gc000269
- Falkovich, A. H., E. Ganor, Z. Levin, P. Formenti, Y. Rudich (2001): Chemical and mineralogical analysis of individual mineral dust particles. *J. Geophys. Res.* 106(D16), 18029-18036.
- Fitzgerald, E., A. P. Ault, M. D. Zauscher, O. L. Mayol-Bracero, K. A. Prather (2015): Comparison of the mixing state of long-range transported Asian and African mineral dust. *Atmos. Environ.* 115, 19-25. doi: 10.1016/j.atmosenv.2015.04.031
- Fletcher, R. A., N. W. M. Ritchie, I. M. Anderson, J. A. Small (2011). *Microscopy and microanalysis of individual collected particles. Aerosol Measurement. Principles, Techniques, and Applications.* P. Kulkarni, P. A. Baron and K. Willeke. Hoboken, New Jersey, John Wiley & Sons.: 179-232.
- Garimella, S., Y. W. Huang, J. S. Seewald, D. J. Cziczo (2014): Cloud condensation nucleus activity comparison of dry- and wet-generated mineral dust aerosol: the significance of soluble material. *Atmos. Chem. Phys.* 14(12), 6003-6019. doi: 10.5194/acp-14-6003-2014
- Goldstein, J. I., D. E. Newbury, D. Joy, C. Lyman, P. Echlin, E. Lifshin, L. Sawyer, J. Michael (2003): *Scanning Electron Microscopy and X-Ray Microanalysis.* New York, Kluwer Academic / Plenum Publishers.
- Golovin, M. N., A. A. Putnam (1962): Inertial impaction on single elements. *Ind. Eng. Chem. Fundam.* 1(4), 264-273.
- Grini, A., G. Myhre, C. S. Zender, I. S. A. Isaksen (2005): Model simulations of dust sources and transport in the global atmosphere: Effects of soil erodibility and wind speed variability. *J. Geophys. Res.* 110, 10.1029/2004JD005037.
- Hangal, S., K. Willeke (1990): Overall efficiency of tubular inlets sampling at 0 - 90 degrees from horizontal aerosol flows. *Atmos. Environ.* 24A, 2379-2386. doi: 10.1016/0960-1686(90)90330-P
- Harrison, A. D., T. F. Whale, M. A. Carpenter, M. A. Holden, L. Neve, D. O'Sullivan, J. Vergara Temprado, B. J. Murray (2016): Not all feldspars are equal: a survey of ice nucleating properties across the feldspar group of minerals. *Atmos. Chem. Phys.* 16(17), 10927-10940. doi: 10.5194/acp-16-10927-2016
- Hartung, J., B. Elpelt, K.-H. Klösener (2005): *Statistik: Lehr- und Handbuch der angewandten Statistik.*, Oldenbourg, Munich, Germany.
- Iwata, A., A. Matsuki (2018): Characterization of individual ice residual particles by the single droplet freezing method: a case study in the Asian dust outflow region. *Atmos. Chem. Phys.* 18(3), 1785-1804. doi: 10.5194/acp-18-1785-2018
- Jaenicke, R., C. Junge (1967): Studien zur oberen Grenzgröße des natürlichen Aerosols. *Beitr. Phys. Atmos. / Contrib. Atmos. Phys.* 40, 129-143.
- Kandler, K., N. Benker, U. Bundke, E. Cuevas, M. Ebert, P. Knippertz, S. Rodríguez, L. Schütz, S. Weinbruch (2007): Chemical composition and complex refractive index of Saharan Mineral Dust at Izaña, Tenerife (Spain) derived by electron microscopy. *Atmos. Environ.* 41(37), 8058-8074. doi: 10.1016/j.atmosenv.2007.06.047
- Kandler, K., K. Lieke, N. Benker, C. Emmel, M. Küpper, D. Müller-Ebert, M. Ebert, D. Scheuvsens, A. Schladitz, L. Schütz, S. Weinbruch (2011a): Electron microscopy of particles collected at Praia,

- Cape Verde, during the Saharan Mineral dust experiment: particle chemistry, shape, mixing state and complex refractive index. *Tellus* 63B, 475-496. doi: 10.1111/j.1600-0889.2011.00550.x
- Kandler, K., L. Schütz, C. Deutscher, H. Hofmann, S. Jäckel, P. Knippertz, K. Lieke, A. Massling, A. Schladitz, B. Weinzierl, S. Zorn, M. Ebert, R. Jaenicke, A. Petzold, S. Weinbruch (2009): Size distribution, mass concentration, chemical and mineralogical composition, and derived optical parameters of the boundary layer aerosol at Tinfou, Morocco, during SAMUM 2006. *Tellus* 61B, 32-50. doi: 10.1111/j.1600-0889.2008.00385.x
- Kandler, K., L. Schütz, S. Jäckel, K. Lieke, C. Emmel, D. Müller-Ebert, M. Ebert, D. Scheuvs, A. Schladitz, B. Šegvić, A. Wiedensohler, S. Weinbruch (2011b): Ground-based off-line aerosol measurements at Praia, Cape Verde, during the Saharan Mineral Dust Experiment: Microphysical properties and mineralogy. *Tellus* 63B, 459-474. doi: 10.1111/j.1600-0889.2011.00546.x
- Karyampudi, V. M., S. P. Palm, J. A. Reagen, H. Fang, W. B. Grant, R. M. Hoff, C. Moulin, H. F. Pierce, O. Torres, E. Browell, S. H. Melfi (1999): Validation of the Saharan Dust Plume Conceptual Model Using Lidar, Meteosat, and ECMWF Data. *Bull. Am. Met. Soc.* 80(6), 1045-1075.
- Karydis, V. A., A. P. Tsimpidi, S. Bacer, A. Pozzer, A. Nenes, J. Lelieveld (2017): Global impact of mineral dust on cloud droplet number concentration. *Atmos. Chem. Phys.* 17(9), 5601-5621. doi: 10.5194/acp-17-5601-2017
- Kelly, J. T., C. C. Chuang, A. S. Wexler (2007): Influence of dust composition on cloud droplet formation. *Atmos. Environ.* 41, 2904-2916.
- Koehler, K. A., P. J. DeMott, S. M. Kreidenweis, O. B. Popovicheva, M. D. Petters, C. M. Carrico, E. D. Kireeva, T. D. Khokhlova, N. K. Shonija (2009): Cloud condensation nuclei and ice nucleation activity of hydrophobic and hydrophilic soot particles. *Phys. Chem. Chem. Phys.* 11, 7906-7920. doi: 10.1039/b905334b
- Kristensen, T. B., T. Müller, K. Kandler, N. Benker, M. Hartmann, J. M. Prospero, A. Wiedensohler, F. Stratmann (2016): Properties of cloud condensation nuclei (CCN) in the trade wind marine boundary layer of the western North Atlantic. *Atmos. Chem. Phys.* 16(4), 2675-2688. doi: 10.5194/acp-16-2675-2016
- Kumar, P., I. N. Sokolik, A. Nenes (2011): Measurements of cloud condensation nuclei activity and droplet activation kinetics of fresh unprocessed regional dust samples and minerals. *Atmos. Chem. Phys.* 11, 3527-3541. doi: 10.5194/acp-11-3527-2011
- Lack, D. A., P. K. Quinn, P. Massoli, T. S. Bates, D. Coffman, D. S. Covert, B. Sierau, S. Tucker, T. Baynard, E. Lovejoy, D. M. Murphy, A. R. Ravishankara (2009): Relative humidity dependence of light absorption by mineral dust after long-range atmospheric transport from the Sahara. *Geophys. Res. Lett.* 36(24). doi: 10.1029/2009GL041002
- Lai, A. C. K., W. W. Nazaroff (2005): Supermicron particle deposition from turbulent chamber flow onto smooth and rough vertical surfaces. *Atmos. Environ.* 39(27), 4893-4900. doi: 10.1016/j.atmosenv.2005.04.036
- Laskin, A., J. P. Cowin, M. J. Iedema (2006): Analysis of individual environmental particles using modern methods of electron microscopy and X-ray microanalysis. *J. Electron. Spectrosc. Relat. Phenom.* 150, 260-274. doi: 10.1016/j.elspec.2005.06.008
- Lepple, F. K., C. J. Brine (1976): Organic constituents in eolian dust and surface sediments from northwest Africa. *J. Geophys. Res.* 81(6), 1141-1147. doi: 10.1029/JC081i006p01141
- Lewis, E. R., S. E. Schwartz (2004): *Sea Salt Aerosol Production: Mechanisms, Methods, Measurements and Models*. Washington, DC, American Geophysical Union.
- Li-Jones, X., J. M. Prospero (1998): Variations in the size distribution of non-sea-salt sulfate aerosol in the marine boundary layer at Barbados: Impact of African dust. *J. Geophys. Res.* 103(D13), 16073-16084. doi: 10.1029/98jd00883
- Li, S.-N., D. A. Lundgren (2002): Aerosol Aspiration Efficiency of Blunt and Thin-Walled Samplers at Different Wind Orientations. *Aerosol Sci. Tech.* 36, 342-350.
- Li, W. J., L. Y. Shao (2009): Observation of nitrate coatings on atmospheric mineral dust particles. *Atmos. Chem. Phys.* 9(6), 1863-1871. doi: 10.5194/acp-9-1863-2009

- Liao, H., J. H. Seinfeld (1998): Radiative forcing by mineral dust aerosols: sensitivity to key variables. *J. Geophys. Res.* 103(D24), 31637-31645. doi: 10.1029/1998JD200036
- Mahowald, N., S. Albania, J. F. Kok, S. Engelstaeder, R. Scanza, D. S. Ward, M. G. Flanner (2014): The size distribution of desert dust aerosols and its impact on the Earth system. *Aeolian Res.* 15, 53-71. doi: 10.1016/j.aeolia.2013.09.002
- Matsuki, A., Y. Iwasaka, G.-Y. Shi, H.-B. Chen, K. Osada, D. Zhang, M. Kido, Y. Inomata, Y.-S. Kim, D. Trochkin (2005): Heterogeneous sulfate formation on dust surface and its dependence on mineralogy: balloon-borne observations from balloon-borne measurements in the surface atmosphere of Beijing, China. *Water Air Soil Pollut.* 5(3), 101-132. doi: 10.1007/s11267-005-0730-3
- May, K. R., R. Clifford (1967): The impaction of aerosol particles on cylinders, spheres, ribbons and discs. *Ann. Occup. Hyg.* 10, 83-95.
- McInnes, L. M., D. S. Covert, P. K. Quinn, M. S. Germani (1994): Measurements of chloride depletion and sulfur enrichment in individual sea-salt particles collected from the remote marine boundary layer. *J. Geophys. Res.* 99(D4), 8257-8268. doi: 10.1029/93jd03453
- Niimura, N., K. Okada, X.-B. Fan, K. Kai, K. Arai, G.-Y. Shi, S. Takahashi (1998): Formation of Asian Dust-Storm Particles Mixed Internally with Sea Salt in the Atmosphere. *J. Meteor. Soc. Japan* 76(2), 275-288.
- NOAA-ARL. (2017). "GDAS half-degree archive." 2016, from <ftp://arlftp.arlhq.noaa.gov/pub/archives/gdas0p5>, accessed 2016 and 2017.
- Noll, K. E. (1970): A rotary inertial impactor for sampling giant particles in the atmosphere. *Atmos. Environ.* 4, 9-19. doi: 10.1016/0004-6981(70)90050-8
- Noll, K. E., K. Y. P. Fang (1989): Development of a dry deposition model for atmospheric coarse particles. *Atmos. Environ.* 23(3), 585-594. doi: 10.1016/0004-6981(89)90007-3
- Noll, K. E., M. M. Jackson, A. K. Oskouie (2001): Development of an Atmospheric Particle Dry Deposition Model. *Aerosol Sci. Technol.* 35(2), 627-636. doi: 10.1080/02786820119835
- Noll, K. E., A. Pontius, R. Frey, M. Gould (1985): Comparison of atmospheric coarse particles at an urban and non-urban site. *Atmos. Environ.* 19(11), 1931-1943.
- Nowottnick, E., P. Colarco, A. da Silva, D. Hlavka, M. McGill (2011): The fate of saharan dust across the atlantic and implications for a central american dust barrier. *Atmos. Chem. Phys.* 11(16), 8415-8431. doi: 10.5194/acp-11-8415-2011
- Ott, D. K., W. Cyrs, T. M. Peters (2008a): Passive measurement of coarse particulate matter, PM<sub>10-2.5</sub>. *J. Aerosol Sci.* 39(2), 156-167. doi: 10.1016/j.jaerosci.2007.11.002
- Ott, D. K., T. Peters (2008b): A Shelter to Protect a Passive Sampler for Coarse Particulate Matter, PM<sub>10-2.5</sub>. *Aerosol Sci. Technol.* 42, 299-309. doi: 10.1080/02786820802054236
- Paik, S., J. H. Vincent (2002): Aspiration efficiency for thin-walled nozzles facing the wind and for very high velocity ratios. *J. Aerosol Sci.* 33(5), 705-720. doi: 10.1016/S0021-8502(01)00208-7
- Pattengale, N. D., M. Alipour, O. R. P. Bininda-Emonds, B. M. E. Moret, A. Stamatakis (2010): How Many Bootstrap Replicates Are Necessary? *J. Comput. Biol.* 17(3), 337-354. doi: 10.1089/cmb.2009.0179
- Petroff, A., L. Zhang (2010): Development and validation of a size-resolved particle dry deposition scheme for application in aerosol transport models. *Geosci. Model Dev.* 3(2), 753-769. doi: 10.5194/gmd-3-753-2010
- Pinsky, M., A. Khain, M. Shapiro (1999): Collisions of Small Drops in a Turbulent Flow. Part I: Collision Efficiency. Problem Formulation and Preliminary Results. *J. Atmos. Sci.* 56(15), 2585-2600. doi: 10.1175/1520-0469(1999)056<2585:cosdia>2.0.co;2
- Piskunov, V. N. (2009): Parameterization of aerosol dry deposition velocities onto smooth and rough surfaces. *J. Aerosol Sci.* 40(8), 664-679. doi: 10.1016/j.jaerosci.2009.04.006
- Prospero, J. M., R. Arimoto (2009). Atmospheric Transport and Deposition of Particulate Material to the Oceans A2 - Steele, John H. *Encyclopedia of Ocean Sciences (Second Edition)*. Oxford, Academic Press: 248-257.

- Prospero, J. M., F.-X. Collard, J. Molinié, A. Jeannot (2014): Characterizing the annual cycle of African dust transport to the Caribbean Basin and South America and its impact on the environment and air quality. *Global Biogeochem. Cy.* 28(7), 2013GB004802. doi: 10.1002/2013gb004802
- Rasband, W. S. (2015). "ImageJ." 1.47c. 2015.
- Reid, E. A., J. S. Reid, M. M. Meier, M. R. Dunlap, S. S. Cliff, A. Broumas, K. Perry, H. Maring (2003): Characterization of African dust transported to Puerto Rico by individual particle and size segregated bulk analysis. *J. Geophys. Res.* 108(D19), 8591. doi: 10.1029/2002JD002935
- Ro, C.-U., J. Osán, I. Szalóki, J. de Hoog, A. Worobiec, R. Van Grieken (2003): A Monte Carlo Program for Quantitative Electron-Induced X-ray Analysis of Individual Particles. *Anal. Chem.* 75, 851-859.
- Salter, M. E., E. Hamacher-Barth, C. Leck, J. Werner, C. M. Johnson, I. Riipinen, E. D. Nilsson, P. Zieger (2016): Calcium enrichment in sea spray aerosol particles. *Geophysical Research Letters* 43(15), 8277-8285. doi: 10.1002/2016gl070275
- Savoie, D. L., J. M. Prospero, S. J. Oltmans, W. C. Graustein, K. K. Turekian, J. T. Merrill, H. Levy (1992): Sources of nitrate and ozone in the marine boundary layer of the tropical north Atlantic. *J. Geophys. Res.* 97(D11), 11575-11589. doi: 10.1029/92jd00894
- Schladitz, A., T. Müller, A. Nowak, K. Kandler, K. Lieke, A. Massling, A. Wiedensohler (2011): In situ aerosol characterization at Cape Verde Part 1: Particle number size distributions, hygroscopic growth and state of mixing of the marine and Saharan dust aerosol. *Tellus* 63B, 531-548. doi: 10.1111/j.1600-0889.2011.00569.x
- Schütz, L. (1980): Long range transport of desert dust with special emphasis on the Sahara. *Ann. NY Acad. Sci.* 338(1), 515-532. doi: 10.1111/j.1749-6632.1980.tb17144.x
- Sehmel, G. A. (1973). *Particle Deposition and Diffusivities Along Smooth Surfaces*. Pollution. E. S. Barrekette, Springer. 2: 564-571.
- Shi, Z., M. D. Krom, S. Bonneville, A. R. Baker, C. Bristow, N. Drake, G. Mann, K. Carslaw, J. B. McQuaid, T. Jickells, L. G. Benning (2011a): Influence of chemical weathering and aging of iron oxides on the potential iron solubility of Saharan dust during simulated atmospheric processing. *Global Biogeochem. Cy.* 25, GB2010. doi: 10.1029/2010GB003837
- Shi, Z., M. D. Krom, S. Bonneville, A. R. Baker, T. D. Jickells, L. G. Benning (2009): Formation of Iron Nanoparticles and Increase in Iron Reactivity in Mineral Dust during Simulated Cloud Processing. *Environ. Sci. Tech.* 43, 6592-6596. doi: 10.1021/es901294g
- Shi, Z., M. D. Krom, T. D. Jickells, S. Bonneville, K. S. Carslaw, N. Mihalopoulos, A. R. Baker, L. G. Benning (2012): Impacts on iron solubility in the mineral dust by processes in the source region and the atmosphere: A review. *Aeolian Res.* 5, 21-42. doi: 10.1016/j.aeolia.2012.03.001
- Shi, Z. B., M. T. Woodhouse, K. S. Carslaw, M. D. Krom, G. W. Mann, A. R. Baker, I. Savov, G. R. Fones, B. Brooks, N. Drake, T. D. Jickells, L. G. Benning (2011b): Minor effect of physical size sorting on iron solubility of transported mineral dust. *Atmos. Chem. Phys.* 11(16), 8459-8469. doi: 10.5194/acp-11-8459-2011
- Sholkovitz, E. R., P. N. Sedwick, T. M. Church, A. R. Baker, C. F. Powell (2012): Fractional solubility of aerosol iron: Synthesis of a global-scale data set. *Geochim. Cosmochim. Acta* 89, 173-189. doi: 10.1016/j.gca.2012.04.022
- Slinn, S. A., W. G. N. Slinn (1980): Predictions for particles deposition on natural waters. *Atmos. Environ.* 14, 1013-1016. doi: 10.1016/0004-6981(80)90032-3
- Stein, A. F., R. R. Draxler, G. D. Rolph, B. J. B. Stunder, M. D. Cohen, F. Ngan (2015): NOAA's HYSPLIT Atmospheric Transport and Dispersion Modeling System. *Bull. Am. Met. Soc.* 96(12), 2059-2077. doi: 10.1175/bams-d-14-00110.1
- Stevens, B., D. Farrell, L. Hirsch, F. Jansen, L. Nuijens, I. Serikov, B. Brüggemann, M. Forde, H. Linne, K. Lonitz, J. M. Prospero (2016): The Barbados Cloud Observatory: Anchoring Investigations of Clouds and Circulation on the Edge of the ITCZ. *Bull. Am. Met. Soc.* 97(5), 787-801. doi: 10.1175/bams-d-14-00247.1

- Sullivan, R. C., S. A. Guazzotti, D. A. Sodeman, K. A. Prather (2007a): Direct observations of the atmospheric processing of Asian mineral dust. *Atmos. Chem. Phys.* 7, 1213-1236. doi: 10.5194/acp-7-1213-2007
- Sullivan, R. C., S. A. Guazzotti, D. A. Sodeman, Y. Tang, G. R. Carmichael, K. A. Prather (2007b): Mineral dust is a sink for chlorine in the marine boundary layer. *Atmos. Environ.* 41, 7166-7179. doi: 10.1016/j.atmosenv.2007.05.047
- Sundaram, S., L. R. Collins (1997): Collision statistics in an isotropic particle-laden turbulent suspension. Part 1. Direct numerical simulations. *J. Fluid Mech.* 335, 75-109. doi: 10.1017/s0022112096004454
- Tang, M., D. J. Cziczo, V. H. Grassian (2016): Interactions of Water with Mineral Dust Aerosol: Water Adsorption, Hygroscopicity, Cloud Condensation, and Ice Nucleation. *Chem. Rev.* 116(7), 4205-4259. doi: 10.1021/acs.chemrev.5b00529
- Trapp, J. M., F. J. Millero, J. M. Prospero (2010): Temporal variability of the elemental composition of African dust measured in trade wind aerosols at Barbados and Miami. *Mar. Chem.* 120, 71-82. doi: 10.1016/j.marchem.2008.10.004
- Trincavelli, J., S. Limandri, R. Bonetto (2014): Standardless quantification methods in electron probe microanalysis. *Spectrochim. Acta B* 101, 76-85. doi: 10.1016/j.sab.2014.07.016
- Ullerstam, M., R. Vogt, S. Langer, E. Ljungström (2002): The kinetics and mechanism of SO<sub>2</sub> oxidation by O<sub>3</sub> on mineral dust. *Phys. Chem. Chem. Phys.* 4, 4694-4699. doi: 10.1039/B203529B
- Usher, C. R., H. Al-Hosney, S. Carlos-Cuellar, V. H. Grassian (2002): A laboratory study of the heterogeneous uptake and oxidation of sulfur dioxide on mineral dust particles. *J. Geophys. Res.* 107(D23), 4713. doi: 10.1029/2002JD002051
- van der Does, M., L. F. Korte, C. I. Munday, G. J. A. Brummer, J. B. W. Stuut (2016): Particle size traces modern Saharan dust transport and deposition across the equatorial North Atlantic. *Atmos. Chem. Phys.* 16(21), 13697-13710. doi: 10.5194/acp-16-13697-2016
- Wagner, J., D. Leith (2001): Passive Aerosol Sampler. Part I: Principle of Operation. *Aerosol Sci. Technol.* 34(186-192). doi: 10.1080/027868201300034808
- Wang, L.-P., O. Ayala, S. E. Kasprzak, W. W. Grabowski (2005): Theoretical Formulation of Collision Rate and Collision Efficiency of Hydrodynamically Interacting Cloud Droplets in Turbulent Atmosphere. *J. Atmos. Sci.* 62(7), 2433-2450. doi: 10.1175/jas3492.1
- Warneck, P., J. Williams (2012): *The Atmospheric Chemist's Companion. Numerical Data for Use in the Atmospheric Sciences*, Springer Netherlands.
- Weinbruch, S., M. Wentzel, M. Kluckner, P. Hoffmann, H. M. Ortner (1997): Characterization of Individual Atmospheric Particles by Element Mapping in Electron Probe Microanalysis. *Mikrochim. Acta* 125, 137-141. doi: 10.1007/BF01246176
- Weinzierl, B., A. Ansmann, J. M. Prospero, D. Althausen, N. Benker, F. Chouza, M. Dollner, D. Farrell, W. K. Fomba, V. Freudenthaler, J. Gasteiger, S. Groß, M. Haarig, B. Heinold, K. Kandler, T. B. Kristensen, O. L. Mayol-Bracero, T. Müller, O. Reitebuch, D. Sauer, A. Schäfler, K. Schepanski, A. Spanu, I. Tegen, C. Toledano, A. Walser (2017): The Saharan Aerosol Long-Range Transport and Aerosol-Cloud-Interaction Experiment: Overview and Selected Highlights. *Bulletin of the American Meteorological Society* 98(7), 1427-1451. doi: 10.1175/bams-d-15-00142.1
- Weinzierl, B., D. Sauer, M. Esselborn, A. Petzold, A. Veira, M. Rose, S. Mund, M. Wirth, A. Ansmann, M. Tesche, S. Gross, V. Freudenthaler (2011): Microphysical and optical properties of dust and tropical biomass burning aerosol layers in the Cape Verde region—an overview of the airborne in situ and lidar measurements during SAMUM-2. *Tellus B* 63(4), 589-618. doi: 10.1111/j.1600-0889.2011.00566.x
- Wen, X., D. B. Ingham (2000): Aspiration efficiency of a thin-walled cylindrical aerosol sampler at yaw orientations with respect to the wind. *J. Aerosol Sci.* 31(11), 1355-1365. doi: 10.1016/S0021-8502(00)00036-7
- Wurzler, S., T. G. Reisin, Z. Levin (2000): Modification of mineral dust particles by cloud processing and subsequent effects on drop size distributions. *J. Geophys. Res.* 105(D4), 4501-4512. doi: 10.1029/1999JD900980

- Xu, X., U. S. Akhtar (2010): Identification of potential regional sources of atmospheric total gaseous mercury in Windsor, Ontario, Canada using hybrid receptor modeling. *Atmos. Chem. Phys.* 10(15), 7073-7083. doi: 10.5194/acp-10-7073-2010
- Zamora, L. M., J. M. Prospero, D. A. Hansell (2011): Organic nitrogen in aerosols and precipitation at Barbados and Miami: Implications regarding sources, transport and deposition to the western subtropical North Atlantic. *J. Geophys. Res.* 116(D20). doi: doi:10.1029/2011JD015660
- Zhang, D. (2008): Effect of sea salt on dust settling to the ocean. *Tellus* 60B, 641-646. doi: 10.1111/j.1600-0889.2008.00358.x
- Zhang, D., Y. Iwasaka (1999): Nitrate and sulfate in individual Asian dust-storm particles in Beijing, China in spring of 1995 and 1996. *Atmos. Environ.* 33, 3213-3223. doi: 10.1016/S1352-2310(99)00116-8
- Zhang, D., Y. Iwasaka (2004): Size change of Asian dust particles caused by sea salt interaction: Measurements in southwestern Japan. *Geophys. Res. Lett.* 31, L15102. doi: 10.1029/2004GL020087
- Zobrist, B., C. Marcolli, T. Peter, T. Koop (2008): Heterogeneous Ice Nucleation in Aqueous Solutions: the Role of Water Activity. *J. Phys. Chem. A* 112(17), 3965-3975. doi: 10.1021/jp7112208

**Table 1: Average dust mass concentrations estimated from deposited particle mass applying various deposition models. Lower and upper refer to different dust fraction estimates (see section 2.3.3).**

<b>Model</b>	<b>lower estimate, <math>\mu\text{g}/\text{m}^3</math></b>	<b>upper estimate, <math>\mu\text{g}/\text{m}^3</math></b>
Stokes settling	149	195
Noll et al. (2001)	0.28	0.32
Noll et al. (1989)	67	96
Aluko et al. (2006)	58	85
Piskunov (2009)	32	47
Wagner et al. (2001)	81	115
High-volume sampler		26

Fig. 1: Comparison of element weight ratios for albite and sodium chloride powder as function of particle size. The nominal ratios for the compounds are shown as orange lines. Left and center: albite ratios as function of acceleration voltage with ZAF correction. Right: sodium chloride ratio at 20 kV acceleration voltage, corrected by the methods Cliff-Lorrimer, ZAF and interpolated. The linear regression of the interpolated correction is shown as black striped line.

Fig. 2: Calculated ion balance for all beam interaction volumes containing particles dominated by Na and Cl. Particles were collected by the DPDS. The axes are scaled in arbitrary units of percent  $\times$  unit charges. Smaller particles yield smaller values as they only fill a fraction of the beam interaction volume. Particle size is color-coded; note that all particles between 0.6  $\mu\text{m}$  and 1  $\mu\text{m}$  in size are shown as blue, and between 10  $\mu\text{m}$  and 25  $\mu\text{m}$  as red. The black diagonal lines show the 10 % deviation cone.

Fig. 3: Mean element index only using Na, Mg, S, Cl, and Ca for normalization, and according standard deviation ( $1\sigma$ ) for NaCl-dominated particles from a typical atmospheric sample as function of particle size. Note that relative standard deviation for Ca is not shown due to frequent values below the detection limit.

Fig. 4: Deposition velocity to a smooth surface calculated by different deposition models for the samples of 2013, taking into account the ambient thermodynamic conditions and the particle composition. a: Stokes settling; b: Noll et al. (2001); c: Noll et al. (1989); d: Aluko et al. (2006); e: Piskunov (2009); f: Wagner et al. (2001)

Fig. 5: Number (a, c) and volume size distributions (b, d) of deposition rates as function of projected area diameter, modeled for Cape Verde aerosol as derived from a 5 mm  $\times$  5 mm analysis field. (a) and (b) are based on CV-ground, (c) and (d) on CV-air size distributions. The grey curve shows the original size distribution of deposited particles, the colored points with whiskers give median and central 95 % quantile of 1000 repetitions (200 for 0.093 and 0.172/0.173) for distributions calculated from samples with different area fractions covered by particles.

Fig. 6: Number (a, c, e) and volume size distributions (b, d, f) of deposited particles measured at Ragged Point and extrapolated change as function of particle projected area diameter and area coverage fraction, simulating a longer exposure time. Plots are given for low (a, b), medium (c, d) and high (e, f) base coverages. Different colors show different factors of exposure increase (5x, 10x, 15x, 20x). Resulting coverage fractions are given in the figure keys.

Fig. 7: Particle volume per area calculated from single particle measurements as function of the fractional area coverage. Blue symbols denote the unmodified samples, red symbols the simulation of higher coverage by factors of 2, 3, 5, 10, 15, and 20. Error bars denote the two-sided 95 % confidence interval. The fit function shown as black dashed line is calculated as  $y = \exp(a \ln(x) + b)$ ;  $[y] = \text{mm}^3/\text{m}^2$ ;  $a = 0.957 \pm 0.041$ ;  $b = 3.57 \pm 0.06$ ;  $x$  is the fractional area coverage.

Fig. 8: Upper 95 % quantile of the fractions of internally mixed particles due to coincidental mixing on the substrate (color scale), for a dust/sea-salt/sulfate system with measured composition and CV-ground size distribution. Strong mixture refers to a minimum particle volume fraction of the other component of 20 %, detectable mixture refers to 1 %. Mixing compounds are given on top of each graph. Sulfate/sea-salt and ternary mixtures practically do not form coincidentally.

Fig. 9: Average atmospheric mass size distribution densities derived from DPDS and FWI measurements. Left: period from July 10 to 15, 2013; right: from June 14 to July 8, 2013. Different colors refer to different deposition velocity estimates as shown in Fig. 4. Solid lines refer to total mass concentrations, dashed ones to the dust mass estimated from the chemical composition (upper limit estimate). Error bars show the central 95 % confidence interval. Pink crosses show a size distribution measured in the Saharan air layer on June 22, 2013 (Weinzierl et al. 2017). Note that for particles smaller than 10  $\mu\text{m}$  the FWI data may contain a considerable bias in calculation.

Fig. 10: Dust mass concentration and flux density time series derived from DPDS compared to such obtained from high-volume sampler (Kristensen et al. 2016). The darker brown bar shows the range from lower to upper estimate, the blue triangles the lower and upper estimate of dust deposition flux density. The date refers to the year 2013.

Fig. 11: Size dependence of the relative number abundance of major particle types as derived from single particle analysis of deposited aerosol.

Fig. 12: Left: box plot of daily mass deposition rate for total dust and dust-derived elements at Barbados for 2013 and 2016. Right: cumulative mass deposition flux as function of aerodynamic particle diameter for dust and dust-derived elements. Note that for P and Ti in the latter plot two particles containing each more than 10 % of the total deposited mass have been removed from the data set.

Fig. 13: Number ratio of total feldspar (filled symbols) and K-feldspar (open symbols) to total silicate particles as function of particle aerodynamic diameter in dry deposition collected at Barbados. For comparison, data from Tenerife (Kandler et al. 2007) and Morocco (Kandler et al. 2009) are given. Only data points with less than 30 % relative counting error are shown.

**Fig. 14: Potential source contribution functions (PSCF) of deposited material: dust (a, b), geometric silicate iron availability index SIAI (c, d), total soluble sulfate (e, f) and relative ion balance for sulfate particles (g, h) for 2013 and 2016 at Ragged Point. Note that for a-d, potential provenance is calculated for Saharan Air Layer transport only (i.e. trajectory arrival altitudes > 1500 m).**

**Fig. 15: Ca/Na atomic ratio as function of particle dry diameter for all sea-salt particles collected at Ragged Point in 2013. Different samplers are shown by color: CI blue, DPDS red, and FWI brown**

**Fig. 16: Time-series of wind and particle number deposition rates for pure compounds and internally mixed particles for June/July 2013 and August 2016. Particle size ranges are given in the top left of each graph. The limit of detection for the number of internally mixed particles is shown as line in the according color. Where only the detection limit for silicate/sulfate mixtures is visible, both limits are identical.**

**Fig. 17: Deposition velocities calculated with the Piskunov model for internal admixture of sea-salt (left) or sulfate (right) for the mixed particles observed at Ragged Point. Velocities are given for the unmixed dust core and internal mixtures at dry conditions, at ambient relative humidity, and at 90 % relative humidity. The lines show the according means. Note that variation in deposition velocity for the same dust core size arises from variation in wind speed and admixed fraction.**

**Fig. 18: Effective deposition velocity for all dust-containing particles observed at Ragged Point. The blue curves take into account internal mixing and hygroscopic growth at ambient conditions, whereas the orange only regards the dry dust fraction of the particles. In addition, cumulative mass distribution is shown on the inverted right axis. Particle size is given as aerodynamic diameter for the dust fraction of a particle. For the ambient deposition velocity, the geometric mean for each size class is shown in conjunction with the 1 geometric standard deviation range.**

Fig. 01

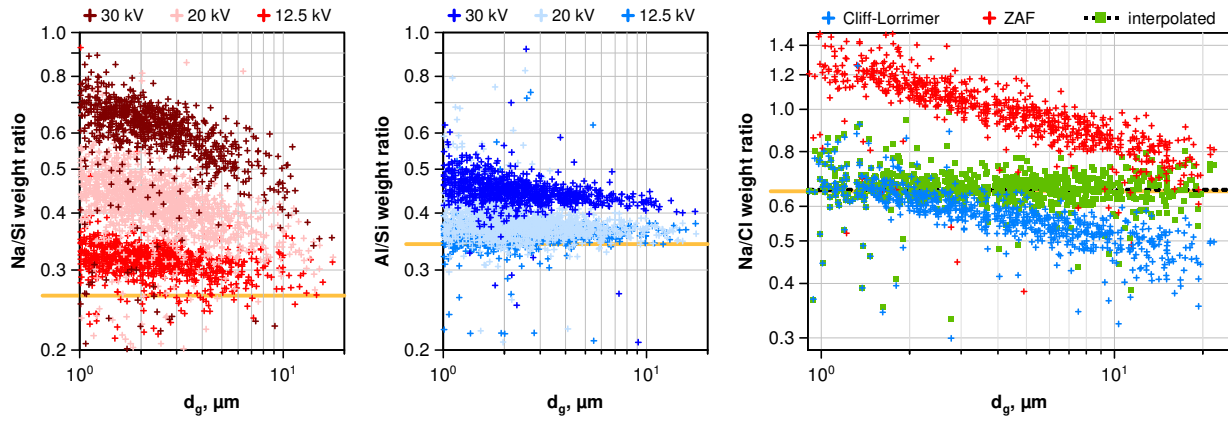


Fig. 02

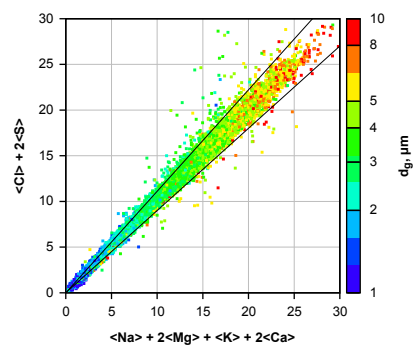


Fig. 03

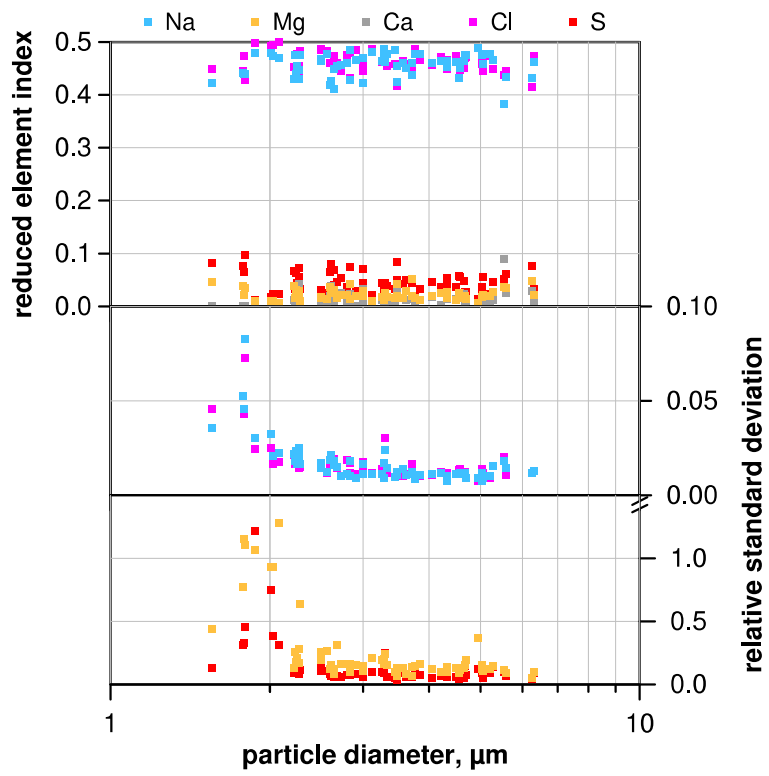


Fig. 04

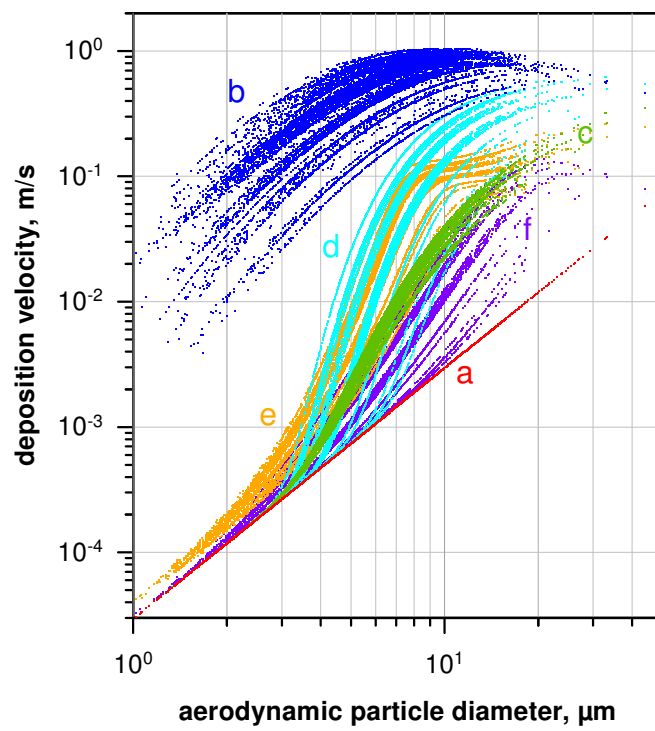


Fig. 05

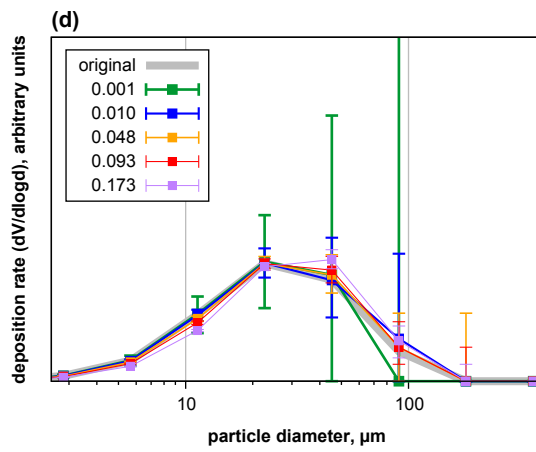
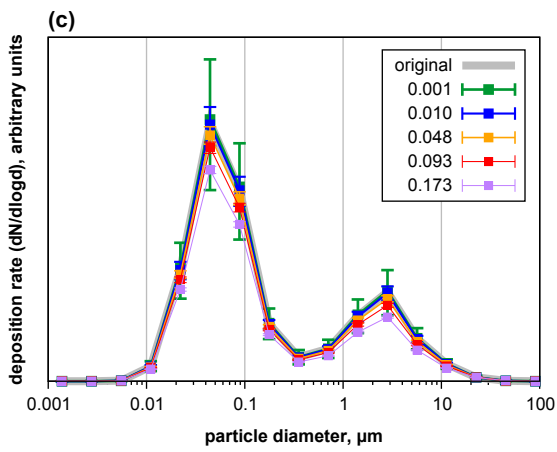
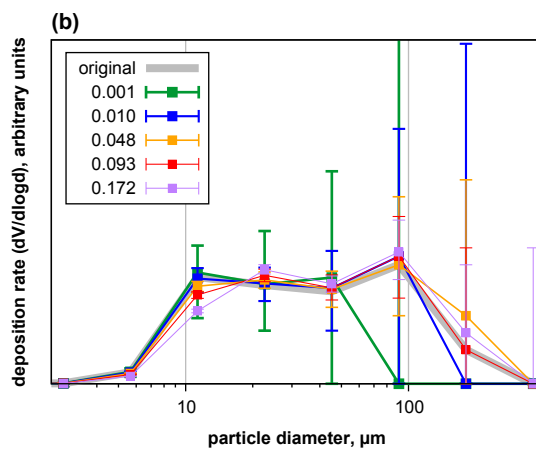
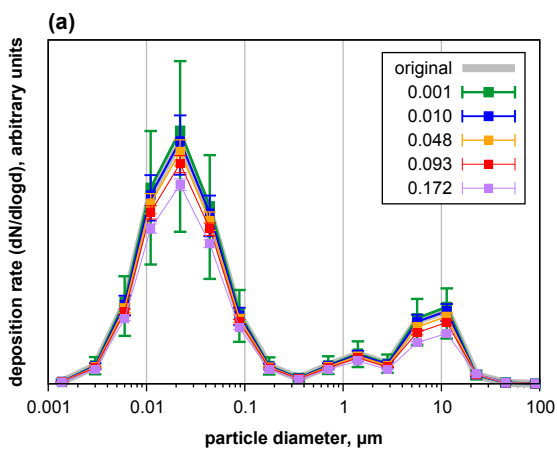


Fig. 06

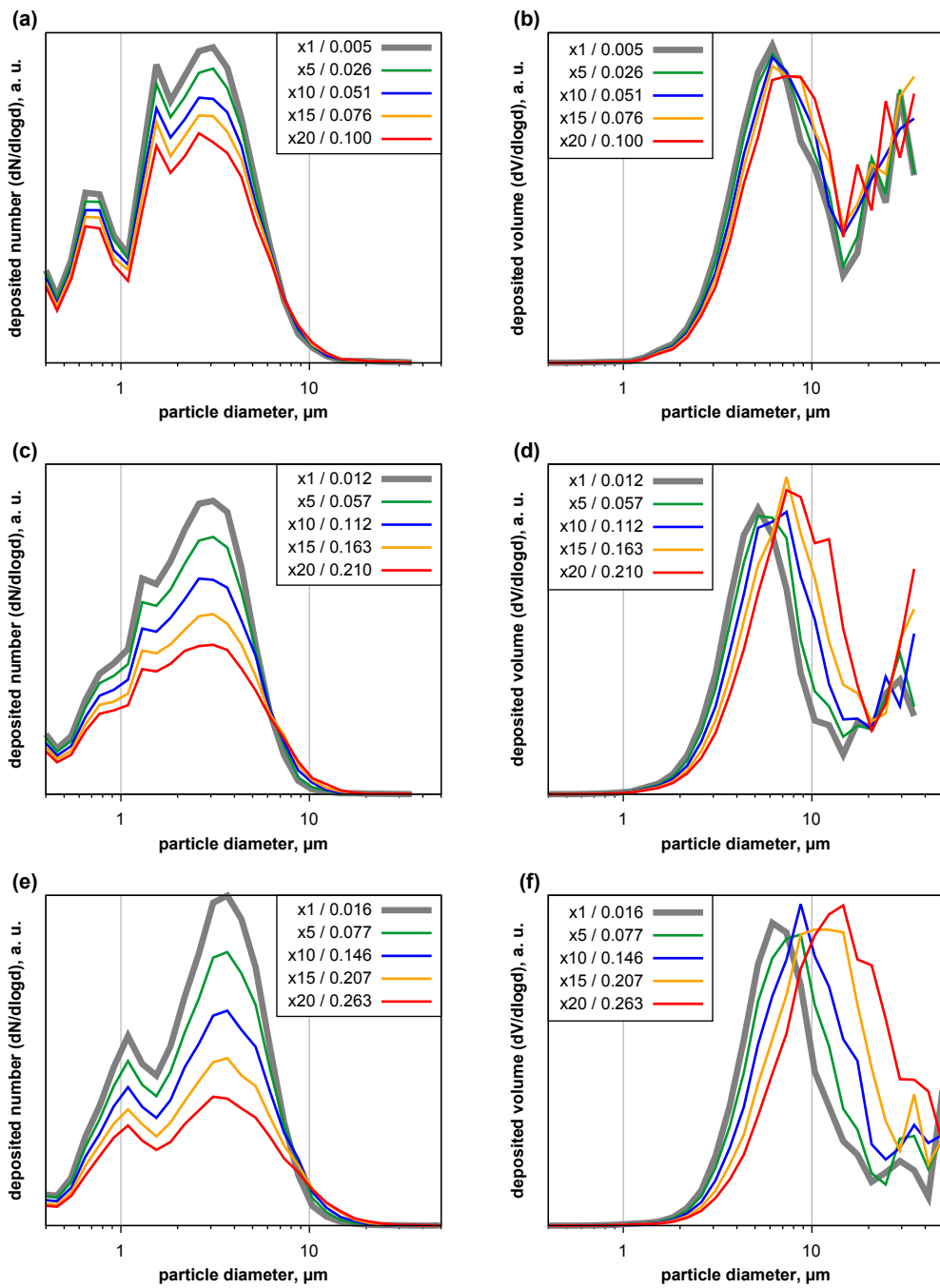


Fig. 07

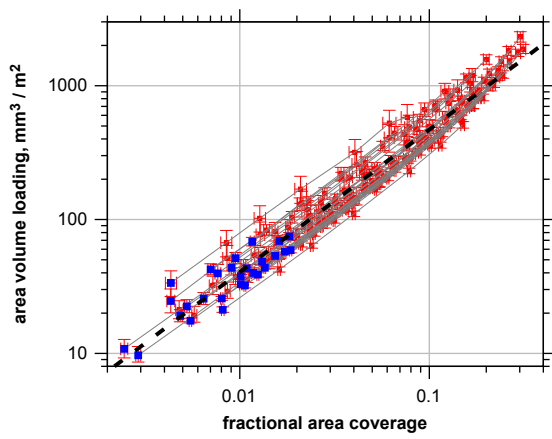
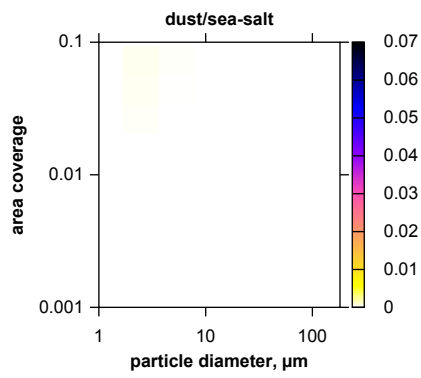
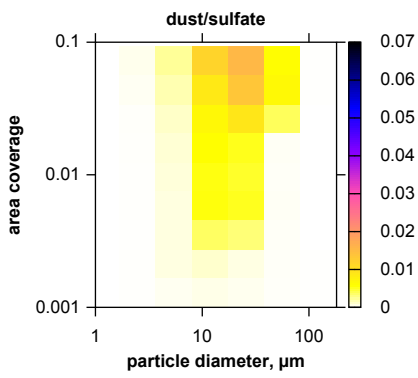


Fig. 08

*Strong mixture*



*Detectable mixture*

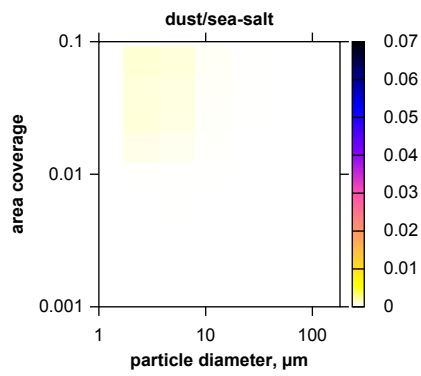
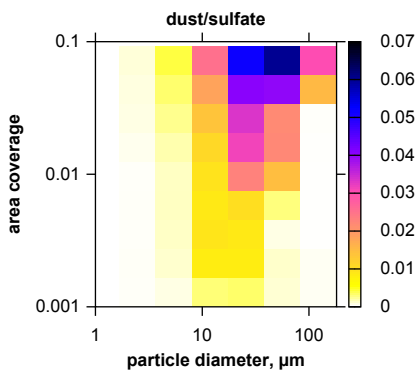


Fig. 09

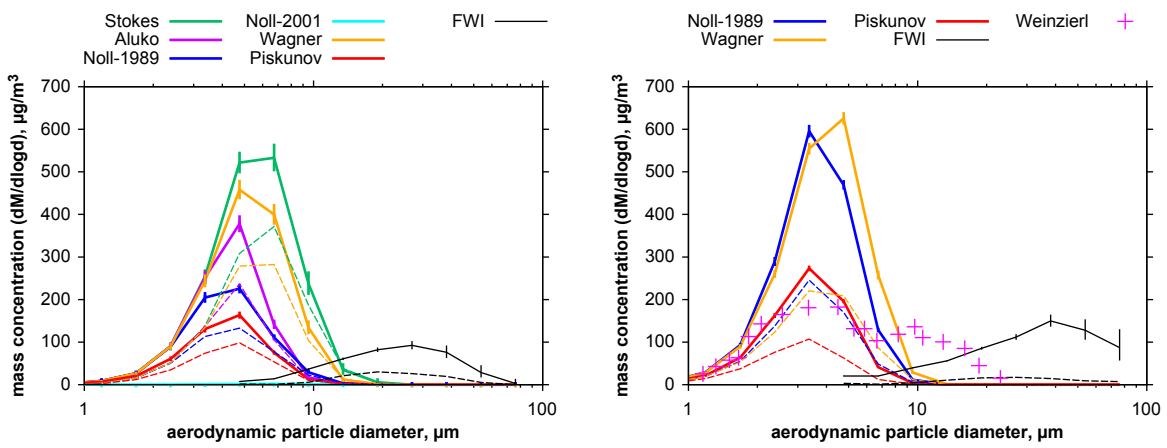


Fig. 10

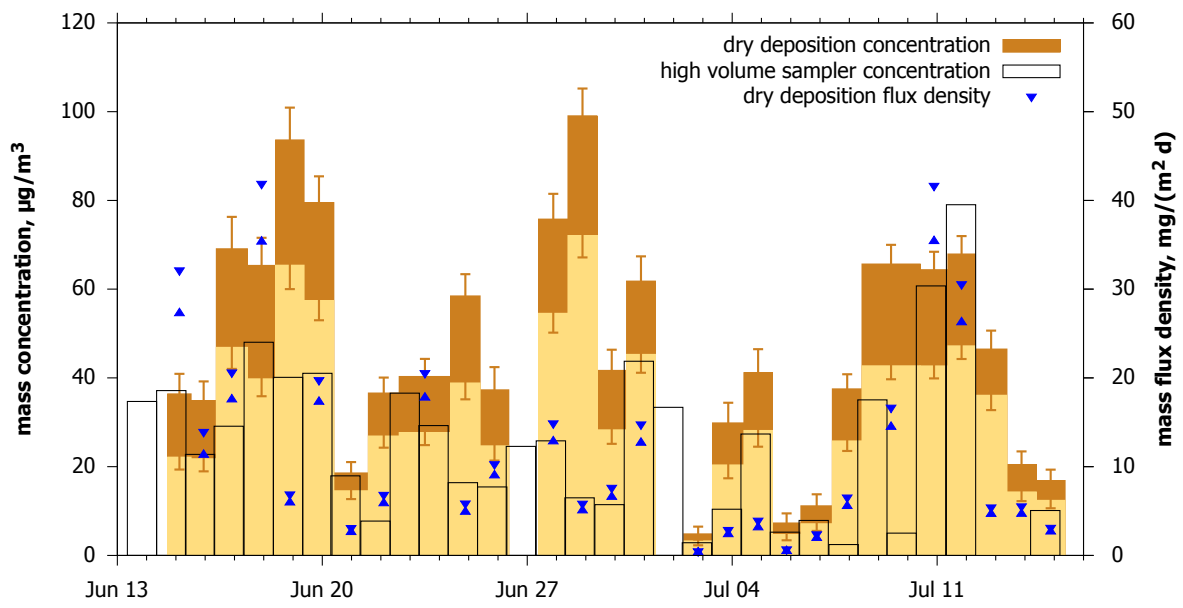




Fig. 12

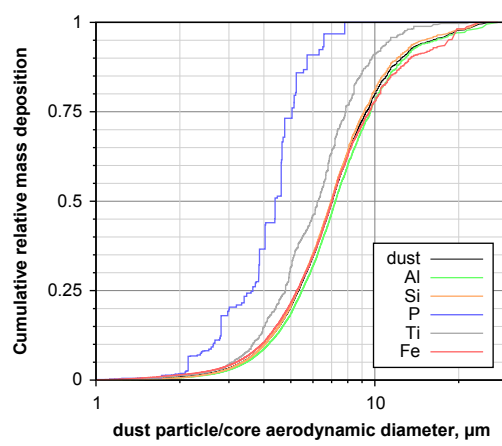
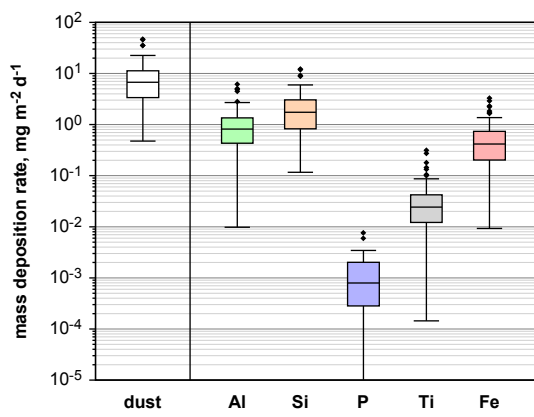


Fig. 13

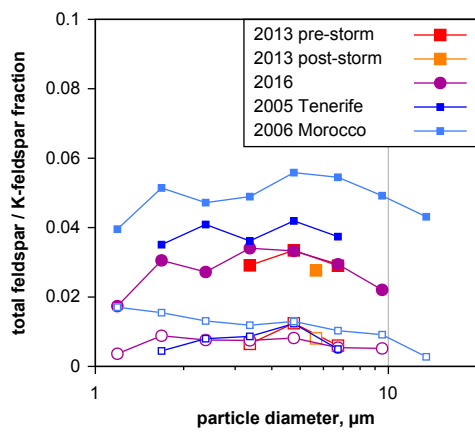
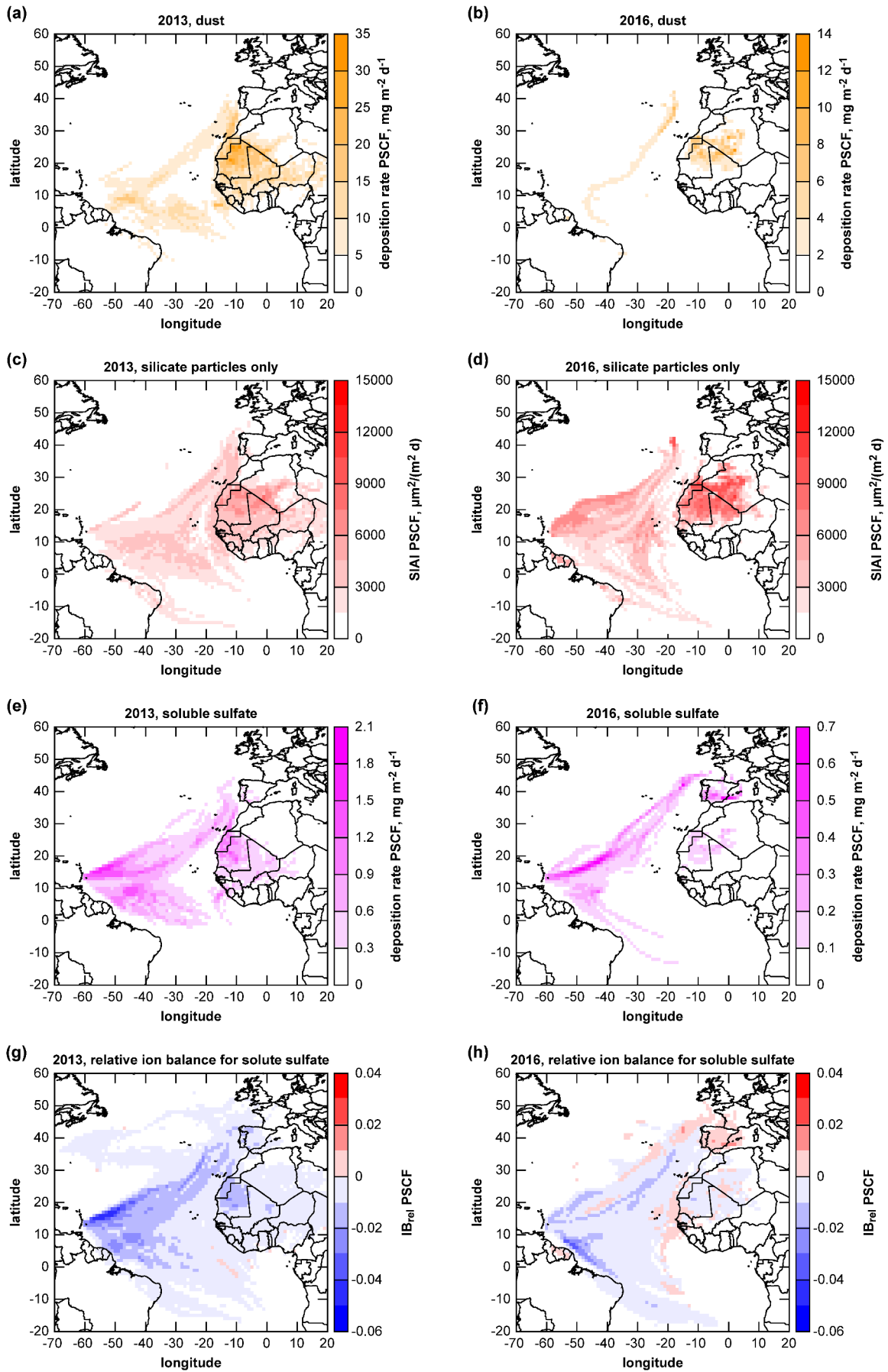


Fig. 14



**Fig. 15**

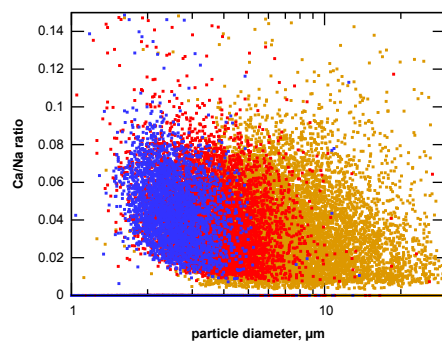


Fig. 16

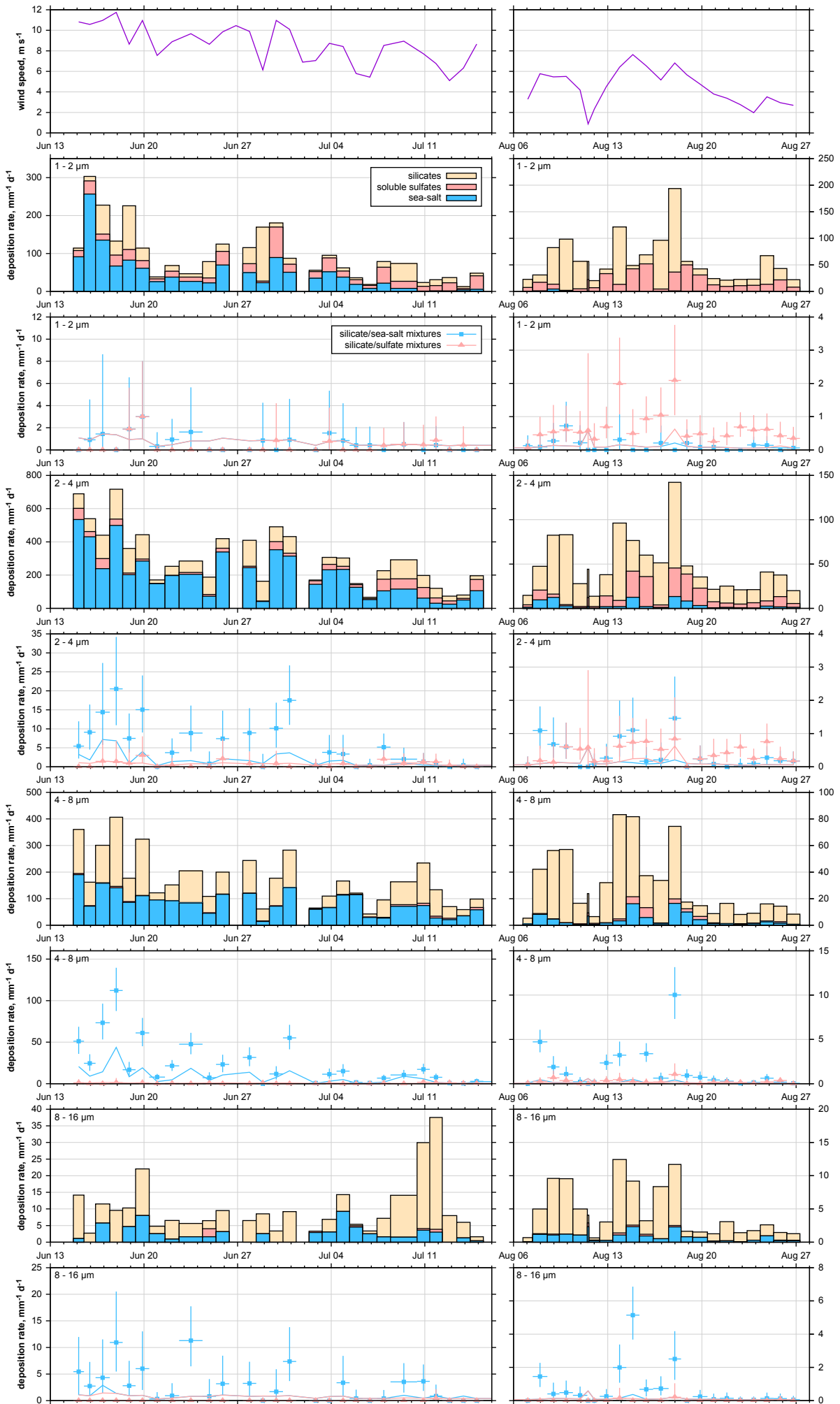


Fig. 17

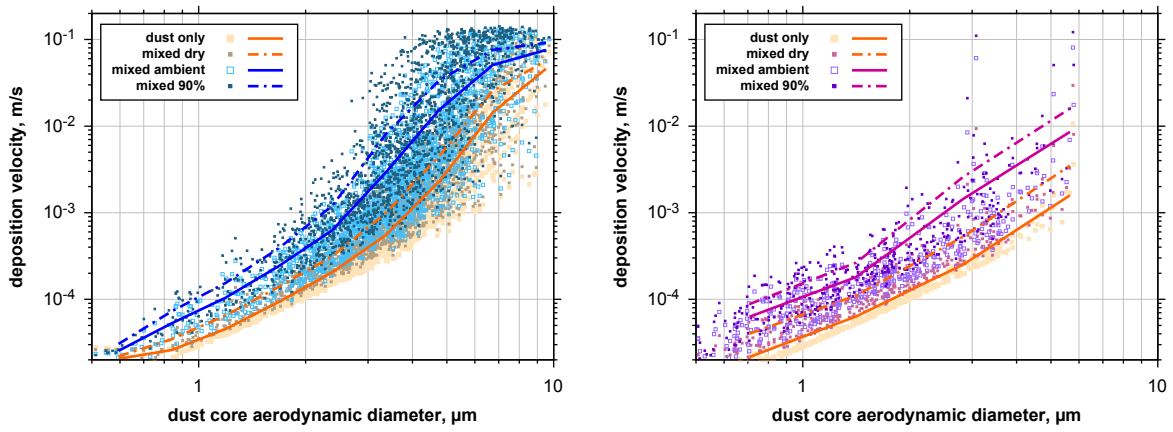
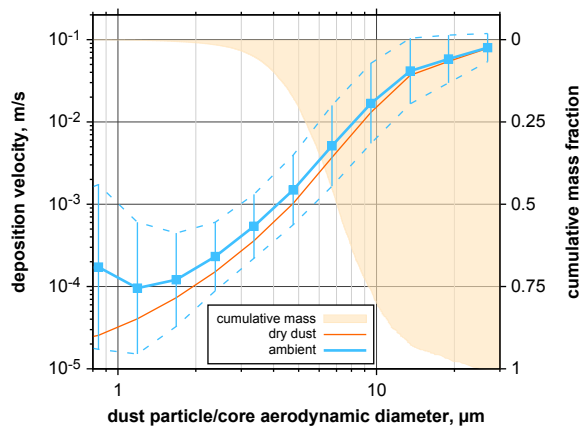


Fig. 18



# Electronic Supplement to “Composition and mixing state of atmospheric aerosols determined by electron microscopy: method development and application to aged Saharan dust deposition in the Caribbean boundary layer”

Konrad Kandler<sup>1,\*</sup>, Kilian Schneiders<sup>1</sup>, Martin Ebert<sup>1</sup>, Markus Hartmann<sup>1,+</sup>, Stephan Weinbruch<sup>1</sup>, Maria Prass<sup>2</sup>, Christopher Pöhlker<sup>2</sup>

<sup>1</sup>Institute for Applied Geosciences, Technical University Darmstadt, 64287 Darmstadt, Germany

<sup>2</sup>Max Planck Institute for Chemistry, Multiphase Chemistry Department, 55128 Mainz, Germany

<sup>+</sup>now at: Experimental Aerosol and Cloud Microphysics Department, Tropos Leibniz-Institute für Tropospheric Research (TROPOS), 04318 Leipzig, Germany

\*Correspondence to: K. Kandler ([kandler@geo.tu-darmstadt.de](mailto:kandler@geo.tu-darmstadt.de))

## S.1 Calculation of the feldspar indices

The index value showing the closeness of a particle composition to pure feldspar is based on three values, the overall contribution of feldspar-specific elements to the particle composition and the vicinities to the feldspar Al/Si ratio as well as to the K/Si or alkali/Si ratio. The overall contribution of specific elements is calculated as

$$r_{Sil} = \frac{\langle Na \rangle + \langle Al \rangle + \langle Si \rangle + \langle K \rangle + \langle Ca \rangle}{\langle Na \rangle + \langle Al \rangle + \langle Si \rangle + \langle K \rangle + \langle Ca \rangle + \langle Mg \rangle + \langle P \rangle + \langle S \rangle + \langle Cl \rangle + \langle Ti \rangle + \langle Fe \rangle} \quad (1)$$

The vicinity with respect to Al/Si is determined as:

$$r_{fsp,Al/Si} = \frac{\langle Al \rangle}{\langle Si \rangle} \frac{3\langle Na \rangle + 3\langle K \rangle + 2\langle Ca \rangle}{\langle Na \rangle + \langle K \rangle + 2\langle Ca \rangle} \quad (2)$$

$$Q_{fsp,Al/Si} = \begin{cases} 1 - \lg(r_{fsp,Al/Si}) & 0.1 \leq r_{fsp,Al/Si} \leq 10 \\ 0 & r_{fsp,Al/Si} < 0.1 \quad \vee \quad r_{fsp,Al/Si} > 10 \end{cases} \quad (3)$$

Closeness with respect to the K and alkali ratio is calculated as:

$$r_{fsp,K/Si} = \frac{3\langle K \rangle}{\langle Si \rangle} \quad (4)$$

$$Q_{fsp,K/Si} = \begin{cases} 1 - \lg(r_{fsp,K/Si}) & 0.1 \leq r_{fsp,K/Si} \leq 10 \\ 0 & r_{fsp,K/Si} < 0.1 \quad \vee \quad r_{fsp,K/Si} > 10 \end{cases} \quad (5)$$

$$r_{fsp,NaKCa/Si} = \frac{3\langle Na \rangle + 3\langle K \rangle + 2\langle Ca \rangle}{\langle Si \rangle} \quad (6)$$

$$Q_{fsp,NaKCa/Si} = \begin{cases} 1 - \lg(r_{fsp,NaKCa/Si}) & 0.1 \leq r_{fsp,NaKCa/Si} \leq 10 \\ 0 & r_{fsp,NaKCa/Si} < 0.1 \quad \vee \quad r_{fsp,NaKCa/Si} > 10 \end{cases} \quad (7)$$

The vicinity of a particle's composition to pure feldspar is expressed then as

$$P_{fsp} = r_{Sil} Q_{fsp,Al/Si} Q_{fsp,NaKCa/Si} \quad (8)$$

and to pure K feldspar as

$$P_{fsp,K} = r_{Sil} Q_{fsp,Al/Si} Q_{fsp,K/Si} \quad (9)$$

For example, the  $P_{fsp}$  value becomes 1 for pure albite and 0 for sodium chloride or quartz.

## S.2 Estimation of the dust contribution to each single particle in a dust / sea-salt / sulfate mixture and the size of the according dust inclusion

Refer to section 2.3.4 of the main manuscript for the general procedure and reasoning of upper and lower limit calculations.

For this model step, the following assumptions are made:

1. There is exactly one dust inclusion in each mixed particle
2. Carbonaceous matter does not contribute
3. Ca contributes to dust as carbonate
4. Ca contributes to non-dust as sulfate / chloride
5. Fe contributes to dust as  $Fe^{3+}$
6. S contributes as sulfate
7. Na, Mg, Al, Si, P, K, Ti and Fe contribute to the dust according to their oxide weights
8. N-containing compounds contribute only in case of a non-neutral ion balance as ammonium and nitrate
9. Dust density is  $\rho_{dust} = 2650 \frac{kg}{m^3}$ , non-dust density is  $\rho_{nondust} = 2200 \frac{kg}{m^3}$ , averaged from typical dust and non-dust constituents: illite, kaolinite, muscovite, quartz, albite, microcline, calcite, gypsum, halite, sodium sulfate minerals in different hydration states, and mascagnite (Deer et al. 1992; Warneck et al. 2012)

### **Estimation of the upper limit**

Following the above-listed assumptions, the apparent cation/anion charge ratio is defined as

$$r_{cat} = \frac{\sum cations_{charge}}{\sum anions_{charge}} \quad (10)$$

with  $\sum cations_{charge} = |Na| + 2|Mg| + |K| + 2|Ca|$ , apparent sum of cation charges,

and  $\sum anions_{charge} = |Cl| + 2|S|$ , apparent sum of anion charges.

Note that  $|X|$  denominates the concentration of element  $\langle X \rangle$  given as atomic (i.e. molar) fraction relative to the sum of all quantified element concentrations with the exclusion of O and lighter elements:

$$|X_i| = \frac{\langle X_i \rangle}{\sum \langle X \rangle} \quad (11)$$

with  $|X_i|$  element concentration index of a particular element with arbitrary index  $i$ ,  
 $\sum \langle X \rangle$  sum of all considered elements (Na, Mg, Al, Si, P, S, Cl, K, Ca, Ti, Cr, Mn, Fe, Co, if not stated differently).

If  $r_{cat} > 1$ , it is assumed in the upper limit estimate that the excess in the apparent sum of cation charges is produced by the dust contribution. Thus, the dust contribution is calculated as the ion balance excess as

$$c_{dust} = \frac{r_{cat} - 1}{r_{cat}} = \frac{\frac{\sum cations_{charge} - 1}{\sum anions_{charge}}}{\frac{\sum cations_{charge}}{\sum anions_{charge}}} = \frac{\sum cations_{charge} - \sum anions_{charge}}{\sum cations_{charge}} \quad (12)$$

Cation excess

If  $c_{dust} > 0$ , an equal fraction of each element's apparent cation contribution excess is attributed to dust, i.e. the ion charge balance is virtually neutralized for the non-dust component. The dust and non-dust masses are calculated as (see also Table S 2 in the electronic supplement)

$$m_{dust} = \sum dust_{oxides} + c_{dust} \sum cations_{oxide} \quad (13)$$

with  $\sum dust_{oxides} = Al_{oxide} + Si_{oxide} + P_{oxide} + Ti_{oxide} + Fe_{oxide}$ ,

and  $\sum cations_{oxide} = Na_{oxide} + Mg_{oxide} + K_{oxide} + Ca_{carbonate}$ .

Note that stable sulfates (gypsum / anhydrite, alunite) are assigned to the non-dust component.

$$m_{nondust} = (1 - c_{dust}) \sum cations_{mass} + \sum anions_{mass} \quad (14)$$

with  $\sum cations_{mass} = Na_{mass} + Mg_{mass} + K_{mass} + Ca_{mass}$ ,

and  $\sum anions_{mass} = Cl_{mass} + SO_{4,mass}^{2-}$ .

The mass contributions are calculated as shown in Table S 2 in the electronic supplement.

Cation deficit

If  $c_{dust} < 0$ , i.e. there is a cation deficit, the missing cation is assumed to be ammonium. The dust and non-dust masses are then calculated as

$$m_{dust} = \sum oxides \quad (15)$$

$$m_{nondust} = \sum cations_{mass} + \sum anions_{mass} + NH_{4,mass}^+ \quad (16)$$

For calculation of the ammonium mass  $NH_{4,mass}^+$  see Table S 2 in the electronic supplement.

### **Estimation of the lower limit**

The dust mass for lower limit estimate of the dust contribution is calculated according to Eq. (15).

The non-dust mass is calculated for  $c_{dust} < 0$  according to Eq. (16). For  $c_{dust} > 0$  nitrate is assumed to be the missing anion and the non-dust mass is calculated as

$$m_{nondust} = \sum cations_{mass} + \sum anions_{mass} + NO_{3,mass}^- \quad (17)$$

Refer to Table S 2 in the electronic supplement for calculation of the nitrate mass.

### Calculation of the dust fraction

From the dust and non-dust mass contributions, the dust volume contribution to the particle is calculated as

$$f_{dust} = \frac{\frac{m_{dust}}{\rho_{dust}}}{\frac{m_{dust}}{\rho_{dust}} + \frac{m_{nondust}}{\rho_{nondust}}} = \frac{m_{dust}}{m_{dust} + \frac{\rho_{dust}}{\rho_{nondust}} m_{nondust}} \quad (18)$$

and the diameter of the resulting dust inclusion as

$$\frac{\pi}{6} d_{v,dust}^3 = f_{dust} \frac{\pi}{6} d_v^3 \rightarrow d_{v,dust} = f_{dust}^{\frac{1}{3}} d_v \quad (19)$$

### S.3 Statistical uncertainty of total volumes / masses and relative number abundances from single particle measurements

When assessing the uncertainty of values based on counted occurrences, frequently the counting statistics are assumed to follow a Poisson distribution. However, when calculating total aerosol masses or volumes, besides the measurement errors in particular the – usually few – large particles can introduce a considerable statistical uncertainty, which is not necessarily accounted for by the distribution assumption. Therefore, estimates of the statistical uncertainty based on single particle counts for an a priori unknown frequency distribution (i. e. the counting frequency distribution modified by the also unknown particle size distribution) either require reasonable assumptions or distribution-independent estimators. In the present work, the uncertainty is estimated by a bootstrap approach with Monte Carlo approximation (Efron 1979).

For the Poisson approach, with a counting error of  $\Delta n = 1$  for a single particle count ( $n = 1$ ) the Gaussian error propagation of the standard deviation for a sum of particle volumes  $V_k$  resolves to

$$\Delta V = \sqrt{\sum_k \left( \Delta n \frac{\partial}{\partial n} n V_k \right)^2 + \sum_k \left( \Delta V_k \frac{\partial}{\partial V_k} n V_k \right)^2} = \sqrt{\sum_k V_k^2 + \sum_k \Delta V_k^2} \quad (20)$$

with  $n$  the number of particles with Volume  $V_k$ , in this case always 1,  
 $\Delta V_k$  the volume measurement error,  
 $k$  the index for the single particles.

Similar considerations apply for the mass calculations.

The two-sided 95 % confidence interval is estimated for the Poisson distribution case as 1.96 times the standard deviation, and for the bootstrap case as the 0.025 to 0.975 quantile range of the bootstrap replications (bias corrected and accelerated method; DiCiccio et al. 1996; Carpenter et al. 2000).

Considering only the statistical uncertainty from Eq. (20), the distribution-based approach can be compared to the bootstrap approach in terms of relative statistical uncertainty for the volume estimated from two methods (Fig. S 1). Clearly, the Poisson assumption underestimates the lower limit of the two-sided 95 % confidence interval (i.e. overestimates the uncertainty), providing even physically meaningless negative numbers. In contrast, the bootstrap approach yields most probably

more precise estimates (see also Efron 2003). For the upper limit of the interval, the Poisson approach seems to underestimate the uncertainty, in particular with respect to the high volumes which can be present in single particles (Fig. S 1, left). When restricting the size range to particles of 1  $\mu\text{m}$  to 20  $\mu\text{m}$  in diameter (Fig. S 1, right), as expected the differences in confidence interval limits become much smaller and stay mostly below 20 % difference between the two approaches. Note in particular the impact of the volume in the single largest particle. For the present work, the bootstrap approach is preferred.

For the assessment of the confidence interval of relative counting abundances, frequently a confidence interval based on a binomial distribution is used as estimate (Agresti et al. 1998), i.e. for a relative number abundance of a certain particle type class  $r$  the two-sided 95 % confidence interval is approximated as (Hartung et al. 2005)

$$CL_{0.025,0.975} = \frac{3.84 + 2r \mp \sqrt{3.84 \left(3.84 + 4r \frac{n-r}{n}\right)}}{2(n + 3.84)} \quad (21)$$

with  $r$  the count of particles in that class,  
 $n$  the total number of particles.

The two approaches show much closer agreement here than in the previous case (see Fig. S 2). Note that if the common Wald confidence interval is used (Agresti et al. 1998), with lower absolute particle numbers in a class, an increasing tendency of over/underestimation similar to the previous case occurs up to meaningless negative values in the binomial case. For sake of consistence, in the present work also for the relative abundances the robust bootstrap approach for estimation of the confidence intervals was chosen.

## S.4 Determining the size distributions from the free-wing impactor measurements

First, a window correction accounting for the exclusion of particles at the analysis image border is applied (Kandler et al. 2009):

$$c_w = \frac{w_x w_y}{(w_x - d_p)(w_y - d_p)} \quad (22)$$

Second, the collection efficiency of the FWI has to be regarded. Therefore, the ambient particle diameter at the time of collection has to be estimated by accounting for the hygroscopic particle growth:

$$d_{amb} = d_v g_{hyg} \quad (23)$$

with  $g_{hyg}$  the hygroscopic growth factor.

Hygroscopic growth can be estimated from the hygroscopicity parameter  $\kappa$  (Petters et al. 2007) as

$$g_{hyg} = \left(1 + \frac{a_w}{1 - a_w} \kappa\right)^{\frac{1}{3}} \quad (24)$$

with  $a_w$  the water activity.

As only super-micron particles are considered in this part of the study, the water activity can be equated with the relative humidity given as fraction. The hygroscopicity parameter can be determined as volume-weighted average of the hygroscopicity parameters of the major contributing components (Petters et al. 2007). Assuming a mixture of sodium sulfate and sodium chloride as the components dominating the hygroscopic growth and assigning the dust component zero hygroscopicity, the hygroscopicity parameter is approximated from the volume contributions as

$$\kappa = (1 - f_{dust}) \frac{0.68 \times Na_2SO_{4,volume} + 1.12 \times NaCl_{volume}}{Na_2SO_{4,volume} + NaCl_{volume}} \quad (25)$$

For the calculation of the volume contributions, refer to Table S 2 in the electronic supplement.

The collection efficiency  $E(P)$  is parameterized (see below) from the experimentally determined values for discs given by May et al. (1967) as a function of impaction parameter  $P$ :

$$P = \frac{S}{D} \quad (26)$$

with  $S$  stopping distance,  
 $D$  characteristic dimension, here 12.5 mm.

While  $P$  equals to the Stokes number within the Stokes regime, in the current work the particle Reynolds numbers are considerably higher. In this regime, in analogy to Hinds (1999) the stopping distance can be approximated with better than 3 % accuracy as

$$S = \frac{\rho_{amb} d_{amb}}{\rho_a \sqrt{\chi}} \left[ Re_p^{\frac{1}{3}} - \sqrt{6} \tan^{-1} \left( \frac{Re_p^{\frac{1}{3}}}{\sqrt{6}} \right) \right] \quad (27)$$

with  $\rho_{amb}$  ambient particle density, estimated from chemical composition and growth factor,  
 $\rho_a$  air density,  
 $\chi$  aerodynamic shape factor.

Results of the trigonometric function must be given as radian. The dry aerodynamic shape factor is assumed as constant similar to Ott et al. (2008), but is interpolated for particles mixed with water as function of the hygroscopic growth factor:

$$\chi = \begin{cases} 1 + (\chi_0 - 1) \left( 1 - \frac{(g_{hyg} - 1)}{(g_{hyg,lim} - 1)} \right) & g_{hyg} < g_{hyg,lim} \\ 1 & g_{hyg} > g_{hyg,lim} \end{cases} \quad (28)$$

with  $\chi_0 = 1.4$  an estimated dry shape factor (Ott et al. 2008)  
 $g_{hyg,lim} = 1.3$  a hygroscopic growth factor at which the particles are assumed to be spherical.

The particle Reynolds number is

$$Re_p = \frac{\rho_a v_i d_{amb}}{\eta \sqrt{\chi}} \quad (29)$$

with  $v_i = \sqrt{v_r^2 + v^2}$  the impaction velocity  
 $v_r = 2\pi l f_r$  the speed of the collector in the plane of rotation  
 $l$  the collector arm length  
 $f_r$  the rotation frequency  
 $v$  the wind speed  
 $\eta$  the viscosity of the air.

The stopping distances calculated by Eq. (27) are well in accordance with the parameterization curves shown by May et al. (1967).

The collection  $E(P)$  efficiency for  $P > 0.125$  is then parameterized (see Fig. S 4 in the electronic supplement) and the according correction is

$$c_e = \frac{1}{E(P)} = \exp\left(\frac{0.28}{P}\right) \quad (30)$$

The total investigated volume for the concentration calculations is determined by

$$V_i = A v_i t_i \quad (31)$$

with  $A$  the analyzed area,  
 $t_i$  the sample collection time.

The atmospheric concentration is finally

$$C(d_{amb}) = \frac{1}{V_i} \sum_k c_w(d_{p,k}) c_e(d_{amb,k}) \quad (32)$$

with  $k$  index of the particle.

## S.5 Determining the airborne size distributions from the sedimentation sampler measurements

Similar to the previous section, sampling efficiency considerations are necessary for the sedimentation sampler. For the supermicron particle size range sedimentation and turbulent impaction dominate the particle deposition velocity. To calculate the turbulent impaction velocity, which depends of the wind speed, the friction velocity is needed. As the opposing inner boundary layers of the sampler plates are always separated for the considered range of wind speeds (boundary layer thickness between 4.5 mm and 2 mm for wind speeds between 3.5 m/s and 13.5 m/s; Munson et al. 2013), the flow inside the sampler is approximated as flow over a smooth flat plate (the lower plate). The friction velocity is calculated as recommended by Wood (1981):

$$u^* = \frac{v}{\sqrt{2}} (2 \log_{10} Re_s - 0.65)^{-1.15} \quad (33)$$

with  $Re_s = \frac{\rho_a v x}{\eta}$  the flow Reynolds number at the sampling stub location,  
 $x$  the distance from the lower plate edge to the center of the sampling stub (6.3 cm).

Considering the flow inside the sampler as tube flow (Liu et al. 1974) would lead to friction velocities differing by less than 5 %.

The deposition velocity is estimated by the following formalism, following the approach of Piskunov (2009):

$$v_d = \frac{u^*}{J_1 + J_2} \quad (34)$$

$$J_1 = \frac{u^* \exp(-1.2\tau^+)}{v_{Stk}} \left[ 1 - \exp\left(-13.204 Sc^{\frac{2}{3}} \frac{v_{Stk}}{u^*}\right) \right] \quad (35)$$

with  $Sc = \frac{\eta}{\rho_a C_D} = \frac{3\pi \eta^2 d_{amb}}{\rho_a k_B T C_c \sqrt{\chi}}$  the Schmidt number,  
 $C_D$  the particle diffusion coefficient,  
 $k_B$  the Boltzmann constant,  
 $T$  the ambient temperature,  
 $C_c = 1 + 2 \frac{\lambda \sqrt{\chi}}{d_{amb}} \left[ 1.257 + 0.4 \exp\left(-\frac{1.1 d_{amb}}{2\lambda \sqrt{\chi}}\right) \right]$  the Cunningham slip correction,  
 $\lambda = \frac{k_B T}{\sqrt{2} \pi d_M^2 P}$  the mean free path,  
 $d_M = 3.68 \times 10^{-10}$  m the average diameter of an air molecule,  
 $P$  the ambient pressure,  
 $v_{Stk} = \frac{12 \eta \sqrt{\chi}}{0.42 C_c \rho_a d_{amb}} \left[ \sqrt{1 + \frac{0.42 C_c^2 \rho_a \rho_{amb}}{108 \eta^2} \left(\frac{d_{amb}}{\sqrt{\chi}}\right)^3 \left(1 - \frac{\rho_a}{\rho_{amb}}\right) g} - 1 \right]$  the gravitational settling velocity,  
 $g$  the gravitational acceleration;

$$J_2 = \frac{1 - \exp\left[-\gamma \left(1 + \frac{v_{Stk}}{u^* p_\tau}\right)\right]}{p_\tau + \frac{v_{Stk}}{u^*}} \quad (36)$$

with  $\gamma = \frac{0.4611 Sc \tau^+ (1 + 0.3859 \tau^+)}{(1 + 0.1193 \tau^+)(1 + 0.1193 \tau^+ + 6.613 Sc)}$   
 $\tau^+ = \frac{u^{*2} \rho_a v_{Stk}}{\eta g}$  the dimensionless relaxation time,  
 $p_\tau = \frac{\tau^+ (1 + 0.3859 \tau^+)}{65.06 (1 + 0.1193 \tau^+)^2}$

The atmospheric concentrations are then

$$C(d_{amb}) = \frac{1}{A t_i} \sum_k \frac{c_w(d_{p,k})}{v_d(d_{amb,k})} \quad (37)$$

A major bias for this calculation originates from the uncertainty in (turbulent) deposition velocity.

The aerodynamic diameter used here is calculated as:

$$d_a = \sqrt{\frac{\rho_{amb}}{\rho_0 \chi}} d_{amb} \quad (38)$$

with  $\rho_0 = 1000 \frac{\text{kg}}{\text{m}^3}$  unity density.

## Literature

- Agresti, A., B. A. Coull (1998): Approximate Is Better than "Exact" for Interval Estimation of Binomial Proportions. *Am. Stat.* 52(2), 119-126. doi: 10.2307/2685469
- Carpenter, J., J. Bithell (2000): Bootstrap confidence intervals: when, which, what? A practical guide for medical statisticians. *Stat. Med.* 19(9), 1141-1164. doi: 10.1002/(sici)1097-0258(20000515)19:9<1141::aid-sim479>3.0.co;2-f
- Deer, W. A., R. A. Howie, J. Zussman (1992): *An Introduction to the Rock-Forming Minerals*. Second Edition. Harlow, UK, Pearson Education Ltd.
- DiCiccio, T. J., B. Efron (1996): Bootstrap confidence intervals. *Statist. Sci.* 11(3), 189-228. doi: 10.1214/ss/1032280214
- Efron, B. (1979): Bootstrap Methods: Another Look at the Jackknife. *Ann. Statist.*(1), 1-26. doi: 10.1214/aos/1176344552
- Efron, B. (2003): Second Thoughts on the Bootstrap. *Statist. Sci.* 18(2), 135-140. doi: 10.1214/ss/1063994968
- Hartung, J., B. Elpelt, K.-H. Klösener (2005): *Statistik: Lehr- und Handbuch der angewandten Statistik*, Oldenbourg, Munich, Germany.
- Hinds, W. C. (1999): *Aerosol Technology. Properties, behavior, and measurement of airborne particles*. Second edition. New York, USA, Wiley Interscience.
- Kandler, K., L. Schütz, C. Deutscher, H. Hofmann, S. Jäckel, P. Knippertz, K. Lieke, A. Massling, A. Schladitz, B. Weinzierl, S. Zorn, M. Ebert, R. Jaenicke, A. Petzold, S. Weinbruch (2009): Size distribution, mass concentration, chemical and mineralogical composition, and derived optical parameters of the boundary layer aerosol at Tinfou, Morocco, during SAMUM 2006. *Tellus 61B*, 32-50. doi: 10.1111/j.1600-0889.2008.00385.x
- Kristensen, T. B., T. Müller, K. Kandler, N. Benker, M. Hartmann, J. M. Prospero, A. Wiedensohler, F. Stratmann (2016): Properties of cloud condensation nuclei (CCN) in the trade wind marine boundary layer of the western North Atlantic. *Atmos. Chem. Phys.* 16(4), 2675-2688. doi: 10.5194/acp-16-2675-2016
- Liu, B. Y. H., J. K. Agarwal (1974): Experimental observation of aerosol deposition in turbulent flow. *J. Aerosol Sci.* 5(2), 145-155. doi: 10.1016/0021-8502(74)90046-9
- May, K. R., R. Clifford (1967): The impaction of aerosol particles on cylinders, spheres, ribbons and discs. *Ann. Occup. Hyg.* 10, 83-95.
- Munson, B. R., T. H. Okiishi, W. W. Huebsch, A. P. Rothmayer (2013): *Fundamentals of Fluid Mechanics*, 7th Edition, John Wiley & Sons.
- Ott, D. K., W. Cyrs, T. M. Peters (2008): Passive measurement of coarse particulate matter, PM<sub>10-2.5</sub>. *J. Aerosol Sci.* 39(2), 156-167. doi: 10.1016/j.jaerosci.2007.11.002
- Petters, M. D., S. M. Kreidenweis (2007): A single parameter representation of hygroscopic growth and cloud condensation nucleus activity. *Atmos. Chem. Phys.* 7(8), 1961-1971. doi: 10.5194/acp-7-1961-2007
- Piskunov, V. N. (2009): Parameterization of aerosol dry deposition velocities onto smooth and rough surfaces. *J. Aerosol Sci.* 40(8), 664-679. doi: 10.1016/j.jaerosci.2009.04.006
- Warneck, P., J. Williams (2012): *The Atmospheric Chemist's Companion. Numerical Data for Use in the Atmospheric Sciences*, Springer Netherlands.
- Wood, N. B. (1981): A simple method for the calculation of turbulent deposition to smooth and rough surfaces. *J. Aerosol Sci.* 12(3), 275-290. doi: 10.1016/0021-8502(81)90127-0

Table S 1: Sample denominations and collection times for the campaigns in 2013 and 2016.

2013						2016					
DPDS sample	starting time (UTC), year-month-day hour:minute	duration, hours:minutes	FWI sample	starting time (UTC), year-month-day hour:minute	duration, hours:minutes	CI sample	starting time (UTC), year-month-day hour:minute	duration, hours:minutes	DPDS sample	starting time (UTC), year-month-day hour:minute	duration, hours:minutes
RPS_001	2013-06-14 21:19	19:06	RPF_01	2013-06-15 15:48	0:30	RPE_01	2013-06-15 15:50	0:10	RPS_031	2016-08-06 20:50	17:15
RPS_002	2013-06-15 16:25	20:41							RPS_032	2016-08-07 14:10	26:10
RPS_003	2013-06-16 13:08	25:29	RPF_02	2013-06-16 13:16	0:30	RPE_02	2013-06-16 13:20	0:10	RPS_033	2016-08-08 16:20	21:32
RPS_004	2013-06-17 14:39	23:09	RPF_03	2013-06-17 14:42	0:30	RPE_03	2013-06-17 14:55	0:10	RPS_034	2016-08-09 13:52	23:58
RPS_005	2013-06-18 13:49	23:15	RPF_04	2013-06-18 13:50	0:30	RPE_04	2013-06-18 14:00	0:06	RPS_035	2016-08-10 13:50	25:48
RPS_006	2013-06-19 13:04	24:23	RPF_05	2013-06-19 13:12	0:30	RPE_05	2013-06-19 13:15	0:10	RPS_036	2016-08-11 15:38	2:43
RPS_007	2013-06-20 13:27	28:19	RPF_06	2013-06-20 13:37	0:30	RPE_06	2013-06-20 13:40	0:20	RPS_037	2016-08-11 18:21	19:26
RPS_008	2013-06-21 17:46	25:16	RPF_07	2013-06-21 18:20	1:00	RPE_07	2013-06-21 18:10	0:20	RPS_038	2016-08-12 13:47	23:30
RPS_009	2013-06-22 19:02	42:08	RPF_08	2013-06-22 19:05	0:30	RPE_08	2013-06-22 19:20	0:20	RPS_039	2016-08-13 13:17	23:54
RPS_010	2013-06-24 13:10	24:13	RPF_09	2013-06-24 13:14	1:30	RPE_09	2013-06-24 13:20	0:40	RPS_040	2016-08-14 13:11	23:23
RPS_011	2013-06-25 13:23	23:32	RPF_10	2013-06-25 14:27	1:47	RPE_10	2013-06-25 14:30	1:00	RPS_041	2016-08-15 12:34	24:26
RPS_013	2013-06-26 12:55	24:21	RPF_11	2013-06-26 12:58	1:00	RPE_11	2013-06-26 13:00	0:30	RPS_042	2016-08-16 13:00	27:35
			RPF_12	2013-06-27 02:43	1:00	RPE_12	2013-06-27 02:30	0:30	RPS_043	2016-08-17 16:35	22:05
RPS_014	2013-06-27 13:16	24:10	RPF_13	2013-06-27 13:20	0:20	RPE_13	2013-06-27 13:30	0:30	RPS_044	2016-08-18 14:40	21:06
			RPF_13B	2013-06-27 15:49	1:15				RPS_045	2016-08-19 11:46	26:08
RPS_015	2013-06-28 13:26	23:43	RPF_14	2013-06-28 13:38	1:00	RPE_14	2013-06-28 13:45	0:30	RPS_046	2016-08-20 13:54	22:15
RPS_016	2013-06-29 13:09	24:17				RPE_15	2013-06-29 13:10	0:48	RPS_047	2016-08-21 12:09	24:41
RPS_017	2013-06-30 13:26	23:39	RPF_16	2013-06-30 15:47	0:30	RPE_16	2013-06-30 13:35	0:15	RPS_048	2016-08-22 12:50	23:47
RPS_018	2013-07-01 13:05	23:20	RPF_17	2013-07-01 13:11	1:00	RPE_17	2013-07-01 13:20	0:20	RPS_049	2016-08-23 12:37	23:32
RPS_019	2013-07-02 12:25	23:28	RPF_18	2013-07-02 12:31	1:13	RPE_18	2013-07-02 12:25	0:40	RPS_050	2016-08-24 12:09	23:54
RPS_020	2013-07-03 11:53	25:43	RPF_19	2013-07-03 11:58	1:08	RPE_19	2013-07-03 11:55	0:45	RPS_051	2016-08-25 12:03	23:37
RPS_021	2013-07-04 13:36	23:20	RPF_20	2013-07-04 13:43	0:30	RPE_20	2013-07-04 13:35	0:30	RPS_052	2016-08-26 11:40	23:16
RPS_022	2013-07-05 12:56	23:22	RPF_21	2013-07-05 13:01	1:00	RPE_21	2013-07-05 13:00	0:40			
RPS_023	2013-07-06 12:18	25:52	RPF_22	2013-07-06 12:16	1:20	RPE_22	2013-07-06 12:14	0:45			
RPS_024	2013-07-07 14:10	24:16	RPF_23	2013-07-07 14:20	1:00	RPE_23	2013-07-07 14:15	1:00			
RPS_025	2013-07-08 14:26	47:40	RPF_24	2013-07-08 17:15	0:30	RPE_24	2013-07-08 17:30	0:25			
RPS_026	2013-07-10 14:06	22:45	RPF_25	2013-07-10 15:00	0:30	RPE_25	2013-07-10 15:00	0:15			
RPS_027	2013-07-11 12:51	22:26	RPF_26	2013-07-11 12:57	0:23	RPE_26	2013-07-11 13:00	0:15			
RPS_028	2013-07-12 11:17	25:56	RPF_27	2013-07-12 11:17	0:30	RPE_27	2013-07-12 11:24	0:20			
RPS_029	2013-07-13 13:13	24:00	RPF_28	2013-07-13 13:19	1:00	RPE_28	2013-07-13 13:15	0:40			
RPS_030	2013-07-14 13:13	23:40	RPF_29	2013-07-14 13:18	1:52	RPE_29	2013-07-14 13:20	0:50			
			RPF_30	2013-07-15 12:58	1:30	RPE_30	2013-07-15 13:00	0:40			

**Table S 2: Conversion formulas used for the calculation of oxide, carbonate, element atomic and ammonium masses, as well as sodium sulfate and sodium chloride volumes. Values were taken from Deer et al. (1992) and Warneck et al. (2012).**

$Al_{oxide} = 101.96 \frac{g}{mol} \times \frac{ Al }{2}$ $Si_{oxide} = 60.08 \frac{g}{mol} \times  Si $ $P_{oxide} = 141.94 \frac{g}{mol} \times \frac{ P }{2}$ $Ti_{oxide} = 79.88 \frac{g}{mol} \times  Ti $ $Fe_{oxide} = 159.69 \frac{g}{mol} \times \frac{ Fe }{2}$	$Na_{oxide} = 61.98 \frac{g}{mol} \times \frac{ Na }{2}$ $Mg_{oxide} = 40.30 \frac{g}{mol} \times  Mg $ $K_{oxide} = 94.20 \frac{g}{mol} \times \frac{ K }{2}$ $Ca_{carbonate} = 100.09 \frac{g}{mol} \times  Ca $
$Na_{mass} = 22.99 \frac{g}{mol} \times  Na $ $Mg_{mass} = 24.31 \frac{g}{mol} \times  Mg $ $K_{mass} = 39.10 \frac{g}{mol} \times  K $ $Ca_{mass} = 40.08 \frac{g}{mol} \times  Ca $	$Cl_{mass} = 35.45 \frac{g}{mol} \times  Cl $ $SO_{4,mass} = 96.06 \frac{g}{mol} \times  S $ $NH_{4,mass} = -18.04 \frac{g}{mol} \times c_{dust}$ $NO_{3,mass} = 62.00 \frac{g}{mol} \times c_{dust}$
$Na_2SO_{4,volume} = \frac{142.04 \frac{g}{mol} \times  X }{2.66 \frac{g}{cm^3}} \begin{cases} X = Na, \text{ if classified as insoluble sulfate} \\ X = S \text{ in other cases} \end{cases}$ $NaCl_{volume} = \frac{58.44 \frac{g}{mol} \times  Cl }{2.17 \frac{g}{cm^3}}$	

**Table S 3: Relationships between area coverage of the simulated 5 mm x 5 mm analysis field, particle numbers, particle masses and uncertainties. Upper part: CV-ground size distribution, lower part: CV-air size distribution. A bulk density of 2500 kg/m<sup>3</sup> was assumed for the mass estimation from particle volume. Abbreviations: SP coverage = ratio of the sum of single particle cross sections to the analysis field; apparent coverage = fraction of area covered by the particles after deposition; N<sub>>1</sub> = Number of particles larger than 1 µm diameter; PM<sub>>1</sub> = Total mass of particles larger than 1 µm diameter (approx. 99.99 % of total mass); PM<sub>1-32</sub> = total mass of particles between 1 µm and 32 µm diameter (approx. 50 % of total mass for source-near size distribution, 67 % for aged one). Relative uncertainty is given as the ratio of the upper and lower bounds of the central 95 % quantile to the median of 1000 (200 for SP coverage >= 0.1) repetitions of deposition simulation.**

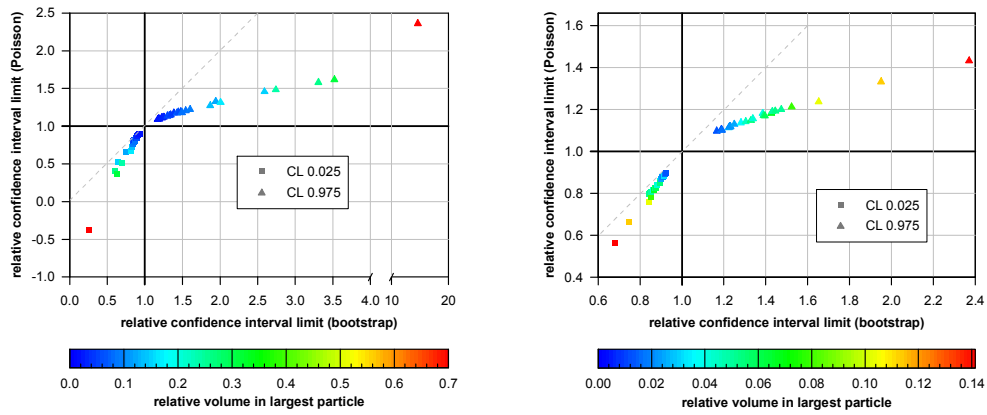
SP coverage	Apparent coverage	N <sub>&gt;1</sub>	PM <sub>&gt;1</sub> , µg	relative uncertainty	PM <sub>1-32</sub> , µg	relative uncertainty
0.001	0.001	353	0.8	0.38 - 4.16	0.5	0.56 - 1.38
0.003	0.002	865	2.7	0.37 - 4.68	1.3	0.69 - 1.24
0.005	0.005	1699	4.6	0.53 - 3.60	2.5	0.78 - 1.18
0.006	0.006	2032	6.1	0.49 - 2.80	3.0	0.81 - 1.17
0.007	0.007	2361	6.9	0.54 - 2.76	3.5	0.82 - 1.16
0.008	0.008	2692	7.6	0.56 - 2.59	4.0	0.83 - 1.14
0.009	0.009	3016	8.3	0.58 - 2.57	4.5	0.84 - 1.14
0.010	0.010	3344	10	0.54 - 2.21	5.0	0.85 - 1.13
0.011	0.011	3669	11	0.57 - 2.26	5.5	0.85 - 1.13
0.012	0.012	3988	11	0.63 - 2.18	5.9	0.86 - 1.12
0.013	0.013	4313	13	0.64 - 2.03	6.4	0.87 - 1.12
0.015	0.015	4951	14	0.67 - 1.95	7.4	0.88 - 1.11
0.020	0.020	6520	20	0.69 - 2.09	9.8	0.89 - 1.10
0.025	0.025	8047	24	0.74 - 1.94	12	0.90 - 1.09
0.035	0.034	10998	34	0.77 - 1.71	17	0.92 - 1.07
0.050	0.048	15146	56	0.69 - 1.48	24	0.93 - 1.06
0.075	0.071	21379	81	0.75 - 1.45	36	0.94 - 1.05
0.100	0.093	26824	106	0.79 - 1.35	47	0.95 - 1.05
0.200	0.172	34099	218	0.80 - 1.53	89	0.97 - 1.04
0.001	0.001	1031	0.7	0.44 - 3.05	0.5	0.66 - 1.33
0.005	0.005	5056	3.6	0.73 - 1.84	2.4	0.84 - 1.15
0.010	0.010	9990	8.1	0.71 - 1.42	4.8	0.89 - 1.11
0.025	0.025	24102	19.8	0.79 - 1.27	11.9	0.93 - 1.07
0.050	0.048	45618	39.4	0.82 - 1.38	23.4	0.95 - 1.05
0.075	0.071	64665	59.1	0.85 - 1.29	34.6	0.96 - 1.04
0.100	0.093	81568	78.5	0.89 - 1.23	45.4	0.97 - 1.04
0.150	0.134	109224	118	0.90 - 1.17	65.7	0.97 - 1.03
0.200	0.173	129769	158	0.91 - 1.13	84.2	0.97 - 1.02

Table S 4: 95 % quantile of the fractions of internally mixed particles due to coincidental mixture on the substrate, for a two-component system with CV-ground size distribution. Strong mixture refers to a minimum particle volume fraction of the other component of 20 %, detectable mixture refers to 1 %. Only values larger than 0.001 are shown, values larger than 0.05 are highlighted in bold.

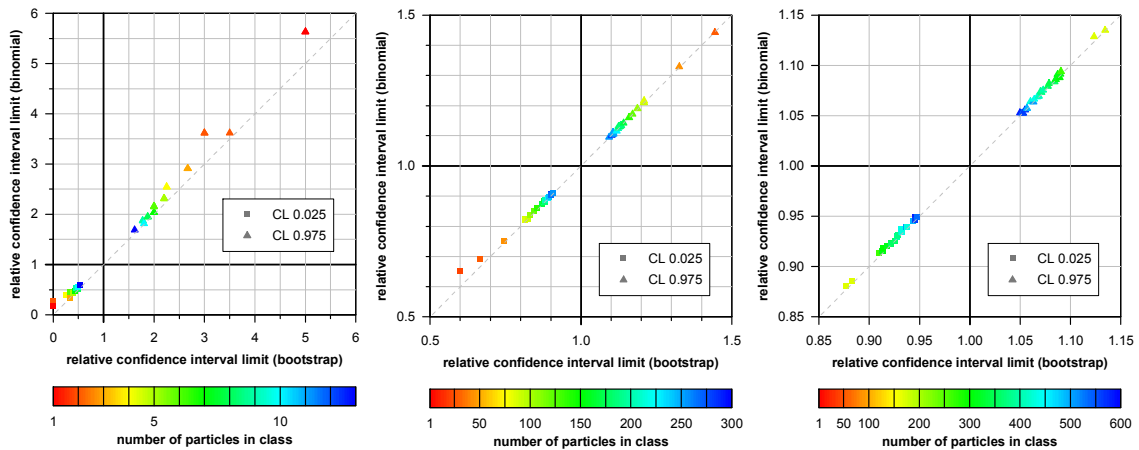
<i>strong mixture</i>		size range, $\mu\text{m}$						
component ratio	apparent area coverage	>1-2	>2-4	>4-8	>8-16	>16-32	>32-64	>64-128
50 % / 50 %	0.001				.007			
	0.005			.002	.007	.027		
	0.010			.002	.010	.032	.042	
	0.025		.001	.003	.018	<b>.051</b>	.038	
	0.048		.001	.004	.032	<b>.084</b>	.044	<b>.077</b>
	0.071		.001	.006	.045	<b>.116</b>	<b>.053</b>	<b>.077</b>
	0.093		.002	.007	<b>.057</b>	<b>.145</b>	<b>.064</b>	<b>.086</b>
	0.172	.001	.002	.012	<b>.102</b>	<b>.254</b>	<b>.121</b>	<b>.108</b>
90 % / 10 %	0.001							
	0.005			.002	.003	.014		
	0.010				.004	.018		
	0.025		.001	.001	.007	.023	.024	
	0.048			.002	.012	.034	.023	<b>.059</b>
	0.071			.002	.017	.045	.025	<b>.050</b>
	0.093			.003	.021	<b>.055</b>	.031	.040
	0.172		.001	.005	.037	<b>.091</b>	.046	<b>.051</b>
99 % / 1 %	0.001							
	0.005				.001			
	0.010					.006		
	0.025				.001	.005		
	0.048				.002	.006	.010	
	0.071				.002	.007	.008	
	0.093				.003	.008	.006	
	0.172				.005	.011	.008	.016
<i>detectable mixture</i>		size range, $\mu\text{m}$						
component ratio	apparent area coverage	>1-2	>2-4	>4-8	>8-16	>16-32	>32-64	>64-128
50 % / 50 %	0.001				.008	.043		
	0.005			.003	.011	<b>.050</b>	<b>.167</b>	
	0.010		.003	.003	.015	<b>.071</b>	<b>.158</b>	<b>.250</b>
	0.025		.002	.005	.029	<b>.125</b>	<b>.214</b>	<b>.286</b>
	0.048		.003	.008	<b>.054</b>	<b>.206</b>	<b>.327</b>	<b>.333</b>
	0.071	.001	.003	.011	<b>.077</b>	<b>.284</b>	<b>.427</b>	<b>.409</b>
	0.093	.001	.004	.014	<b>.098</b>	<b>.354</b>	<b>.526</b>	<b>.500</b>
	0.172	.002	.007	.025	<b>.176</b>	<b>.563</b>	<b>.777</b>	<b>.836</b>
90 % / 10 %	0.001							
	0.005			.002	.005	.027	<b>.100</b>	
	0.010			.002	.007	.034	<b>.083</b>	
	0.025		.001	.002	.012	<b>.051</b>	<b>.104</b>	<b>.167</b>
	0.048		.001	.003	.020	<b>.083</b>	<b>.146</b>	<b>.182</b>
	0.071		.002	.004	.029	<b>.110</b>	<b>.178</b>	<b>.200</b>
	0.093		.002	.005	.037	<b>.133</b>	<b>.210</b>	<b>.217</b>
	0.172		.003	.010	<b>.065</b>	<b>.221</b>	<b>.331</b>	<b>.294</b>
99 % / 1 %	0.001							
	0.005				.002			
	0.010				.002	.007		
	0.025				.002	.010	.026	
	0.048				.003	.013	.029	.067
	0.071				.004	.015	.033	.056
	0.093				.005	.018	.035	.049
	0.172			.001	.008	.027	<b>.050</b>	<b>.053</b>

Table S 5: 95 % quantile of the fractions of internally mixed particles due to coincidental mixture on the substrate, for a two-component system with CV-air size distribution. Strong mixture refers to a minimum particle volume fraction of the other component of 20 %, detectable mixture refers to 1 %. Only values larger than 0.001 are shown, values larger than 0.05 are highlighted in bold.

<i>strong mixture</i>		size range, $\mu\text{m}$						
component ratio	apparent area coverage	>1-2	>2-4	>4-8	>8-16	>16-32	>32-64	>64-128
50 % / 50 %	0.001			.005				
	0.005		.001	.004	.007	.014		
	0.010		.002	.005	.009	.020	.053	
	0.025		.003	.010	.016	.032	.049	
	0.048		.005	.017	.027	<b>.052</b>	<b>.059</b>	
	0.093	.002	.010	.032	.049	<b>.090</b>	<b>.090</b>	<b>.154</b>
	0.134	.002	.014	.046	<b>.070</b>	<b>.128</b>	<b>.127</b>	<b>.167</b>
	0.173	.003	.019	<b>.060</b>	<b>.092</b>	<b>.166</b>	<b>.163</b>	<b>.176</b>
90 % / 10 %	0.001							
	0.005			.002	.003	.012		
	0.010			.002	.004	.011		
	0.025		.001	.004	.007	.014	.024	
	0.048		.002	.007	.011	.021	.031	
	0.093		.004	.012	.019	.034	.039	<b>.111</b>
	0.134		.005	.017	.027	.049	<b>.053</b>	<b>.091</b>
	0.173	.001	.007	.022	.034	<b>.061</b>	<b>.063</b>	<b>.095</b>
99 % / 1 %	0.001							
	0.005							
	0.010				.001			
	0.025				.002	.002		
	0.048			.001	.002	.004	.010	
	0.093			.002	.003	.005	.009	
	0.134			.002	.003	.007	.012	
	0.173			.003	.004	.008	.011	<b>.053</b>
<i>detectable mixture</i>		size range, $\mu\text{m}$						
component ratio	apparent area coverage	>1-2	>2-4	>4-8	>8-16	>16-32	>32-64	>64-128
50 % / 50 %	0.001		.002	.005	.013	<b>.050</b>		
	0.005		.002	.008	.020	.043	<b>.125</b>	
	0.010		.003	.012	.029	<b>.059</b>	<b>.143</b>	
	0.025	.001	.006	.024	<b>.059</b>	<b>.106</b>	<b>.186</b>	<b>.500</b>
	0.048	.002	.010	.045	<b>.108</b>	<b>.188</b>	<b>.278</b>	<b>.521</b>
	0.093	.003	.019	<b>.085</b>	<b>.199</b>	<b>.329</b>	<b>.453</b>	<b>.667</b>
	0.134	.004	.028	<b>.121</b>	<b>.278</b>	<b>.453</b>	<b>.599</b>	<b>.750</b>
	0.173	.006	.037	<b>.156</b>	<b>.352</b>	<b>.556</b>	<b>.714</b>	<b>.864</b>
90 % / 10 %	0.001			.005	.011			
	0.005		.001	.004	.009	.022	<b>.071</b>	
	0.010		.001	.005	.013	.027	<b>.071</b>	
	0.025		.002	.010	.024	.045	<b>.093</b>	<b>.333</b>
	0.048		.004	.017	.041	<b>.073</b>	<b>.124</b>	<b>.333</b>
	0.093	.001	.007	.031	<b>.073</b>	<b>.126</b>	<b>.185</b>	<b>.333</b>
	0.134	.002	.010	.045	<b>.104</b>	<b>.171</b>	<b>.236</b>	<b>.400</b>
	0.173	.002	.014	<b>.057</b>	<b>.131</b>	<b>.213</b>	<b>.287</b>	<b>.409</b>
99 % / 1 %	0.001							
	0.005			.001	.003	.011		
	0.010			.001	.003	.006		
	0.025			.002	.004	.009	.023	
	0.048			.002	.006	.012	.027	
	0.093			.004	.009	.017	.029	<b>.111</b>
	0.134		.001	.005	.013	.022	.036	<b>.111</b>
	0.173		.002	.007	.016	.027	.044	<b>.111</b>



**Fig. S 1:** Comparison of the relative two-sided 95 % confidence interval limits for bootstrap and Poisson approaches. Values shown are the confidence interval limits for the total deposited particle volume divided by this volume. Data basis are the deposition samples at Ragged Point of 2013. Left: for all particles; right: for particles between 1  $\mu\text{m}$  and 20  $\mu\text{m}$  diameter. The color shows the fraction of the total volume present in the single largest particle. Note the different scales between the graphs.



**Fig. S 2:** Comparison of two-sided 95 % confidence interval limits relative to the relative number abundance of a particle type class. Data basis are the deposition samples at Ragged Point. a: for a low-abundance class (0–1.2 % relative number abundance); b: for a medium-abundance class (2.4–41.8 %); c: for a high-abundance class (27.5–61.9 %). The color shows the absolute number of particles in the according class. Note the different scales between the graphs.

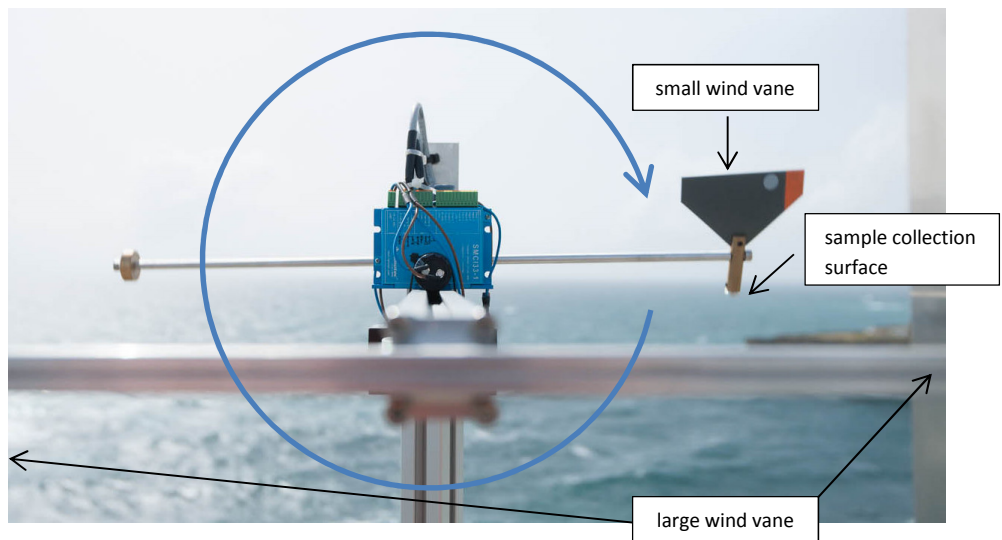


Fig. S 3: Free-wing impactor during rotation (indicated by the blue arc) depicted with  $1.25 \times 10^{-5}$  s exposure time. Wind is blowing towards the observer. Note the inclined orientation of the sampling substrate on the right relative to the rotation plane, aligned with the sum vector of wind and rotation movement.

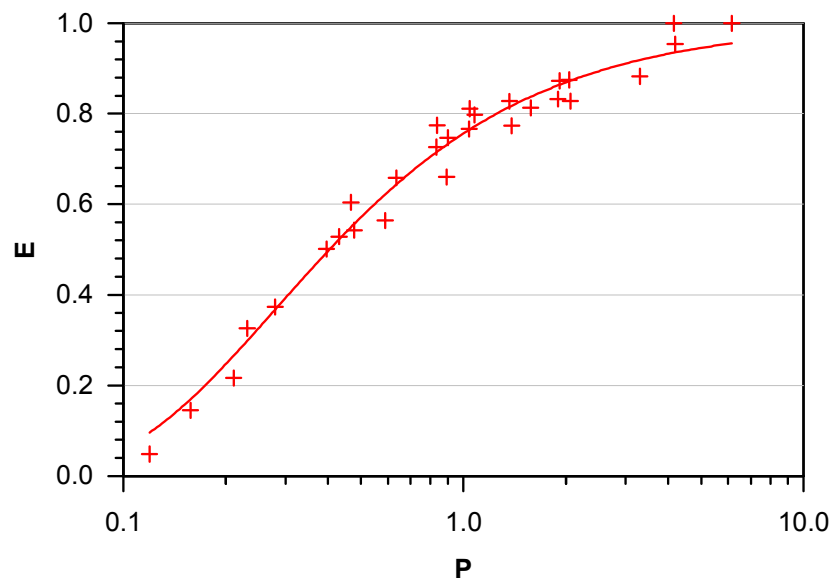


Fig. S 4: Parameterization of collection efficiency  $E$  of a disc as function of impactation parameter  $P$ ; fit to the data of May et al. (1967). Fit function is shown as continuous line.

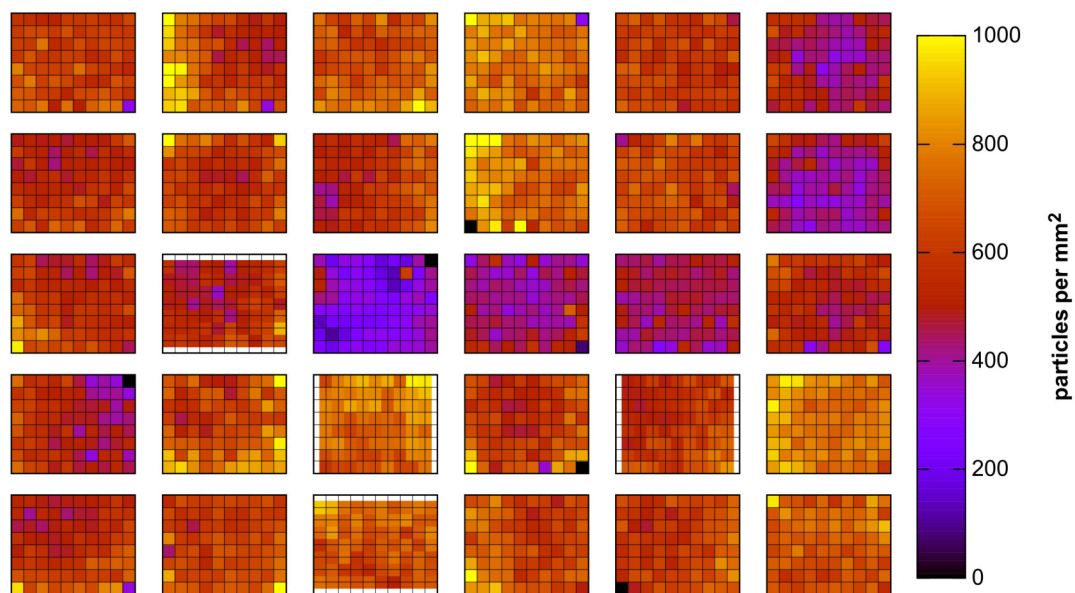


Fig. S 5: Maps of particle deposition density on the FWI substrates for  $4 \mu\text{m} < d_g < 8 \mu\text{m}$ . Each division on the x and y axes equals 1 mm distance.

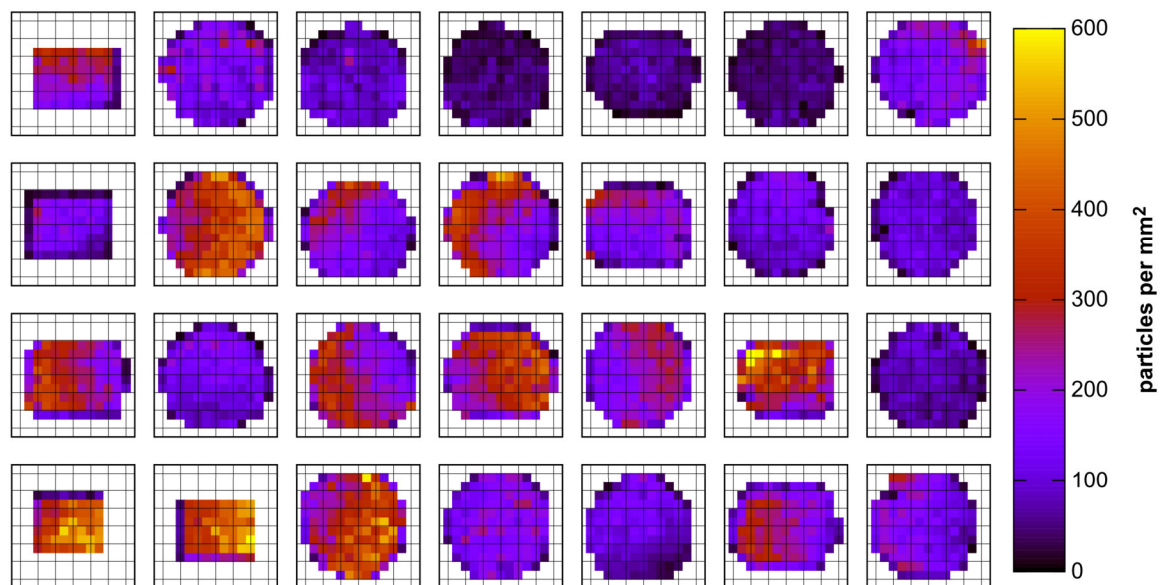
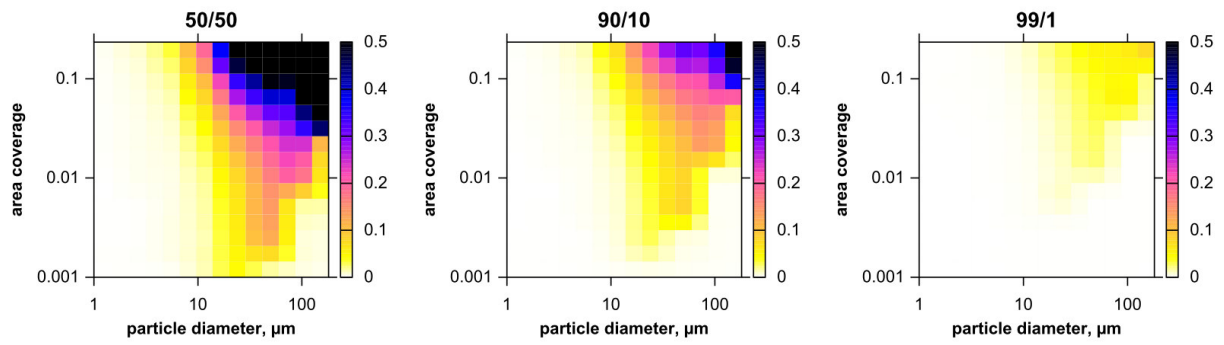


Fig. S 6: Maps of particle deposition density on the DPDS substrates for  $4 \mu\text{m} < d_g < 8 \mu\text{m}$ . Each division on the x and y axes equals 2 mm distance.

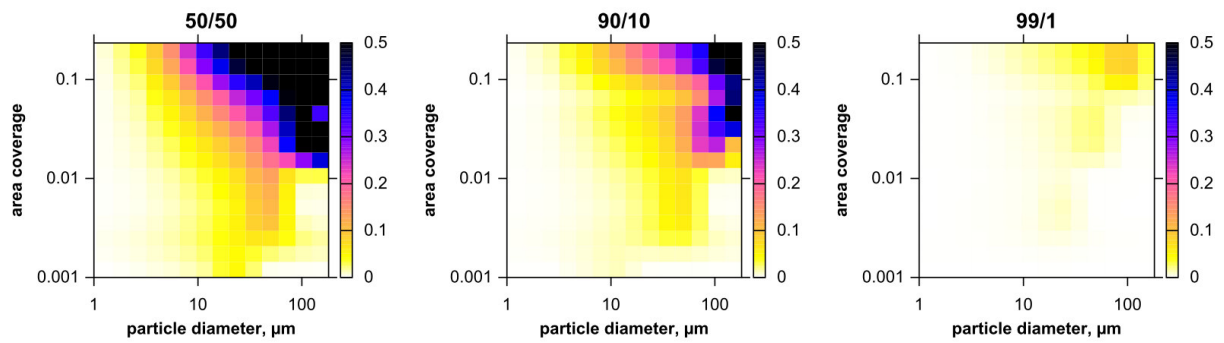
---

*Detectable mixture: CV-ground*



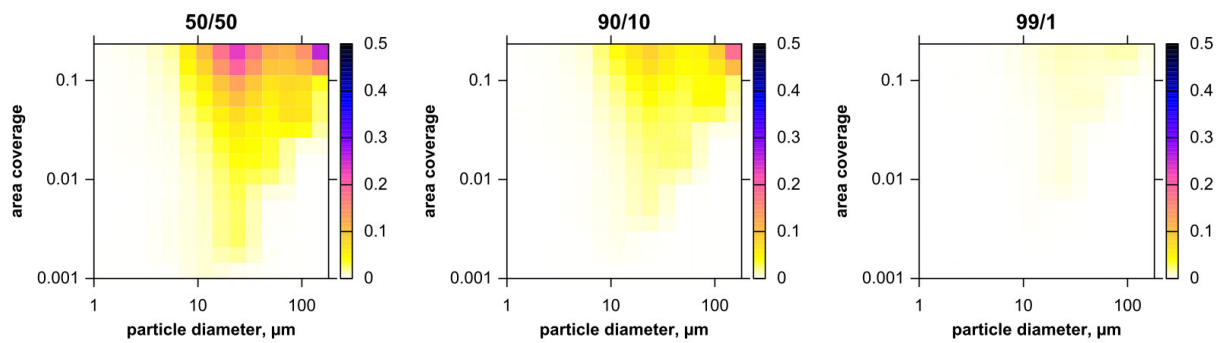
---

*Detectable mixture: CV-air*



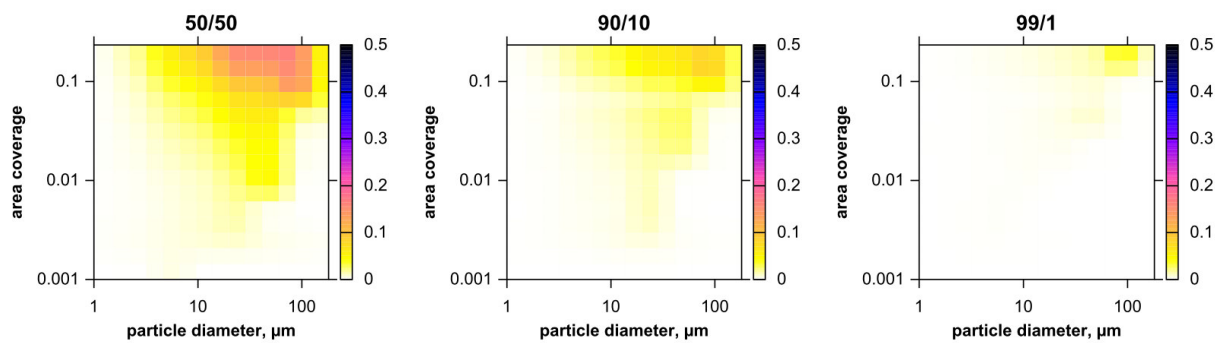
---

*Strong mixture: CV-ground*



---

*Strong mixture: CV-air*



---

**Fig. S 7: Upper 95% quantile of the fractions of internally mixed particles due to coincidental mixture on the substrate (color scale) as function of the projected area diameter and substrate area coverage, for a two-component system. Strong mixture refers to a minimum particle volume fraction of the other component of 20 %, detectable mixture refers to 1 %. Ratios of the two components in the base aerosol are given as percentages above each plot.**

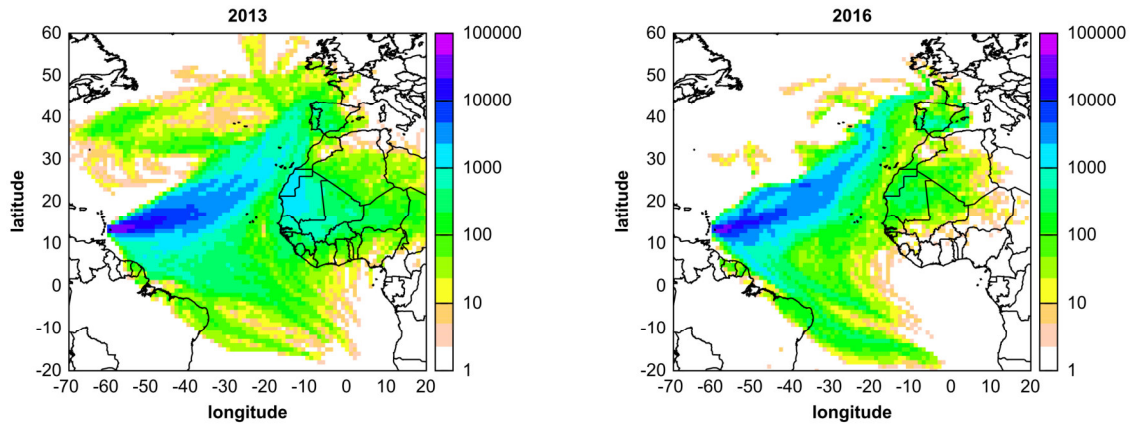


**Fig. S 8:** Potential air mass provenance during the measurement campaigns 2013 and 2016. A location is counted as potential provenance, if the trajectory at this point is lower than modeled boundary layer height. Colors indicate number of according trajectory point for each grid cell, corrected for differences in grid cell area.

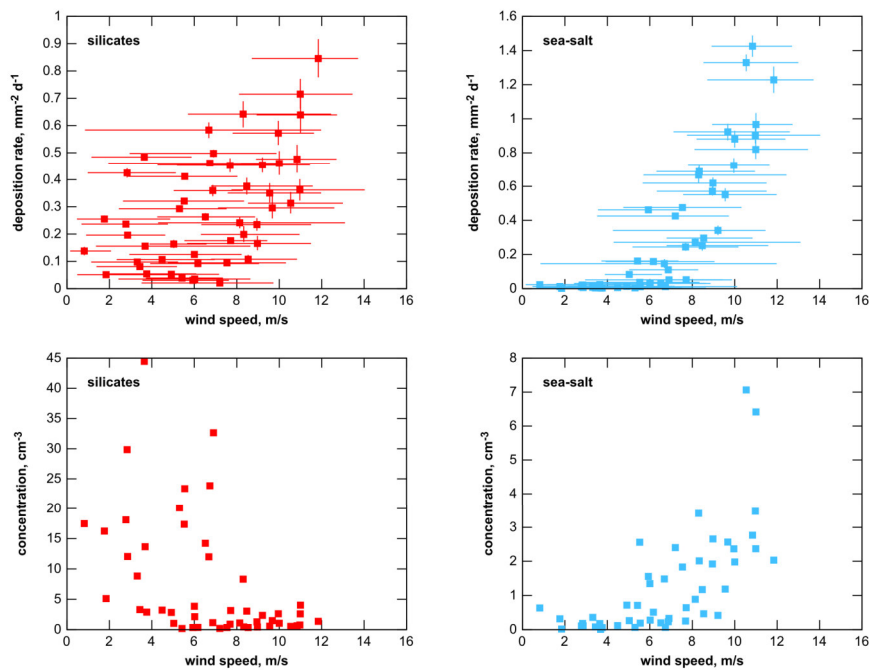


**Fig. S 9:** Total number deposition rate (upper graphs) and total number concentrations calculated with the Piskunov model (lower graphs) for all samples of 2013 and 2016 as function of wind speed for silicate and sea-salt particles. In the upper graphs, variation in wind speed is given as central 95 % quantile of 1-minute averages, and statistical uncertainty of the deposition rate is shown as two-sided 95 % confidence interval.

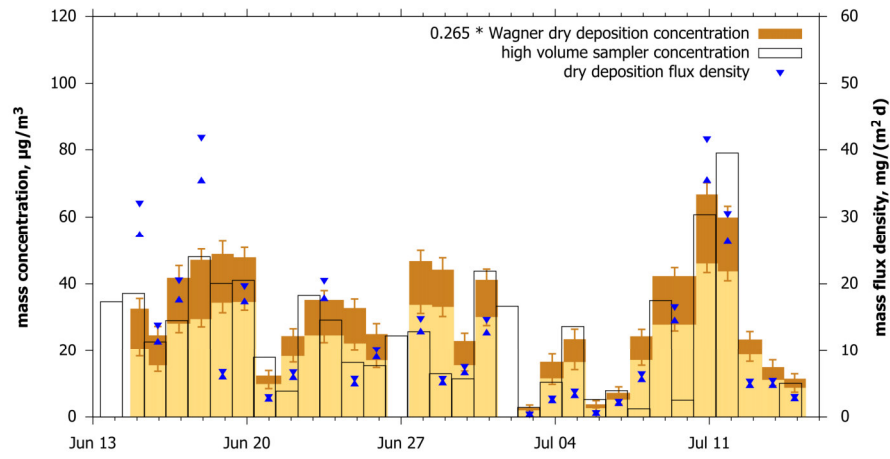


**Fig. S 10:** Dust mass concentration and flux density time series derived from DPDS data with a linearly tuned Wagner deposition velocity model, compared to such obtained from the a high-volume sampler (Kristensen et al. 2016). The darker brown bar shows the range from lower to upper estimate, the blue triangles the lower and upper estimate of dust deposition flux density.

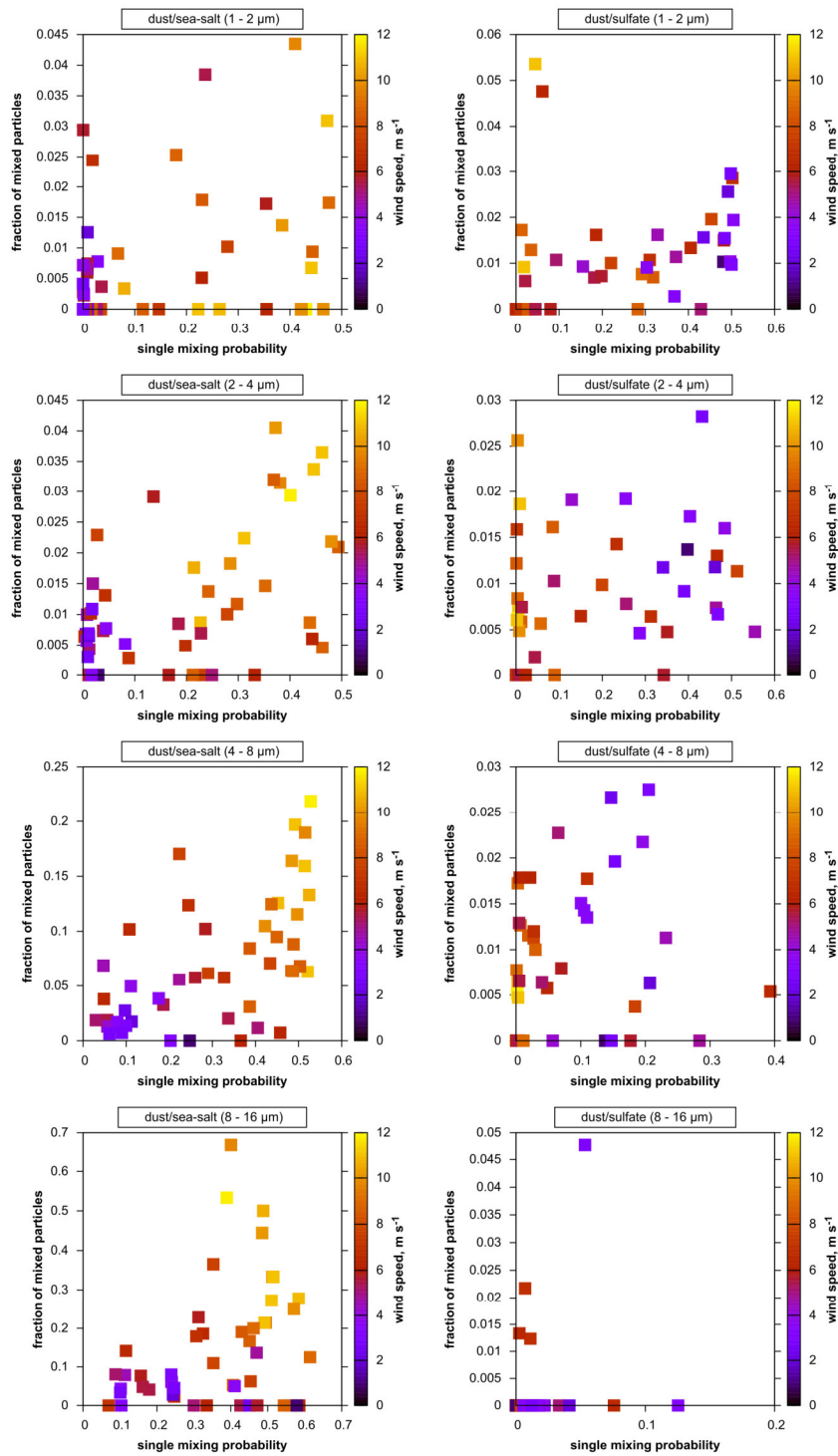


**Fig. S 11:** Ratio of binary mixed particle abundance to according pure compound abundance as function of the size-restricted single mixing probability. Deposition rate is color coded.